ELECTRONIC ANTIBODY MICROARRAYS FOR LABEL-FREE CELL IMMUNOPHENOTYPING

A Dissertation
Presented to
The Academic Faculty

by

Ruxiu Liu

In Partial Fulfillment
of the Requirements for the Degree
Doctor of Philosophy in
Bioengineering

Georgia Institute of Technology
May 2020

ELECTRONIC ANTIBODY MICROARRAYS FOR LABEL-FREE CELL IMMUNOPHENOTYPING

Approved by:

Dr. A. Fatih Sarioglu, Advisor
School of Electrical and Computer Engineering
Georgia Institute of Technology

Dr. Omer Inan
School of Electrical and Computer Engineering
Georgia Institute of Technology

Dr. Albert B. Frazier
School of Electrical and Computer Engineering
Georgia Institute of Technology

Dr. Wilbur Lam
Wallace H. Coulter Department of Biomedical Engineering
Georgia Institute of Technology

Dr. Andrés García
George W. Woodruff School of Mechanical Engineering
Georgia Institute of Technology

Date Approved: March 23, 2020

Betting on you

I am betting on you

Infinite

To me

To my beloved family

To the people I meet

ACKNOWLEDGEMENTS

Time flies when we are having fun; and flies even faster as we get older. To slow the time down, I sought to do something that is not fun, ultimately coming to Georgia Tech and starting my Ph.D. battle in bioengineering. Not surprisingly, the enemies started to come like a random variable following the Poisson distribution with a very large parameter k. Just in the training stage, I used up all my artifices in System and Control but could not harm the enemies at all. I stayed at the origin and started to doubt my decision.

Luckily, I met Dr. Sarioglu. He took me with him as a team and encouraged me to start over. He customized the equipment specially for me and taught me how to take on the battlefield, training me in close mentorship. He taught me the skills to survive and counseled me on how to beat the strong opponents together. More than the number of enemies I defeated, he cared more about my conditions and feelings, he was always there whenever I needed help and comfort, and my power and intelligence could always be recovered after his healing. I am so grateful and proud to be the first member of his team.

During the journey, I met several other youths who might be as ignorant and impulsive as the younger me. Each of us had different backgrounds which could cover my weaknesses. As a weak individual, I sought help from them and tried to group them into a strong team to protect myself. Thanks to the discussions with them, I was able to understand the enemies from multiple perspectives and chose the best solution to defeat the enemies. During the ceasefire period, they tried to have fun with each other using the limited resources to get them through the tough times. For the entirety of this long march,

we spent the most time together. I thank them for dissipating the loneliness around me and making my life much more colorful and beautiful.

Sometimes, when I felt frustrated and found no exit or relief, I would always hear a mystical whisper that said, “come to us”. When I would hear this, some energy would break through my wall of frustration and fill my spirit, and in front of me I would see some teleported cash and other items. I understand this to be my parents, who not only gave me my life and shaped my character but continue to devote everything to support my fight to soldier on. I am deeply sorry about them burning themselves to prolong my life, but I am still not powerful enough to reverse, or even just stop the conversion.

I have much to be thankful for, including the miraculous background music, *Bad* by Infinite, which significantly improved my luckiness attribute, enabling me to tame and control the enemy. I finally killed the final boss and cleared the stage, and now have a chance to play the New Game Plus. Before starting this new game, I looked back and recounted the details of every battle; suddenly, I was amazed by myself. As a sensible and emotional person, it is very hard for me to catch the logic and structure of the enemies. I must thank myself for persevering and executing under the weight of a long and arduous struggle. Finally, everything has come to an end.

Be ready for the New Game Plus.

TABLE OF CONTENTS

LIST OF TABLES

LIST OF FIGURES

LIST OF SYMBOLS AND ABBREVIATIONS

AC	Alternating current
ACK	Ammonium-chloride-potassium
APC	Allophycocyanin
APD	Avalanche photodiode
APTES	(3-aminopropyl)triethoxysilane
ATCC	American Type Culture Collection
a	Electrode width
BPSK	Binary phase shift keying
BSA	Bovine serum albumin
b	Length of Gold sequence (minimum)
CCD	Charge-coupled device
CD	Compact Disc
CD	Cluster of differentiation
CDMA	Code division multiple access
CMOS	Complementary metal-oxide-semiconductor
CTC	Circulating tumor cell
C_{dl}	Double layer capacitance
C_m	Medium capacitance
C_{mem}	Cell membrane capacitance
$C_{mem,0}$	Cell membrane capacitance per unit area
c	Particle/cell concentration
c_{ab}	The particle/cell count at sensor a,b

c_k	Random bipolar pulse
DC	Direct current
DEP	Dielectrophoresis
DI	Deionized
DMEM	Dulbecco's modified Eagle's medium
d	Distance between electrodes
E	Average total bit error rate
EDL	Electrical double layer
EDTA	Ethylenediaminetetraacetic acid
ε_0	Vacuum permittivity
ε_i	Cytoplasm permittivity
ε_m	Medium permittivity
ε_∞	High-frequency suspension permittivity
FBS	Fetal bovine serum
FEA	Finite element analysis
FITC	Fluorescein isothiocyanate
FSC	Forward scatter
f_c	Signal frequency
GMR	Giant magnetoresistance
G_f	Geometry constant
g	Gap length between finger electrodes
h	Microfluidic channel height
I	Correlation output
I_0	Correlation output (matched part)

I_k	Correlation output (interference part)
IGA	Improved Gaussian approximation
IRB	Institutional review board
k	Elliptic modulus
k	Number of coincident cells
k'	Complementary modulus
k_{out}	Elliptic modulus of the outermost unit block
L	Length of common electrode (minimum)
LED	Light emitting diode
LFSR	Linear-feedback shift register
l	Length of electrode
λ	Expected number of coincident cells
MACS	Magnetic-activated cell sorting
m	Number of sensors in the sensor network
μ_p	Mean of the sensor signal power level
μ_Ψ	Mean of the variance of the interference
N	Number of bits in the digit code
n	Gold sequence calculation factor
PA	Photoacoustic
PAFC	Photoacoustic flow cytometry
PBS	Phosphate buffered saline
PDMS	Polydimethylsiloxane
PE	Phycoerythrin
PMT	Photomultiplier tube

PRN	Pseudorandom noise
P_e	Error rate
P_{e0}	Error probability
P_k	Signal power from the k-th sensor
p_{ab}	The fraction of particles/cells in chamber a,b
Φ	Cell volume fraction
RPS	Resistive pulse sensing
R_{ce}	Surface electrode resistance
R_i	Cytoplasm resistance
R_m	Medium resistance
RPMI	Roswell Park Memorial Institute
SAW	Surface acoustic wave
SCM	Schwarz-Christoffel mapping
SNR	Signal-to-noise ratio
SPION	Superparamagnetic iron oxide nanoparticle
SSC	Side scatter
STEAM	Serial time-encoded amplified microscopy
s_k	Individual sensor signal
σ_i	Cytoplasm conductivity
σ_m	Medium conductivity
σ_p	The standard variance of the sensor signal power level
σ_Ψ	The standard variance of the variance of the interference
T	Period
T_b	Period of a sequence

T_c	Period of a bit
τ_k	Delay of k-th sensor
V	The volume of the sensing region
w	Width of electrode
X	Number of coincident cells (random variable)
Ψ	The variance of the interference (Gaussian random variable)
ZCR	Zero-crossing rate

SUMMARY

Immunophenotyping (i.e., identifying cell membrane antigens) is widely used to characterize cell populations in basic research and to diagnose diseases from surface biomarkers in the clinic. This process usually requires complex instruments such as flow cytometers or fluorescence microscopes, which are typically housed in centralized laboratories. Microfluidic devices can be used as immunophenotyping assays through immunoaffinity-based capture of the target cells, and are able to analyze a limited-volume sample in a small-footprint, with the ultimate goal of replacing the need for centralized laboratories. However, microfluidic devices are typically designed for qualitative analysis, and almost always require external tools for the readout, which negates the cost and portability benefits of the chip itself.

In the thesis, we introduce a microfluidic technology that employs a network of integrated electrical sensors to identify cell subpopulations based on their membrane antigens in a quantitative manner. To realize this technology, we develop a scalable electronic sensor network called microfluidic CODES (microfluidic coded orthogonal detection by electrical sensing), which combines code division multiple access (CDMA), a spread spectrum telecommunications technique, with Coulter sensing for the distributed detection of cells at strategic nodes across the microfluidic device from a single electrical output. By integrating the Microfluidic CODES technique with microfluidic cell capture chambers pre-functionalized with antibodies against target antigens, the device will achieve all-electronic cell immunophenotyping through the combinatorial arrangement of antibody sequences along microfluidic paths. Our technology will not only provide an

integrated platform for label-free combinatorial immunophenotyping of cell populations against multiple antigen targets, but also be built on affordable hardware well suited for resource limited settings or point-of-care applications.

CHAPTER 1. INTRODUCTION

1.1 Background and motivations

Cell surface markers are essential proteins or carbohydrates [1,2] involved in a variety of cell functions, ranging from cell-cell interactions, ligand-receptor binding, and cell signaling, to serving as transporters, ion channels, enzymes, and adhesion molecules [3]. Because different cell types usually express varying subsets of surface markers, cell surface markers, especially cluster of differentiation (CD) antigens [4], serve as chemical fingerprints to identify and classify cells (e.g., CD8 is a marker for cytotoxic T cell, a type of killer cell in the human immune system) [5]. Moreover, the expression of cell surface markers is dynamically altered at different stages during the differentiation of cell lineages, both for healthy cells and malignant tumor cells. For example, CD43 is expressed on the later stages of B cells but not on the earlier stages [6]; the carcinoembryonic antigen (CEA) is highly correlated to the development of colorectal cancer [7].

The profiling of the cell surface markers, i.e., immunophenotyping, is, therefore, an important process with a wide range of applications in basic research and clinical studies to provide comprehensive information about the cell state, and is routinely used to characterize cells in lineages of differentiation and to diagnose and classify diseases derived from those cells.

1.1.1 Flow cytometry

Flow cytometry is a widely used method to quantitate the properties of single cells. First introduced in 1950, flow cytometry is able to measure the number, size, granularity,

surface markers, expression of proteins in a heterogeneous cell population, and is currently the gold standard for immunophenotyping assays [8]. In the process, a suspension of cells or particles is injected into the flow cytometer instrument; cells are passing through a laser beam at the detection zone of the flow cytometer in a monodisperse and sequential manner at a rate of thousands of cells per second. The lights transmitted through the cells are then quantitated by an array of photodetectors, which can quickly be processed by the computer in time, representing the information of the cell populations. Since flow cytometry has the strong power in analyzing heterogeneous cells in a short time, it is used in basic research and clinical applications for various applications, including molecular biology, pathology, immunology, virology, plant biology, and marine biology [9-18].

A flow cytometer usually consists of 3 main systems (Figure 1.1): the fluidics system, the optics system, and the electronics system. The fluidics system carries and aligns the cells in a liquid stream (sheath fluid) to the laser beam for interrogation; the optics system applies multiple lamps and lasers to illuminate the cells, collects and conducts the forwarded and scattered light signals into the appropriate detectors through channels equipped with optical lens and filters; and the electronics system converts the light signals into electrical signals using photodetectors, amplifies and samplings the signals, and transmits the signals into the computer for further processing.

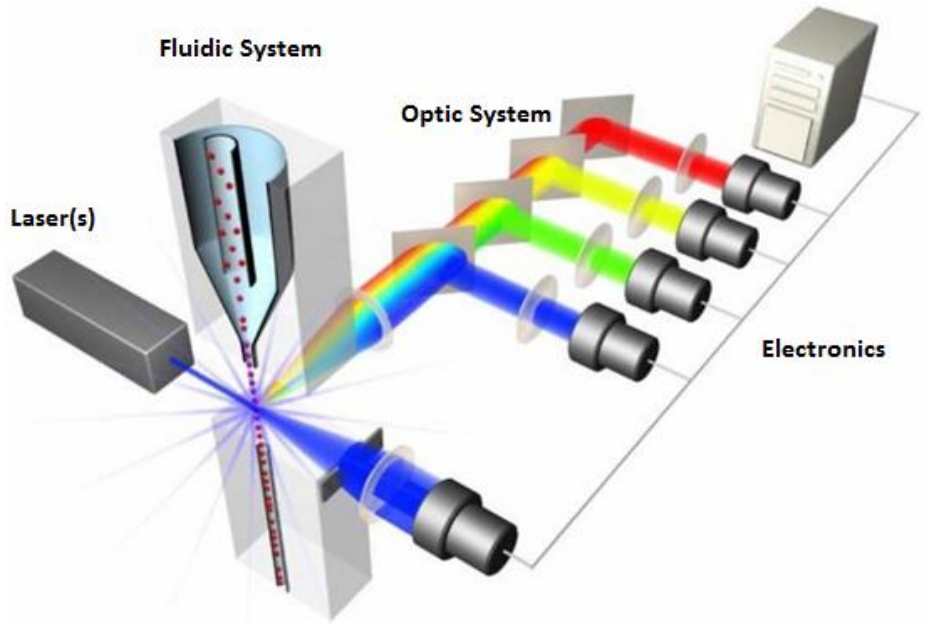

Figure 1.1 – The basic structure and principle of flow cytometry (From the University of California, Irvine, Flow cytometry Core Facility [19]).

In a flow cytometer immunophenotyping assay, cells are usually pre-labeled with fluorophore-conjugated antibodies specifically targeting the antigens of interest, and the fluorophores are excited by the lasers in the optics system when the fluorescently labeled cells pass through the detection zone where the resulting fluorescence emission is measured. From the fluorescence intensity, flow cytometers can quantify various surface marker expression levels on cells. With the development of fluorophore and optical detection resolution, a flow cytometer can be integrated with multiple lasers and fluorescence detectors, and with the increasing of the number of detectors, the modern flow cytometer can detect at most ~40 parameters of the cells simultaneously.

However, even though the modern flow cytometer can cover the wide fluorescence range among multiple fluorophores, because of the overlapping between the excitation and emission spectra of different fluorophores [13,20], flow cytometer is usually limited in the number of antigens it can simultaneously probe. Moreover, the three systems in a flow

cytometer, especially the optics system, have to be well aligned and coordinated precisely, making the manufacturing of the tool complicated, the dimension of the tool bulky, the price of the tool expensive, and the operation of the tool labor-intensive. These limitations fixed the flow cytometry into centralized laboratories and cannot be performed at the point of care settings.

1.1.2 Antibody microarray

Antibody microarray is a technology widely used for the detection of protein expression. In the microarray, a collection of antibodies are spotted and immobilized on a surface, such as plastic, glass, or silicon, in an array format to interact with the targeting antigens based on the antibody-antigen affinity. Antibody microarrays have been used for the detection of surface markers from cell populations, such as CD antigens, pathogen antigens, and soluble antigens [21-30]. Such devices rely on highly specific immunoaffinity-based capture of cells expressing target antigens and are widely used in the research on signaling pathways, enzyme kinetics, drug mechanism, and clinical research, such as autoimmune diseases, cancers, neurodegenerative diseases, and infectious diseases.

The biggest attractiveness antibody microarrays have is their capabilities to be used in the study of a diverse number of surface markers or other proteins at one time, which increases the throughput of the detection procedure. Also, the antibody microarrays are able to use sample volume to reach very high sensitivity, making antibody microarrays proper tools for the detection of protein expression from various biofluids, including serum, plasma, and tissue lysates. However, it is very hard to obtain the combinatorial and

sequential immunophenotype information of heterogeneous cells, since each individual cell can only interact with one of the spots in the antibody array. And also, antibody microarrays do not have the direct readout for the quantification analysis.

1.1.3 Microfluidic devices

Microfluidic devices have long been sought for analyzing a limited-volume sample in a small-footprint, with minimal cost and with the ultimate goal of replacing the need for centralized laboratories, and hence are commonly referred to as "lab-on-a-chip" systems. According to its name, microfluidics is the study of the system that applies fluidic channels or chambers with dimensions at the microscale to process small quantities of fluids with a volume of micrometers. At the microscale, the behavior of fluids differs from the one in the macroscale, which brings interesting and important properties to the experiments using microfluidic devices, and the technology has been applied to various research areas to save time and money. Comparing with the conventional experimental setup, microfluidic devices have the following advantages:

- Use fewer samples and reagents, which can reduce the experimental cost and waste production and save energy.
- Move the experiment from a centralized lab to a diverse environment.
- Control the flow and experimental parameters precisely on the microscale.
- Take a short reaction time and get results fast and effectively.
- Increase the detection and reaction resolution to the scale of molecules.

Indeed, lab-on-a-chip technologies offer exciting opportunities for deterministic analysis of biological samples in a well-controlled microenvironment and also offer unique

capabilities to manipulate biological particles such as human cells, bacteria, viruses, and proteins in microfluidic channels under a variety of force fields (e.g., mechanical, chemical, electrical, magnetic, etc.) [31-34]. These not only enable complex sample preparation steps to be performed on-chip but also allow biological constituents to be fractionated based on the contrast in biophysical (i.e., size [35,36], density [37], electrical permittivity [38,39], stiffness [40,41]) and/or biochemical [42,43] properties.

However, microfluidic devices often do not have integrated readouts for quantitative analysis, and highly rely on external instrumentation, for the readout for further analysis, microscopy has been the method of choice for acquiring particle position on the microscale. Despite its convenience, microscopy introduces redundancy into the system, producing large amounts of data at the expense of temporal resolution, and requires specialized high-speed cameras to capture fast hydrodynamic events in microfluidic devices. Such instrumentation needs typically tie the microfluidic chip to the lab infrastructure and limit its use in mobile settings. While cell phone-based computational-imaging approaches allow microscopy to be performed in mobile settings, these systems do face challenges such as rigid field-of-view, the requirement for optically transparent substrates, external components, and throughput that can easily be addressed by developing an integrated system. Different types of sensors have been integrated into microfluidic devices for the standalone lab-on-a-chip assays that can quantitatively analyze cells. Based on the type of the signal, the sensors can be divided into the following categories:

- Optical sensors. By minimizing the optical microscopy system into tiny optical fibers and optosensors, the microfluidic chips integrated with optical sensors can detect the light or fluorescent intensity and transfer the optical information into

the signals. The optical sensors include the simplest ones count the number of shadows or scattered beams generated by the particles blocking the normal laser path from a pore [44], and the optosensors count the number of the fluorescent pulses from the particles in a stream labeled with fluorophores [45] or excited via chemiluminescence [46]. The same principle has also be applied to Compact disc (CD) microfluidics to detect the number of particles in the channels by recognizing the number of abnormal signals using the normal CD reader [47].

- Mechanical sensors. Mechanical sensors detect the fluctuations in the measurement of the mechanical properties of the system to count the number of particles. The most widely used mechanical sensor measures the resonant frequency of a lever beam with an internal channel [41] or across a channel [48].
- Thermal sensors. Some particles can be heated when passing through a field, and the thermal particle detector can monitor the temperature at a pore and sense the heated particles. The heater and the sensor can also be combined to simplify the design of the device [49].
- Electrical sensors. By providing an AC/DC electric field in the sensing region in a microfluidic device, the electrical sensors can track the resistance, impedance, or capacitance change in the electric field [50-52]. The number of particles can be obtained by counting the number of pulses in the electrical signal. By adjusting the dimension of the electrodes and the microfluidic channels, the electrical sensing can be widely used for particles with various sizes. The electrical sensors can also be used in the droplet microfluidics for particle sensing [53].

- Magnetic sensors. Similar to the electrical sensors, the magnetic sensors can detect the magnetic field change due to particles [54]. However, due to the property of the materials, the magnetic sensors can only be applied to the magnetic beads or particles conjugated with magnetic beads.
- Chemical sensors. Chemical sensors detect the particles based on chemical reactions, but they are usually integrated with other types of sensors for the result display (electrical current, optical intensity) [55,56].

Among these, electrical sensors have been the most common due to ease of fabrication, label-free operation, high signal-to-noise ratio, and the ability to directly interface with external electronics [50,53].

1.1.4 Coulter counter and Coulter principle

Among various types of sensors, Coulter counters allow rapid detection of particles by electronically utilizing a technique called resistive pulse sensing (RPS), or Coulter principle [57,58]. In RPS, particles of interest are suspended in an electrolyte and passed through a pore between two electrodes. As each particle displaces the electrolyte in the pore, electrical conduction is reduced temporarily, allowing particles to be detected (Figure 1.2). Therefore, one can determine the count and the size distribution of particles by the number and amplitude of pulses, respectively. From the 1950s, Coulter counters are widely used in hematology research, cell counting and sizing, and various particle characterization.

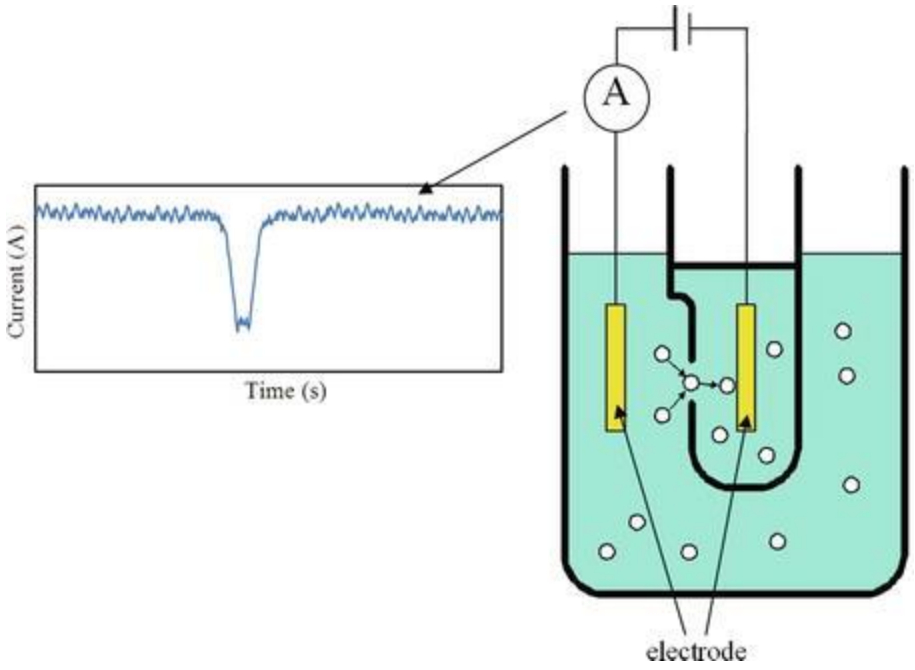

Figure 1.2 – The schematic of the Coulter counter and Coulter principle (From Springer, [46]). When the particle passes through the pore between two electrodes (right), a current drop will be generated in the electrical signal (left).

Coulter counters are attractive to microfluidic devices as they can easily be integrated into a microfluidic device providing simple and robust on-chip detection. The resistive pulse sensor geometry can be micromachined to produce predictable waveforms to achieve higher sensitivity and dynamic range in sizing particles [59-63]. Enabled by this simple and robust sensing mechanism, microfluidic Coulter counters are versatile instruments that have been used in the analysis of blood cells [64-66], proteins [67-69], DNA molecules [70], viruses [71], and nanoparticles [72].

Multiple Coulter sensors can also be integrated on the same device for detection at different locations across the chip or to increase the device throughput [73-76]. With the goal of increasing the device throughput, the electrical detection of particles at multiple locations across microfluidic chips has previously been demonstrated either by allocating a dedicated Coulter counter at each monitoring location on the microfluidic chip [77-79]

or through multiplexing by electrically driving each location at a distinct frequency [80]. These devices, however, are more complex as they require interfacing with a larger number of electrodes. In addition, the scalability of these devices is limited since the number of electrodes to interface increases linearly with the number of the sensors.

Here, we want to develop a fully portable antibody microarray that is able to analyze a cell suspension against multiple antibodies without the aids from the external instrumentation. Such a system will provide exciting opportunities for the diagnosis of various disease types at the point of care or resource-limited settings.

1.2 Thesis flow

In this thesis, the aim is to integrate the microarray with a simple and scalable electrical sensor network, and the electronic immunophenotyping device will provide the cell information *via* electrical data that could easily be processed, stored, and transmitted using the already existing infrastructure. To achieve the goal, in this thesis, we will address the aforementioned challenges step by step. The goal is divided into three subgoals.

Subgoal 1: To design and fabricate the sensor network that is integrated with a large number of electrical sensors into the device with simple device complexity for the Coulter detection of cells in microfluidic devices (Chapter 3).

Subgoal 2: To characterize the microfluidic devices integrated with the electrical sensor network via computational and experimental analysis. In the subgoal, we will establish an equivalent circuit model for the sensor network (Chapter 4), and then discuss the issues related to the scaling of the sensor network (Chapter 5). Besides, we will

introduce a new technique to facilitate the fabrication of the scaled sensor network in microfluidic devices (Chapter 6).

Subgoal 3: To integrate the antibody microarray with the developed sensor network to create an electronically readable antibody microarray for the immunophenotyping of cell populations (Chapter 7).

CHAPTER 2. MICROFLUIDIC FLOW CYTOMETRY, A BRIEF REVIEW

As introduced in Chapter 1, currently, the gold standard for immunophenotyping is flow cytometry. However, flow cytometers are bulky and expensive tools, which fixes the flow cytometry to centralized laboratories. Microfluidics provides opportunities for performing chemical/biological assays in a tiny and cheap manner. If we integrate them together, we may be able to finish the immunophenotyping on a lab-on-a-chip device. In fact, many research groups have been working on microfluidic flow cytometry research and had some exciting results. Before going deep into our discussion, in this chapter, we will do brief literature research about the previous microfluidic flow cytometry work.

Similar to a conventional flow cytometer, in a microfluidic flow cytometer, there are also the fluidics system, optics system, and electronics system. Based on the different operation and detection methods, the optics and electronics system may not coexist in one system; here, we divide a microfluidic flow cytometer into two parts, the fluidic system and the detection system, to summarize the recent research on microfluidic flow cytometry.

2.1 The fluidic system in microfluidic flow cytometry

The fluidic system is a very important part of the benchtop flow cytometry system; it provides a uniform environment and controls the flowing path and moving pattern of the cells. Similarly, in microfluidic flow cytometers, microfluidic channels also regulate the cells passing through the detecting region in a monodisperse and sequential manner. Some flow cytometers also have the particle sorting function, to distribute the particles into

different channels using the fluidic system. In the subsection, we will talk about the sample focusing and sorting strategies in the existing microfluidic flow cytometry.

2.1.1 Sample focusing in microfluidic flow cytometry

In a conventional flow cytometer, samples need to pass through the small detection pore in a monodisperse and sequential manner at a constant rate to ensure the detection accuracy, so the position of the particle in the channel is very important for the performance of the tool, and flow focusing is an easy way to regulate the position of the cells. Flow cytometers use surrounding sheath flows to compress the particles to the center. Similarly, most of the microfluidic flow cytometers use the hydrodynamic focusing by sheath flow to regulate the samples, because it is easy and simple in implementation. Other than that, there are also microfluidic flow cytometers applying inertial focusing, dielectrophoresis force, acoustic waves to regulate the samples, which has been summarized in Table 2.1.

- Hydrodynamic focus

Hydrodynamic focus is the most widely used method in microfluidic flow cytometers. In this method, the sample fluid and many sheath fluids are infused co-laminarly at the rate optimum to focus the sample into a narrow streamline. Many research groups have developed different 2D/3D structure for hydrodynamic focus [81-90]. Skommer et al. proposed a microfluidic system with a 2D hydrodynamic focusing structure [81]. The device could detect the apoptosis status corresponding to cell cycle periods based on six parameters. Huang et al. introduced a microfluidic flow cytometer to detect the motile human sperm [82]. The system applied a 2D hydrodynamic side-focusing module, and live and dead sperms would interact differently with the laminar flows.

Table 2.1 – A summary of the sample focusing methods in microfluidic flow cytometry

Method	Principle	Notes
Hydrodynamic-2D	Sheath flows, act on an angle	Simple design No control in one direction Need a large amount of sheath buffer
Hydrodynamic-3D	Sheath flows, surrounding the sample stream	Complex design Good focusing result Need a large amount of sheath buffer
Inertial	Forces generated by geometry changes	No effects on cells Affected by particle size Good focusing result Difficult to integrate Complex design
Dielectrophoresis	Force on particles from the electric field	Easy to integrate Require accurate control Affected by particles and electric fields
Acoustic	Use sound wave to manipulate sample	Low throughput Affected by particle size

2D focusing structures are applied widely in the microfluidic flow cytometry applications, because they are simple to fabricate and duplicate. However, 2D focusing structures can only regulate the sample streams in one plane (usually horizontal plane). Differently, 3D focusing structures can regulate the streams in both horizontal and vertical planes, the variance comes from one dimension can be eliminated, and the sample is confined in the central line, so more accurate control of the sample can be achieved. 3D focusing is achieved using multi-layer designs, which usually require specialized microfabrication processes. The previous studies on 3D focusing try to increase the sheath flow branches, and the current studies care more on creating sheath flows in different geometry designs or integrated methods. Yang et al. introduced a 3D focusing microfluidic device equipped with a series of weirs with reducing height [86]. The device was able to

progressively focus the sample along the centerline by the Saffman shear lift force, and could reach more than 99.5% focusing efficiency tested using beads. Frankowski et al. proposed a microfluidic device to analyze blood components [87]. The device applied a two-stage cascade focusing unit and a vortex spin focusing unit to focus the samples, and was used to detect $CD3^{pos}$ and $CD4^{pos}$ cells in the blood.

- Inertial focusing

Inertial focusing is a passive focusing method, and utilizes the inertia of the fluid to focus samples in the channel. Since it does not require external forces, it has been applied widely in microfluidic flow cytometry [91-93]. However, inertial focusing requires Reynolds numbers high enough to affect the particles, so the device usually operates under higher flow rates [94]. In an inertial focusing process, three forces act on the particle simultaneously, namely a microchannel wall interaction force, a shear gradient lift force, and drag forces from the secondary flows [91]. Chung et al. introduced a device [93] to focus the particles. The device applied 30 steps with different height in a 6 cm straight channel, and could reach 99.77% capture efficiency.

- Dielectrophoresis focusing

Dielectrophoresis (DEP) is widely used in microfluidics for particle manipulation. DEP focusing is based on the moving process of dielectric particles in the non-uniform electric field, DEP force moves the particles to the equilibrium position. The DEP force is determined by several factors, including the size of the particle, the dielectric properties of the particle and the medium, and the frequency of the current if in an alternating current field [95]. DEP is also used in microfluidic flow cytometry to focus the sample stream

[96,97]. For example, Shaker et al. introduced a microfluidic flow cytometer to detect cell morphology [96]. In this device, the DEP force generated by liquid electrodes was used to focus the particles to the center. However, the DEP force is relatively weak, and decays rapidly on particles. Usually, it cannot be used on devices that need high flow speeds.

- Acoustic focusing

Acoustic waves can generate large forces on particles in microfluidic devices. Under the force of acoustic waves, particles move forward to the pressure nodes or antinodes. The biggest advantage of acoustic wave focusing has is that it is a nondestructive method for samples, and there is no specific requirement for the electrical properties of particles and the medium. Because of the advantages, surface acoustic wave (SAW) has been applied in microfluidic flow cytometry devices for sample focusing [98,99]. Grenvall et al. presented a microfluidic flow cytometry which can position samples precisely using SAW [98], the device used Coulter counter type sensor to analyze diluted blood sample, and the results had good agreement with benchtop flow cytometry.

2.1.2 Sample sorting in microfluidic flow cytometry

In the flow cytometry, sorting is an optional function to select the subpopulation from the sample. The subpopulations need to be extracted without damage for further use. In a conventional flow cytometer, it is achieved by deflecting charged particles in an electric field. For microfluidic flow cytometers, many sorting systems have been developed, as summarized in Table 2.2. Since sorting systems for flow cytometry have no big difference from sorting systems for typical microfluidic devices, which has been studied a lot in the

previous reviews [34,100], here, we just simply list the sorting methods used in the existing microfluidic flow cytometry for comparison.

Table 2.2 – A summary of the sample sorting methods in microfluidic flow cytometry

Method	Principle	Notes
Optic	Optical tweezer	No effect on cells Precise control Expensive
Electric	Dielectrophoresis force	Easy to integrate Simple to fabricate Precise control
Magnetophoretic	Control of magnetizable sample	Easy to integrate Magnetic marker required
Acoustophoretic	Manipulated by the acoustic wave	No effect on cells
Piezoelectric actuator	Piezoelectric actuator	No effect on cells Easy to integrate Piezoelectric transducer needed External tools needed
Passive	Inertial force, hydrodynamic force, filtration, deterministic lateral displacement, etc.	No effect on cells External tools needed Complex design

2.2 The Detection system in microfluidic flow cytometry

The detection of the specific target is the key task in the flow cytometry. In conventional flow cytometry, the samples are detected by the optics system and the electronics system. In microfluidic flow cytometry, there are several methods to detect the cells depending on the assays and the analysis needed. Traditionally, the samples are detected and analyzed using optical methods. There are also non-optical methods including

electrical methods, acoustic methods, and magnetic methods. A summary of each method is listed in Table 2.3.

Table 2.3 – A summary of the detecting methods in microfluidic flow cytometry

Method	Principle	Notes
Optic-fluorescence	Excite light hits fluorophores on particle	Capable with multiple colors Fluorescent-labeling required Bulky and expensive Precise control
Optic-image	Camera capture image, analyze by the algorithm	Low throughput External tools needed
Electric	Impedance perturbed when particle flows	High throughput Easy to integrate Label-free detection
Magnetic	Magnetic field perturbed when particle flows	Easy to integrate Bulky Labeling required
Acoustic	Echo differs between different particles	Label-free detection External tools needed Strict calibration

- Optic-based methods

The most common method used in microfluidic flow cytometry is fluorescence-based methods, since they have high sensitivities. In such devices, leukocytes usually pass through a focused laser beam, scattered light and fluorescent emission are detected using optical sensors and used for cell classification. In essence, forward scatter (FSC) is used to evaluate particle sizes, side scatter (SSC) is used for internal granularities, and fluorescence information is used to discriminate the cells based on immunophenotypes, like a benchtop flow cytometer [101-104]. Recently, researchers have proposed many different approaches for miniaturizing the system, such as the optimization of the optical components [101] or

the detection process [102]. In the up-to-date devices, the light emitting diodes (LED) are always used as emission sources instead of lasers, and photomultiplier tubes (PMT), avalanche photodiodes (APD), or charge-coupled devices (CCD) are usually used as the emission detectors in the device [94]. For example, Xun et al. introduced a microfluidic flow cytometer using SSC and fluorescein isothiocyanate (FITC) fluorescence for the detection of leukocytes [103]. In the device, the leukocytes were detected using fluorescent PMTs, and the coincidence error of the system was less than 0.069%. Goda et al. proposed a flow cytometry-based on serial time-encoded amplified microscopy (STEAM), which can detect particles [104]. Not like the typical flow cytometry using LED or lasers as the light source, the device used femtosecond pulse fiber laser to generate light with wide spectral bandwidth. By using the novel detection method, the system could detect particles rapidly using a limited volume of samples, and throughput could reach as high as ~100,000 particles per second.

Other than the fluorescence-based method, the image-based method is another detecting method category applying the optical principle. The system usually consists of a microscopic platform including light sources, either brightfield/darkfield or fluorescence, lenses to magnify the detection field, and the detectors to capture the parameters of the particle, and image processing software to analyze the captured information [85,105]. Image-based devices are most fit for living cell analysis; however, the integrating of imaging parts highly decreases the throughput of the system. The detectors used in the system are typically CCD or complementary metal-oxide-semiconductor (CMOS) cameras. In the systems, cell images are captured and analyzed using the algorithm. Vercruysse et al. developed an image-based system for counting and classifying leukocytes [85]. The

device used the image to get two parameters to quantify the size and the granularity of the cells for the classification. Sawetzki et al. proposed a microfluidic flow cytometer using a high-speed CMOS camera to analyze the dynamic viscoelastic behavior of erythrocytes, and the device is able to distinguish the erythrocytes infected by *Plasmodium falciparum* within the response time [105].

- Electric-based methods

Optical components are usually expensive and need fine adjustment; to overcome the disadvantages, some research groups have tried to remove the optical system and used the electrical system only for the microfluidic flow cytometry assays [106-110]. These devices usually apply the aforementioned Coulter principle, which detects cells *via* impedance changes. For example, Mansor et al. presented [106] a microfluidic flow cytometer for yeast cell detection. The device used a dual tungsten microneedle in the middle of the channel to detect the impedance of the cell. Hasni et al. [107] proposed a microfluidic device combined hydrodynamic trapping and impedance spectroscopy measurements for cell detection. Using four metal electrodes and coated conductive polymer, the device was able to distinguish intact oocytes from the broken ones. Sometimes, capacity detection is also used as a part of the impedance detection. Song et al. introduced a 3D microfluidic capacitor sensor [110]. The sensor could detect the capacitance at two different stages of the algal *Dunaliella Salina*, and tell the viability of the algal from the differences.

- Magnetic-based methods

Magnetism has been involved in the conventional flow cytometry in the magnetic-activated cell sorting (MACS) process, but it is used much less frequently than optical- or electrical-based methods as detection methods since the magnetism detecting system is usually big. Helou et al. reported a magnetic-based microfluidic flow cytometry [111]. Similar to the fluorescence-based methods, the device also needs a pre-labeling step, using some superparamagnetic iron oxide nanoparticles (SPIONs) conjugated antibodies to label the cells. The labeled cells passed through the magnetic field created using an upstream NdFeB magnet, and the perturbance of the magnetic field was detected using a giant magnetoresistance (GMR) sensor, so the information of the cell was obtained. The throughput of the device was quite low (10 cells s^{-1}), but since GMR components were cheap and easy to integrate with the other parts, the same principle had been applied to some other microfluidic devices.

Other than GMR sensors, some groups applied magnetophoresis into microfluidic flow cytometry to distinguish cells [112]. In the devices, the cells are prelabeled by SPION-conjugated antibodies, and passed through a magnetic field. In the field, the cells with more surface antigen expression will deviate more than the cells with less expression from the streamline so that the cells can be discriminated. These devices can be integrated with cameras or other counting methods, and can reach a very high resolution and wide dynamic range.

- Acoustic-based methods

Ultrasound and photoacoustic (PA) waves have also been used to differentiate the cells as acoustic-based methods [113-115]. For the ultrasound sensors, the reflected

ultrasound from the particles contains the size information of the particles. For example, Komatsu et al. introduced a technique called “sonocytometry” [113]. In the technique, a high frequency ultrasound (30 MHz) was given to the particle samples, and the particles can be characterized using the ultrasound echo. Different from the ultrasound method which can only be applied *in vitro*, photoacoustic flow cytometry (PAFC) can be used *in vivo*, which is based on the PA effect [114] and has been successfully applied into circulating tumor cells (CTC) detection [115].

2.3 Summary

With the development of micro- and nano-technology, great progress has been made in the microfluidic flow cytometry related research. Researchers have proposed many flow cytometers for different applications. Even though each microfluidic flow cytometer selects individual principle and approach for the target, the devices share the same central dogma: the purpose of creating microfluidic flow cytometry platforms is to move the bulky flow cytometers from centralized labs, and perform the necessary assays in the point-of-care diagnostic devices. Based on the idea, it is important to have the final device inexpensive, portable, and user-friendly. From the summaries in this chapter, we can see that all the applications have their advantages and limitations, and it is hard to decide which method is the ideal approach as the panacea.

Targeting our goal for cell immunophenotyping assays, in this thesis, we are trying to be inspired by the previous research and balance each aspect, to provide a different perspective to solve the problem.

CHAPTER 3. MICROFLUIDIC CODES, THE MULTIPLEXED SENSOR NETWORK TECHNIQUE [116]

Continued with the problem in Chapter 1 when we want to integrate a large number of sensors in the microfluidic device. Since each sensor is using its own channel to detect and transfer the electrical signal, the total number of the electrodes is proportional to the number of the sensors, so that the integrated electrical sensor connection on the microfluidic chip will become very complex.

Inspired from the cellphones from our everyday life, code division multiple access (CDMA) telecommunications provide a solution to the problem. CDMA is a telecommunications technique that entails the use of both spread spectrum technology [117-119] and a digital coding scheme to carry out the multiplexed transmission of information across multiple transmitters sharing the same transmission channel to a base station. Each source in a CDMA network transmits information simultaneously within the same frequency spectrum. To differentiate between sources, each source is assigned a unique digital code, a so-called "digital spreading code." The codes are orthogonal with each other so that the signals can be identified in the presence of interference from other sources. CDMA labels each bit of information from a source by multiplying it by the digital spreading code exclusively assigned to that source. The bits that do not carry the correct label can then be rejected by a receiver matching a specific digital spreading code [120]. Similarly, if we apply the same orthogonal codes to different Coulter counters in the sensor network, then orthogonal detection at multiple points across a microfluidic device can be achieved in a simple and scalable way and signals from different sensors can be

multiplexed without increasing the number of external connections to the microfluidic chip. For this purpose, our solution is to construct sensors in microfluidic channels such that they each generate distinct signals.

In this chapter, we first introduce the scalable electronic sensor that utilizes CDMA for orthogonal detection of particles across a microfluidic device from a single electrical output. We call this technology microfluidic Coded Orthogonal Detection by Electrical Sensing or microfluidic CODES in short. We use microfabrication techniques to create coplanar electrodes such that particles passing over these electrodes produce bipolar digital codes, similar to the digital codes used in CDMA communication networks to differentiate between cell phone users. These codes are designed to be orthogonal to each other so that they can easily be distinguished through computation even when they overlap. Microfluidic CODES is simple and also scalable; it uses only 3 electrodes and can, in theory, be adapted to orthogonally detect particles at an arbitrary number of positions across a microfluidic device (Figure 3.1).

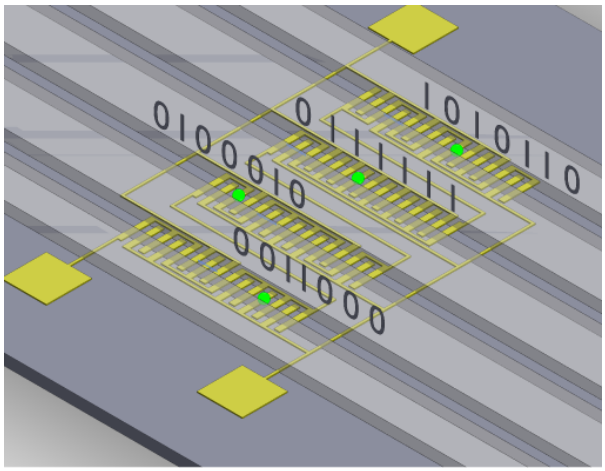

Figure 3.1 – The design of digitally coded microfluidic channels. Orthogonal digital codes are electrically generated as particles flow over coding surface electrodes.

3.1 Constructing the quasi-orthogonal code-set

At the heart of telecommunications is multiplexing, which reversibly combines information from multiple sources into a single data stream for the efficient use of a limited channel capacity. Generating truly distinguishable signals to orthogonally detect particles in multiple microfluidic channels without increasing the device complexity requires special consideration in coding, sensor design, and device layout. Thus, designing a set of unique, distinguishable digital spreading codes, which ensures information recovery in the presence of interference from multiple sources, is critical to the success of multiplexing in any CDMA-based approach.

From a mathematical perspective, the suppression of interference from multiple sources requires an orthogonal digital spreading code set, in which digital codes are pairwise orthogonal; that is, their cross-correlation or inner product is zero when they are in phase. Therefore, we can easily identify any digital spreading code by correlating the signal with all possible digital spreading codes in the code set. Perfectly orthogonal spreading codes, however, can be employed only in synchronous CDMA systems (e.g., a CDMA downlink from a base station to a cell phone) because of strictly controlled signal timing, which maintains code orthogonality. Our microfluidic device is an asynchronous system; that is, it entails an unsynchronized flow of particles over electrodes, which leads to the interference of sensor signals with an arbitrary time lag. Asynchronous CDMA systems (e.g., a CDMA uplink from cell phones to a base station) use quasi-orthogonal codes specifically designed to maintain a certain level of orthogonality (i.e., have bounded cross-correlation) under arbitrary time delays [120]. Therefore, our design consists of a class of quasi-orthogonal codes called Gold sequences [121,122]. Commonly used to

minimize multi-user interference in CDMA communication networks, Gold sequences provide a relatively large quasi-orthogonal code set for any given code length. In this section, we generate a set of seven-bit Gold sequences to multiplex four Coulter sensors on a microfluidic device.

As an initial step to generate Gold sequences, we designed maximal-length sequences (*m*-sequences) [119]. *m*-sequences are quasi-orthogonal spreading codes that have minimal out-of-phase autocorrelation, but are not necessarily bounded in their cross-correlation with other *m*-sequences. Therefore, they are well suited to resolve the self-interference of a spreading code with its time-delayed version. To generate two 7-bit m-sequences, we used two linear feedback shift-registers (LFSR) LFSR1 and LFSR2, each constructed with 3 shift registers, based on primitive polynomials $h_1(x) = x^3 + x^2 + 1$ and $h_2(x) = x^3 + x + 1$, respectively. For both LFSRs, we started with an initial state and the output is updated until it returns to the starting state (Figure 3.2). Using LFSR1, initialized at 001 state, and LFSR2, initialized at 111 state, we generated two *m*-sequences $m_1 = 1001011$ and $m_2 = 1110100$.

m_1 and m_2 constitute a so-called "preferred pair" of *m*-sequences as they satisfy the following criteria [117]:

1) $n = \text{odd or } 2 \pmod 4$, where m_1 and m_2 are each composed of $2^n - 1$ bits (n is the order of the polynomials, and in this case $n = 3$).

2) $m_2 = m_1[q]$, where q is odd, and either $q = 2^k + 1$ or $q = 2^{2k} - 2^k + 1$. $m[q]$ is the q-th decimation of m, obtained by sampling every q-th bit of m, after the first ($m_2 = m_1[3]$ and $k = 1$).

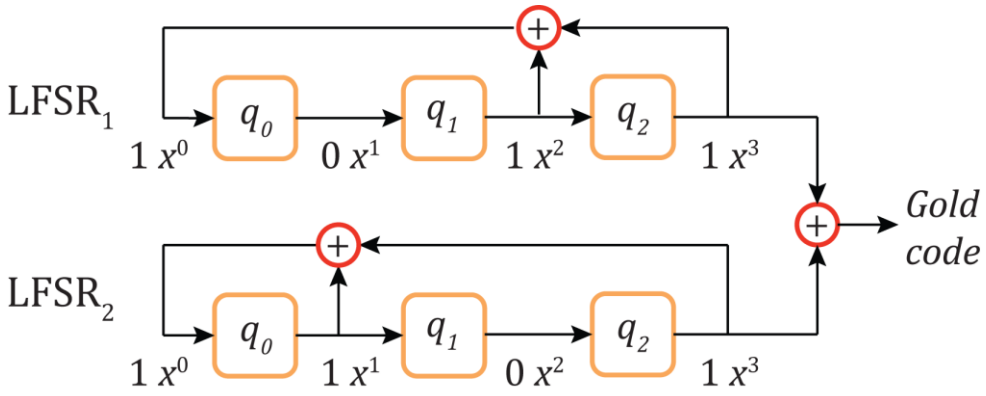

Figure 3.2 – Schematic diagram of the two linear feedback shift registers corresponding to polynomials $x^3 + x^2 + 1$ and $x^3 + x + 1$, which are used to generate 7-bit Gold sequences used in our device

3) $\gcd(n, k) = \begin{cases} 1, & \text{for } n \text{ odd} \\ 2, & \text{for } n = 2 \pmod 4 \end{cases}$ ($\gcd(3,1) = 1$).

Being a preferred pair, the cross-correlation between m_1 and m_2 is bounded. Using m_1 and m_2, we generated a set of $(2^n + 1)$ (i.e., in this case, 9) Gold sequences, whose cross-correlations are likewise bounded in the following way:

$$g(m_1, m_2) = \{m_1, m_2, m_1 \oplus m_2, m_1 \oplus D\, m_2, m_1 \oplus D^2\, m_2, \dots, m_1 \oplus D^{N-1}\, m_2\} \tag{3.1}$$

where the $D^i\, m_2$ is the i-th-bit cyclic shift of m_2 (Figure 3.3).

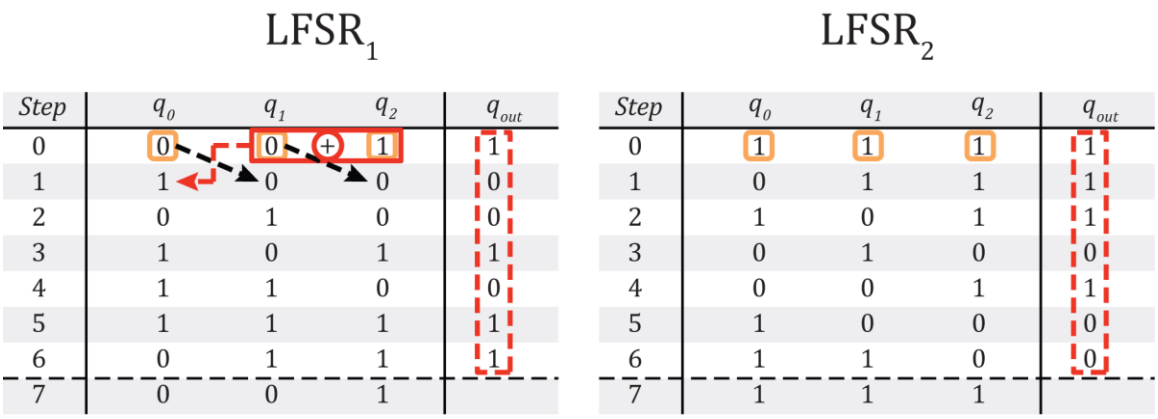

Step	q_0	q_1	q_2	q_{out}
0	0	0	1	1
1	1	0	0	0
2	0	1	0	0
3	1	0	1	1
4	1	1	0	0
5	1	1	1	1
6	0	1	1	1
7	0	0	1	

Step	q_0	q_1	q_2	q_{out}
0	1	1	1	1
1	0	1	1	1
2	1	0	1	1
3	0	1	0	0
4	0	0	1	1
5	1	0	0	0
6	1	1	0	0
7	1	1	1	

Figure 3.3 – States of the linear feedback shift registers to produce a preferred pair of m-sequences

Specifically, individual Gold sequences in our set are:

$$g_1 = m_1 = \quad 1001011$$

$$g_2 = m_2 = \quad 1110100$$

$$g_3 \coloneqq m \oplus m' = \quad 0111111$$

$$g_4 \coloneqq m \oplus D\,m' = \quad 0100010$$

$$g_5 \coloneqq m \oplus D^2\,m' = \quad 0011000$$

$$g_6 \coloneqq m \oplus D^3\,m' = \quad 1101100$$

$$g_7 \coloneqq m \oplus D^4\,m' = \quad 0000101$$

$$g_8 \coloneqq m \oplus D^5\,m' = \quad 1010110$$

$$g_9 \coloneqq m \oplus D^6\,m' = \quad 1110010$$

Among these codes, we chose four Gold sequences (g_3, g_4, g_5, g_8) to multiplex detection in four microfluidic sensors. Due to differential measurements of impedance modulations in our device, we first mapped 1's to 1 and 0's to -1 to create bipolar code sequences (as in Binary phase shift keying (BPSK) modulation) [123]. We then calculated normalized continuous-time periodic autocorrelation and cross-correlation between four Gold codes as a function of time the delay between them (Figure 3.4). Our calculations show that 1) all four codes produce a global maximum autocorrelation peak at zerothe -time delay, 2) the cross-correlation between different codes are strictly bounded. Specifically, the discrete-time cross-correlation function (i.e., at integer multiples of bit duration) takes only the values of $-5/7$, $-1/7$, and $3/7$. These results agree with the fact that Gold codes have the highly desirable property that the cross-correlation spectrum of any pair of codes takes on only the three values [117].

$$R_{gg'}(\tau) = \begin{cases} -1 + 2^{\frac{n+1}{2}}, -1, -1 - 2^{\frac{n+1}{2}} & \text{, for } n \text{ odd} \\ -1 + 2^{\frac{n+2}{2}}, -1, -1 - 2^{\frac{n+2}{2}} & \text{, for } n = 2 \ (mod\ 4) \end{cases} \tag{3.2}$$

An important parameter that determines the multiplexing capacity and the error rate in a code-multiplexed system is the ratio of autocorrelation to cross-correlation between codes (i.e., processing gain). As expressed in Eq. 3.2, the processing gain increases by using longer codes (increasing n). To demonstrate this point, we generated 33 31-bit Gold sequences (n = 5) and calculated aperiodic cross-correlation of the 17th sequence with the other sequences in the set as well as its autocorrelation for random delays (Figure 3.5). Compared to results from 7-bit Gold sequences (Figure 3.4), these results demonstrate the increase in the processing gain of the system for longer Gold sequences. This also shows

that signals from code-multiplexed resistive pulse sensors designed based on longer Gold sequences can be distinguished with a higher signal-to-noise ratio.

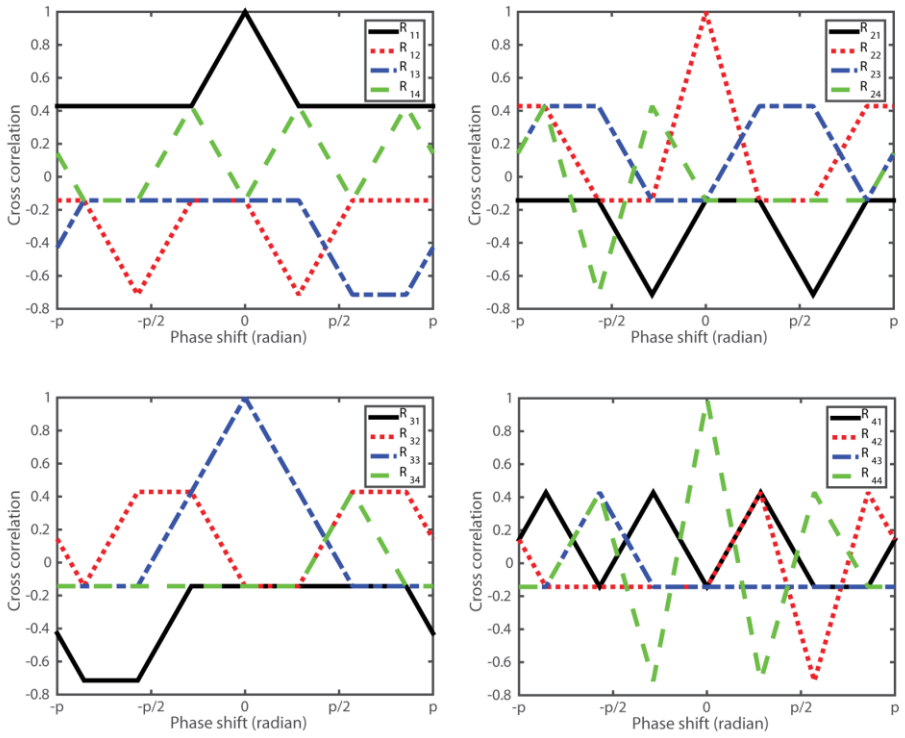

Figure 3.4 – Periodic auto- and cross-correlation of four 7-bit Gold sequences designed to encode resistive pulse sensors in our device

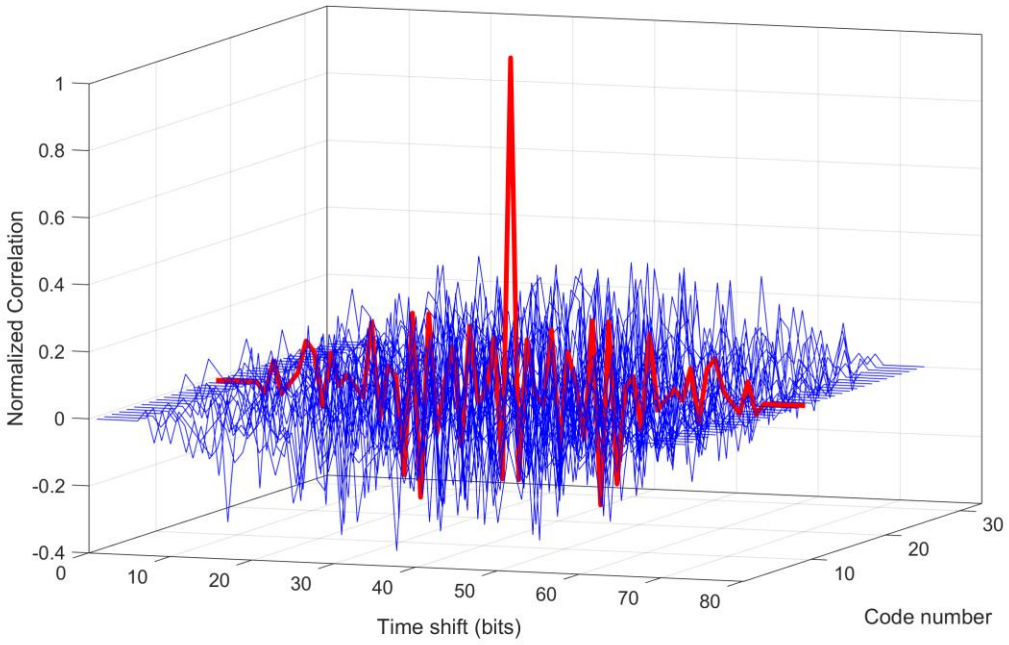

Figure 3.5 – Aperiodic auto- and cross-correlation of the 17th Gold sequence with all of the 33 sequences in a 31-bit Gold code set

3.2 Microfluidic chip design and operation principle

Our device is composed of micromachined surface electrodes on a glass substrate and a microfluidic layer aligned with them (Figure 3.6, left). We create an electrode network from three co-planar electrodes, a common electrode, and two coding electrodes to generate a binary output. By arranging these three electrodes in distinct spatial patterns at different nodes on the chip, we create code-multiplexed resistive pulse sensors. Because conduction between electrodes only occurs in the electrolyte-filled microfluidic channels, the order of electrodes in the microfluidic channels determines the sensor output. In each sensor, we set the order of electrodes based on the assigned digital code. Specifically, we place a coding-electrode finger in between two common electrode fingers for every bit to

be encoded in the sensor output (Figure 3.6, right). In this setting, the polarity of any bit is simply set by which (i.e., positive or negative) coding-electrode is used to encode it.

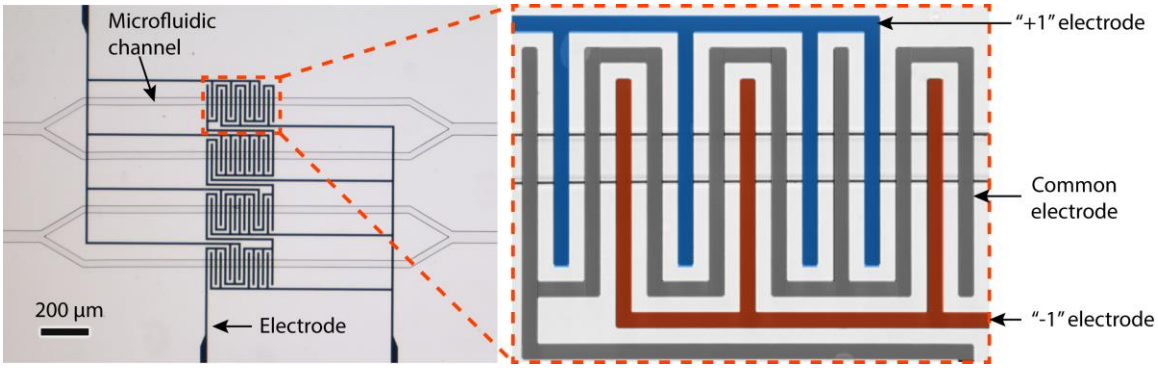

Figure 3.6 – The structure of the microfluidic chip. The left side shows an image of a fabricated Microfluidic CODES device with four code-multiplexed resistive pulse sensors, and the right side shows a false-colored close-up image of the sensor #1 that encodes "1010110".

From a circuit point of view, the overall sensor network can be represented as a lumped model with two variable impedances between the common electrode and the two coding-electrodes independent of the number of code-multiplexed sensors in our device (Figure 3.7, left). When the system is at rest (i.e., no particles), the two impedances are balanced, which we achieve by designing the sensor network to have the same total number of positive and negative coding electrodes. In operation, particles flowing in any microfluidic channel sequentially interact with electrodes and dynamically modulate the channel impedance intermittently unbalancing the circuit (Figure 3.7, right). We detect these changes by applying an AC signal to the common electrode and by measuring the differential current flow from the two branches of the circuit. As a result, a particle flowing over an encoded sensor produces a time waveform that is determined by the order of underlying electrodes.

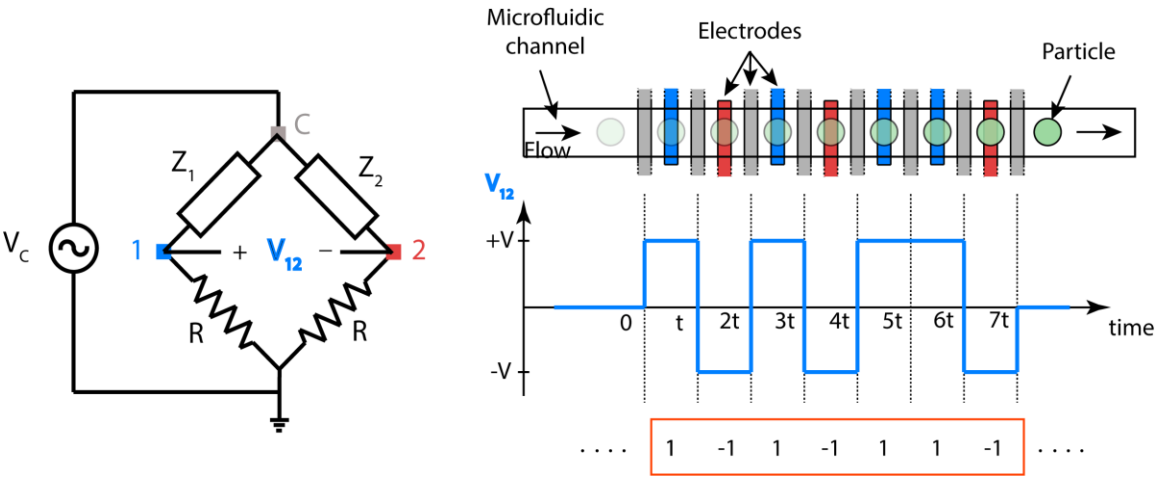

Figure 3.7 – Operation principle of the Microfluidic CODES. A lumped-model of the electrode network in a Microfluidic CODES device. Schematic showing the generation of a time waveform of resistive pulses as a cell flowing in the microfluidic channel sequentially interacts with micropatterned electrodes.

Differential measurement of impedance modulations in our device provides several advantages for our purposes. First, it rejects the common mode signal in the circuit, which cancels out the interference in the electrical measurement, thereby making the signals of interest easier to detect. Second, it enables us to generate bipolar code waveforms as the sensor output, which makes it easier to demultiplex code waveforms when they interfere due to multiple particles simultaneously interacting with the sensors. This is because bipolar signals can be designed to have smaller cross-correlation than unipolar signals [124,125]. In wireless communications, digital codes are routinely converted to bipolar signals using BPSK modulation [123]. In our device, BPSK modulation is physically implemented by measuring the differential impedance between the common electrode and the coding-electrodes. To balance the system, we use an equal number of positive and negative electrode fingers. Therefore, we design a digital code set with an equal number of 1's and 0's (Figure 3.8). With a balanced digital code set, our technique is not only more sensitive but also more robust to changes in fluid or material properties.

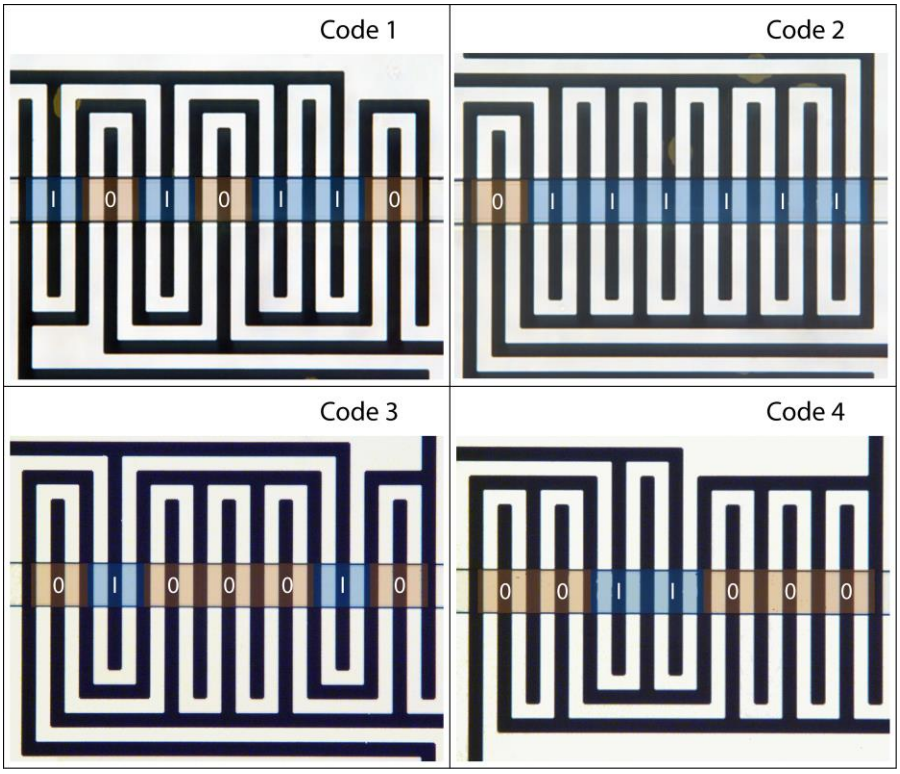

Figure 3.8 – The close-up images of the four sensors in the sensor network. The digital code set is specifically chosen to balance the system.

In addition to the design of the electrode layout, the design of the microfluidic layer is also critical to its proper operation. Unlike in a CDMA telecommunication network, in which signals are digitally generated based on stable clock signals, the temporal properties of our digital codes are determined by the flow speeds of individual cells. Thus, variations in the speed of the cell flow lead to differences in the duration of the digital code perturbing the favorable cross-correlation properties of the designed digital code set. To minimize such variations, we design our device so that fluid flows at the same rate in all of the microfluidic channels and remains constant across the coding region. The design of each microfluidic channel of our device consists of uniform cross sections with equal hydraulic resistance. The size of the microfluidic channel cross section is close to the size of the cell so that (1) the cell speed is less affected by the parabolic flow profile across the microfluidic

channel, (2) the total sensing volume is minimized, which reduces cell overlapping, and (3) cells remain close to the surface electrodes, which increases the sensitivity of the device.

3.3 The fabrication of the device

We fabricated the device in a cleanroom using a combination of surface micromachining and soft lithography and used a lift-off process to create coding electrodes on a glass substrate (Figure 3.9). We began the microfabrication process by coating a 4 in. borosilicate glass wafer with a 1.5 μm-thick negative photoresist and patterning it using optical lithography. Using e-beam evaporation, we deposited a 20 nm-thick chromium adhesion layer followed by an 80 nm-thick gold conduction layer on the patterned photoresist, etched a sacrificial photoresist layer in acetone under sonication, and diced the wafer into separate chips using a wafer saw. Separately, we fabricated the microfluidic layer of the device in polydimethylsiloxane (PDMS) using soft lithography and to fabricate the mold, we coated a 15 μm-thick SU-8 negative photoresist on a 4 in. silicon wafer and patterned it using photolithography. Onto this SU-8 mold, we then poured a PDMS prepolymer and a cross-linker mixed at a 10:1 ratio. Once degassed under vacuum, the PDMS was cured in an oven at 65°C for 4 hours and then peeled off of the SU-8 mold, on which we created inlet and outlet holes using a biopsy punch. To fabricate the final device, we activated a glass chip with micromachined surface electrodes and the PDMS microfluidic layer in an oxygen plasma, aligned under a microscope and bonded. An image of the final device appears in Figure 3.6.

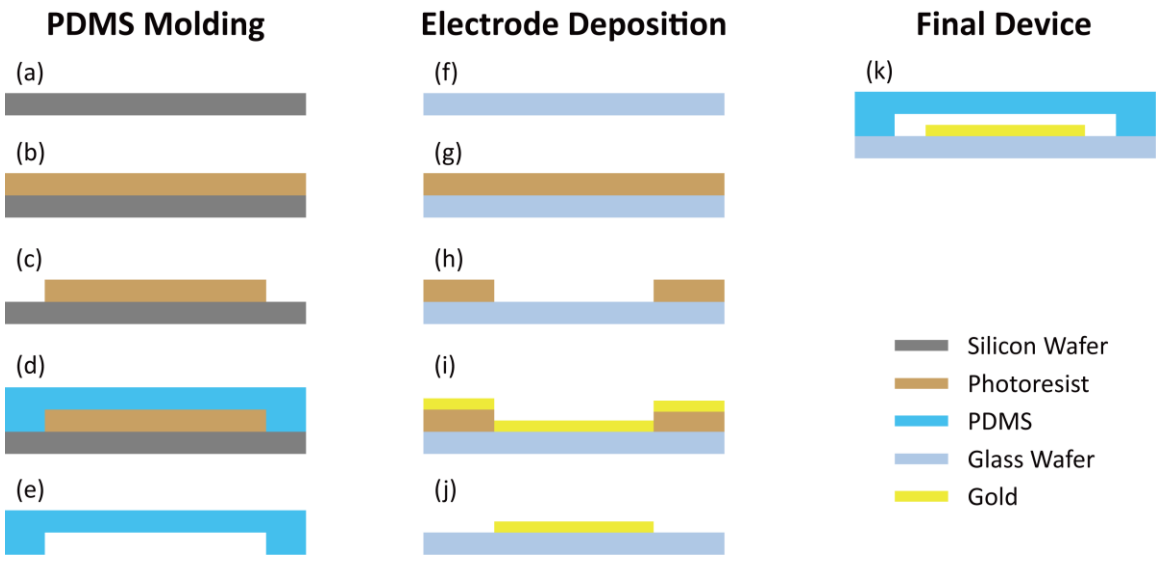

Figure 3.9 – The fabrication process of the microfluidic CODES chip. (a)~(e) The fabrication of the metal-coated PDMS microchannel. (f)~(j) The fabrication of the glass substrate with micropatterned surface electrodes. (k) Bonding of the two components to form the final device.

3.4 Experimental methods

We used cells suspended in phosphate buffered saline (PBS) as a model biological sample. Our measurement setup consisted of a syringe pump for driving the cells through the microfluidic chip, electronic hardware for acquiring data and processing raw sensor signals, and an optical microscope equipped with a high-speed camera for the visual analysis of cell flow in the microfluidic channels (Figure 3.10).

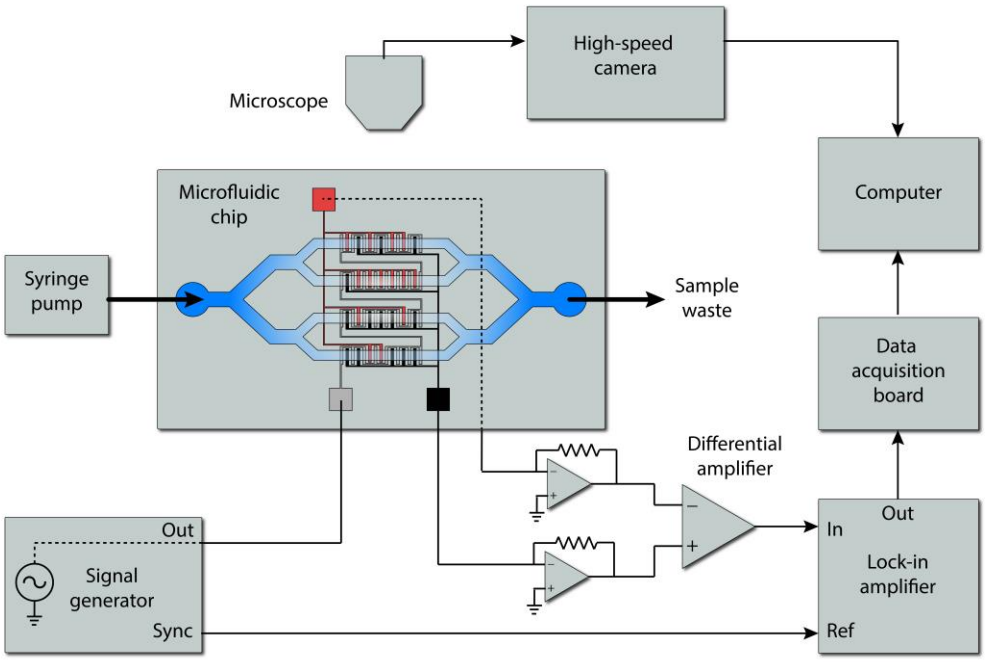

Figure 3.10 – Experimental setup used for our measurements. The cell suspension is driven through the microfluidic chip using a syringe pump. A bipolar electrical signal is obtained using a differential amplifier and sampled into a computer for decoding. High-speed optical microscopy is then used to validate decoded electrical signals.

We generated digital codes by detecting changes in the magnitude of electrical current as cells flow through the microfluidic channels. For this purpose, we excited the system from the common electrode with a sine wave at 400 kHz, specifically to bypass the double layer capacitance at the electrode-liquid interface. The current flow through the negative and positive electrodes was independently measured using two transimpedance amplifiers. These signals were then subtracted from each other using a differential amplifier to obtain a bipolar signal. Specifically, we subtracted the positive electrode signal from the negative electrode signal so that the reduced electrical current would lead to positive peaks in the output. The magnitude of this differential signal was measured using a lock-in amplifier. The lock-in amplifier output was then sampled at 1 MHz into a computer using a data acquisition board to decode digital codes.

Through a transparent glass substrate, we optically analyzed the cell flow through the coding electrodes to validate the acquired electrical signals. We obtained images of the microfluidic chip using an inverted optical microscope (Nikon Eclipse Ti-E) equipped with a high-speed camera (Vision Research Phantom v7.3). We recorded movies of cells at 8000 frames per second so that we could resolve them as they passed through the microfluidic channels within milliseconds. The recorded videos were then downloaded onto a computer to be analyzed frame by frame.

3.5 Results and discussion

Digital code signals corresponding to each of the four sensors are easily identified in the recorded electrical waveform. The measured code signals closely match with the designed digital codes (Figure 3.11, left). Deviations from ideal square pulses can be attributed to several factors, including the nonuniform electric field between the coplanar electrodes, spherical cell shape, and continuous (i.e., not pulsatile) flow of cells in the microfluidic channels.

To decode electrical signals, we first created a template library using experimentally obtained digital code signals corresponding to each sensor. The template library included four measured, normalized code signals and their computer-generated versions with varying durations to accommodate differences in flow speed between different cells. By correlating the recorded electrical signal with all of the templates in the library, we determined the specific template that maximized the amplitude of the autocorrelation peak. From this template, we obtained (1) the specific sensor the cell passed through, (2) the digital code signal duration and hence the cell transit time (Figure 3.11,

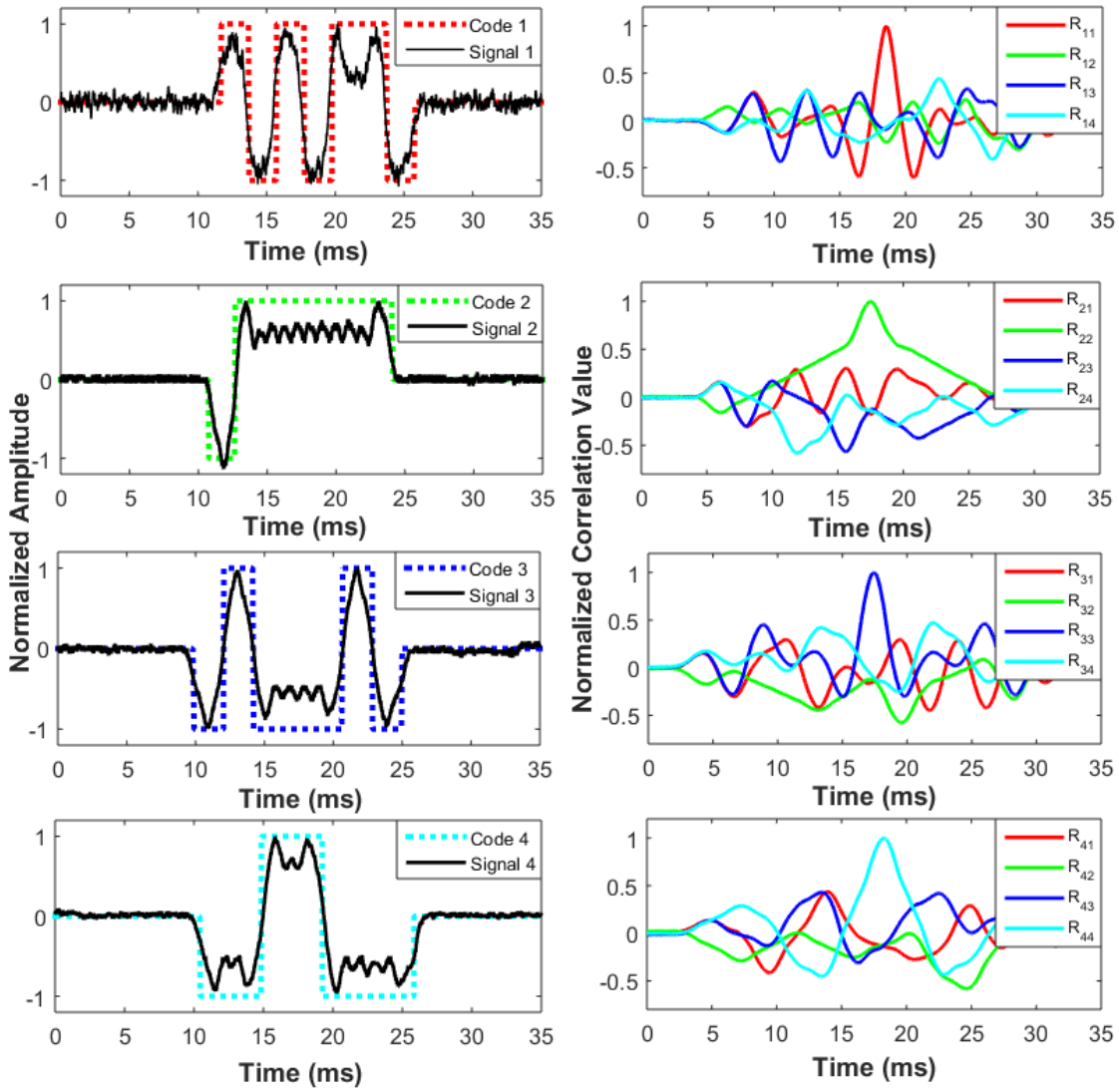

Figure 3.11 – Measured electrical signals as templates and their correlations. (a) The representative normalized digital code signals (templates) corresponding to each sensor are shown together with the corresponding ideal square pulse sequences. The signals are recorded as the cells are driven through the microfluidic device at 100 µL/h. (b) Each template signal is correlated with itself and three other template signals corresponding to other sensors. In each case, an autocorrelation peak can be identified because the digital codes for each sensor are specifically designed to be orthogonal to one another.

right). Note that an autocorrelation peak can robustly be identified in this process because the digital codes for each sensor are designed to be orthogonal to each other. Specifically,

the peak amplitude of the periodic cross-correlation between the 7-bit Gold sequences corresponding to two different microfluidic channels is bounded and can only be as high as ~40% of the autocorrelation peak theoretically.

An important feature of the microfluidic CODES technology is that it can also resolve cells at microfluidic sensors even when multiple cells simultaneously occupy the coding electrodes. When the cells simultaneously interact with the electrode network, the signals due to different cells interfere, and the recorded electrical signal cannot be readily associated with a single template corresponding to a specific microfluidic channel. Resolving such coincident cells, however, is particularly important for processing samples with a high cell density, where cells are more likely to coincide.

To demonstrate how microfluidic CODES can resolve coincident cells, we present an example that involved four coincident cells at four different sensors (Figure 3.12, 1st row, 1st plot). To resolve signals corresponding to individual cells, we developed an iterative approach based on a successive interference cancellation scheme used for multi-user detection in CDMA [126]. First, we determined the dominant autocorrelation peak corresponding to the strongest interfering signal by correlating the recorded waveform with the template library (Figure 3.12, 1st row, 2nd plot). Using the amplitude and time of the autocorrelation peak as well as the template used, we estimated the signal due to this specific cell (Figure 3.12, 1st row, 3rd plot). This estimated signal was then subtracted from the original signal, effectively removing the interference due to the largest cell (Figure 3.12, 2nd row, 1st plot). This process was iterated until the correlation of the template library with the residual signal did not produce a clear autocorrelation peak for any channel (Figure 3.12, 5th row, 2nd plot). Specifically, the process was terminated when none of the

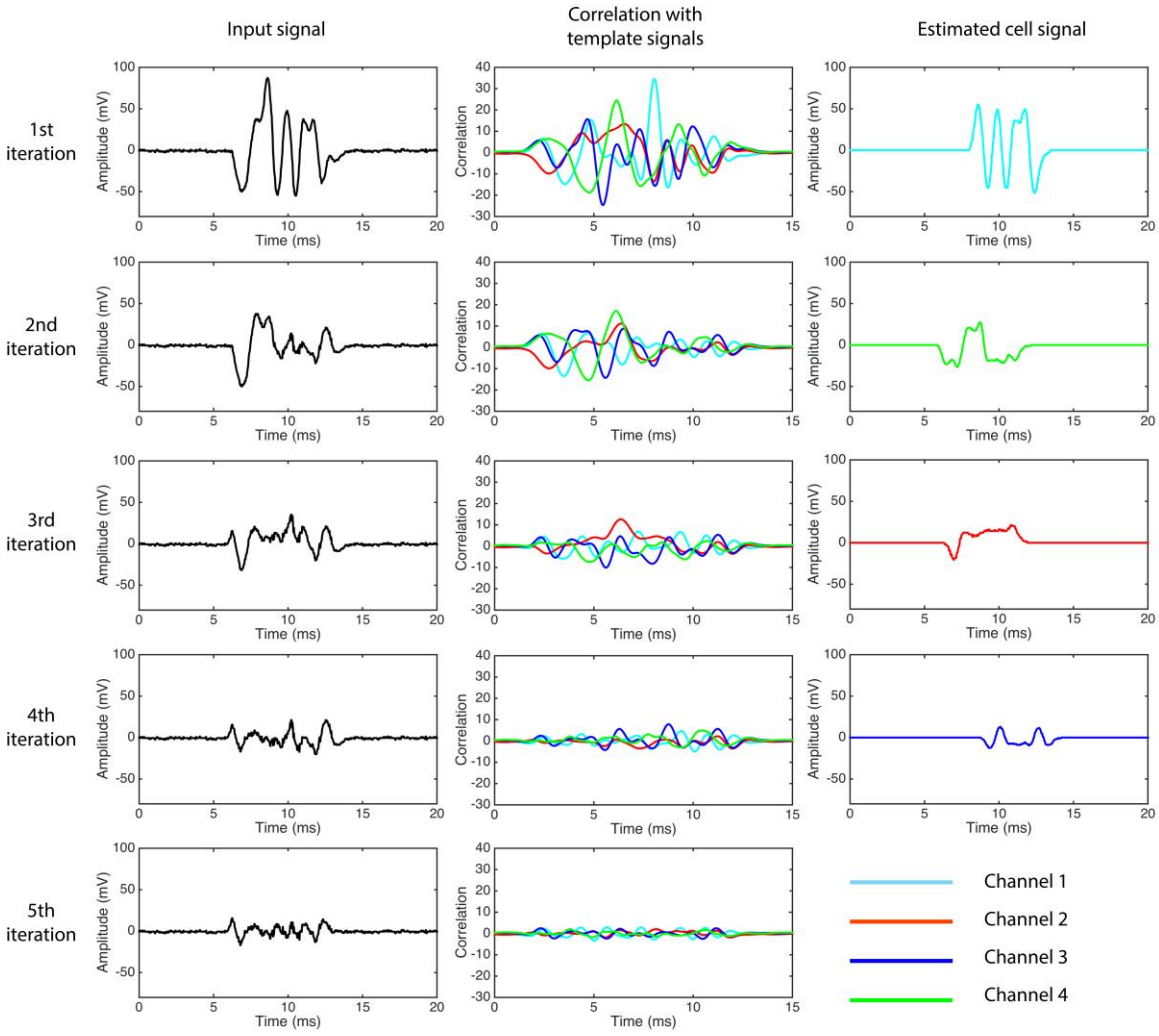

Figure 3.12 – Decoding the coincident signals with successive interference cancellation. (a) The input signal (left column) is correlated with the template library to identify the template that leads to the maximum correlation amplitude (center column). Using this template as well as the amplitude and time of the correlation peak, the signal due to the largest overlapping cell is estimated (right column). The estimated signal is then subtracted from the original signal, effectively canceling the interference due to the specific cell. The process is repeated until the residual signal does not resemble any of the templates in the library (i.e., correlation coefficient <0.5).

templates correlated with the normalized residual signal led to a correlation coefficient greater than 0.5. Following termination of the interference cancellation process, we ran an optimization process, where the amplitude and duration of estimated cell signals were refined to produce the best fit with the recorded electrical signal based on the least-squares

approximation (Figure 3.13(a)). At the end of this optimization process, we determined spatial information (the specific sensor the cell is at), the amplitude of the signal and the timing of each coincident cell (Figure 3.13(b)). Simultaneously recorded high-speed microscopy videos confirmed our results, showing that the sensor's cells were passing and also their timing was correctly determined (Figure 3.13(c)).

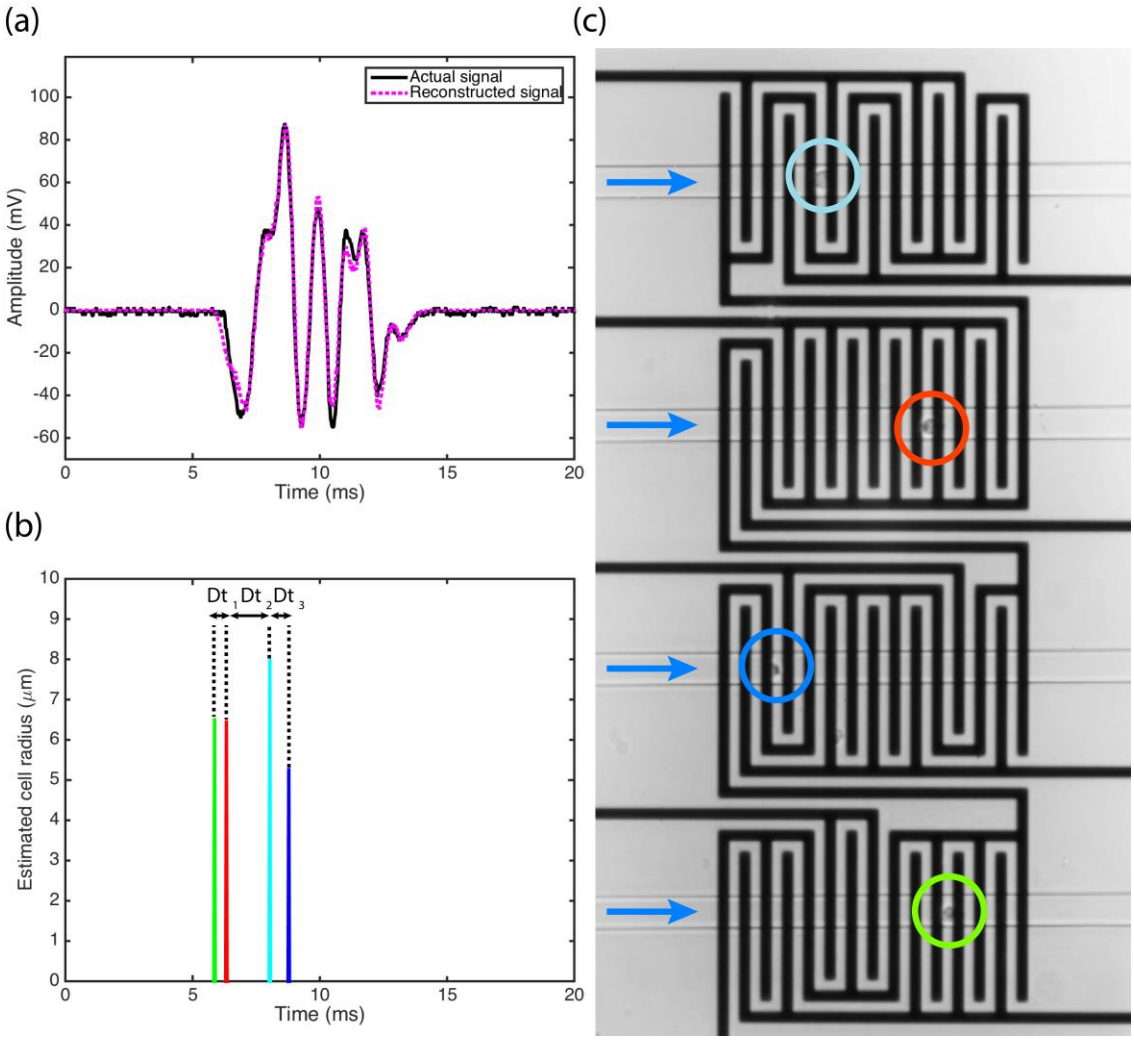

Figure 3.13 – Validation of the coincident signal decoding. (b) Cell signal amplitudes and durations are later optimized to obtain the best fit with the measured signal using least-squares approximation. (c) The optimization process produces accurate results for the timing and amplitude of signals (used to compute cell size using calibration data in Figure 3.14) corresponding to individual cells. (d) Simultaneously recorded high-speed microscopy video confirms the estimated results for the location, timing, and size of the cells.

Our iterative decoding approach is essential in processing samples containing particles with varying sizes such as biological samples. Successively canceling interference due to coincident cells allows us to accurately resolve smaller cells with weaker signals, which are otherwise buried in strong interfering signals from larger cells.

While Figures 3.12, 3.13 demonstrates a case of coincident cells at different sensors, it should be noted that cells coinciding at the same sensor could also be resolved. This is because the coinciding of cells at the same sensor simply corresponds to interference of the same digital code with its time-shifted form and can successfully be decoded using our approach outlined above.

In addition to discriminating between different sensors (i.e., spatial information), we also used the amplitude of the code waveforms from each sensor to orthogonally measure cell sizes. To achieve this, we first calibrated measured electrical signals with optically measured cell volumes using linear regression (Figure 3.14). Based on this calibration, we used calculated cell signal amplitudes in Figure 3.12 to estimate the corresponding cell size (Figure 3.13(b)). A comparison of measurements using microfluidic CODES with optically measured cell sizes in Figure 3.12 shows that we can accurately determine cell size even for coincident cells (Table 3.1).

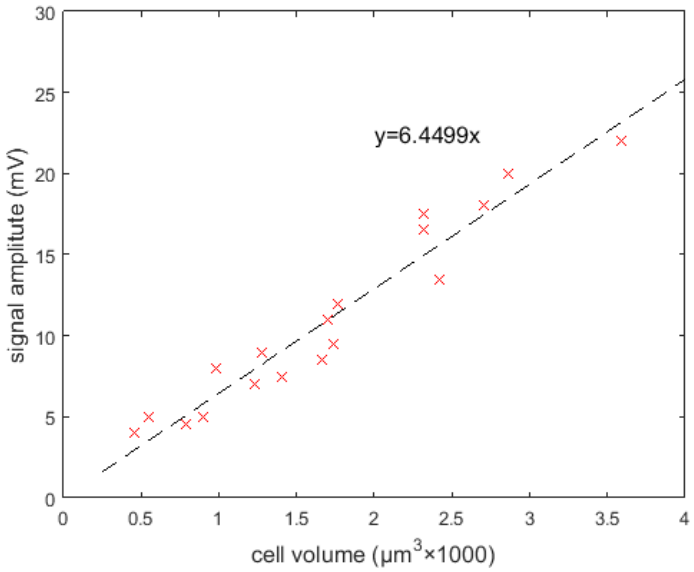

Figure 3.14 – Calibration of electrical signals' peak amplitude and cell volume. Cell radius is optically measured using high-speed optical microscopy and peak amplitude of the corresponding cell signal is recorded (x marks on the plot). Linear regression is used to model the relation between cell volume and electrical signal peak amplitude.

Table 3.1 – Comparison of electrically and optically measured parameters of Figure 3.13

Measurement type	r_{ch1} (μm)	r_{ch2} (μm)	r_{ch3} (μm)	r_{ch4} (μm)	Δt_1 (ms)	Δt_2 (ms)	Δt_3 (ms)
Electrical	8.01	6.49	5.30	6.55	0.465	1.705	0.744
Optical	8.32	6.77	5.68	7.04	0.375	1.625	0.750

The timing of cell passage through each sensor can also be orthogonally determined using microfluidic CODES. This is because Gold sequences (or pseudorandom noise sequences in general) are sensitive to timeshifts and produce sharp autocorrelation peaks at zero time delay. A comparison of our estimates using microfluidic CODES with the results obtained from the simultaneously recorded high-speed video with a known frame rate shows that the time differences between the coincident cells in Figure 3.13 can accurately be determined (Table 3.1).

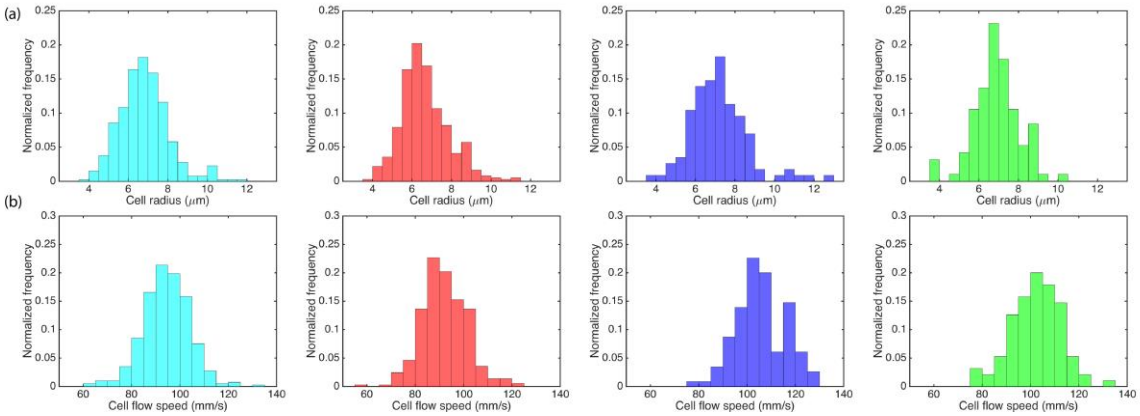

Figure 3.15 – Orthogonal measurement of cell size and speed at the four sensors. Histograms of the calculated cell radius (a) and cell flow speed (b) as the cells are driven at 1000 µl h^{-1} through the microfluidic channels. The recorded electrical waveform is processed using the algorithm outlined in the text. The calculated cell parameters corresponding to the microfluidic channel #1 (cyan), #2 (red), #3 (blue) and #4 (green) are grouped in separate histogram plots.

To demonstrate the performance of our technique over a large number of cells, we processed a model biological sample with a density of 4×10^5 cells mL^{-1}. We analyzed the recorded electrical signal corresponding to more than 1000 cells using MATLAB and decoded individual digital codes as follows: using a low-pass filter, we first removed high-frequency noise (>2.5 kHz) in the recorded electrical signal. In the filtered signal, the time windows where the signal power is above a certain threshold (signal-to-noise ratio (SNR) > 12 dB) were identified as sensor activity. Each event was then individually analyzed using the iterative algorithm described above. By comparing our results with the simultaneously recorded high-speed microscopy video, we determined that we can identify each cell and the microfluidic channel it passed through with a 96.15% (973/1012) accuracy. In this analysis, success rates for detecting non-coincident and coincident cells were 98.71% (688/697) and 90.48% (285/315), respectively. Using calibration parameters (Figure 3.14), we also measured the size and flow speed of cells in our analysis (Figure 3.15). Our cell

size measurement results match with the optically measured cell size distribution (Figure 3.16).

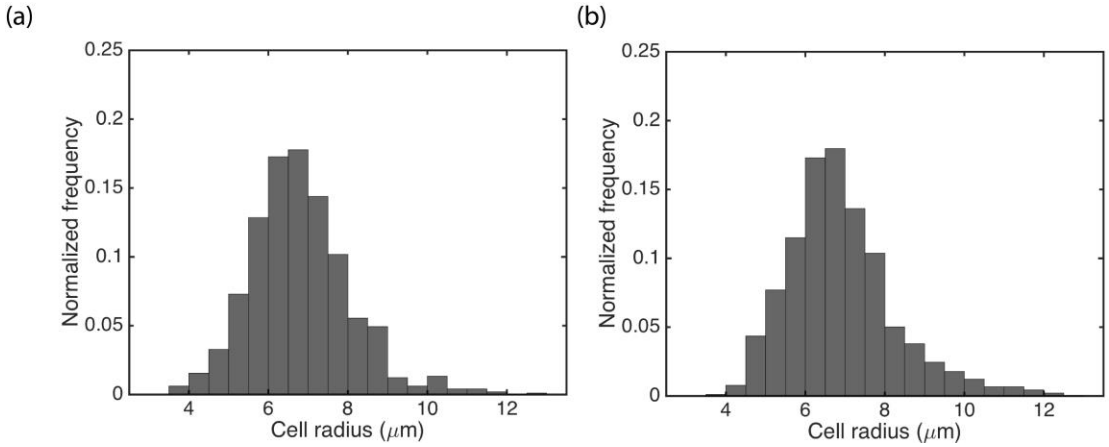

Figure 3.16 – Comparison of electrically (a) and optically (b) measured cell size distribution of HeyA8 human ovarian cancer cell line. Electrical measurements in this plot are obtained by combining cell size histograms from all sensors in Figure 2.15. A close match between histograms demonstrates the accuracy of our measurements.

Finally, microfluidic CODES can be scaled to incorporate more microfluidic channels. This is achieved by assigning each microfluidic channel a code distinguishable from others. For this purpose, larger digital code sets with favorable correlation properties can be designed by using longer (i.e., more bits) codes. Longer codes are less prone to interference from other codes and can therefore be distinguished from each other with higher accuracy. Furthermore, a key parameter that determines the performance and also the scalability of our sensor is the sample cell density. More microfluidic channels covering a larger sensor area will increase the likelihood of coincident events and hence the interference. The maximum number of coincident cells that can be resolved using our technology depends on several factors including the digital code set, the detection algorithm, the design of the microfluidic chip as well as the electronic noise and will

ultimately determine the sample cell density that can be processed reliably. These issues will be further discussed in Chapter 5.

3.6 Conclusions

Combining the techniques from telecommunications and microfluidics, we have introduced the microfluidic CODES technology, a scalable electronic sensor to orthogonally detect particles at multiple locations across a microfluidic device from a single electrical output. The microfluidic CODES relies on multiplexing an array of micromachined Coulter counters, each designed to produce a distinct digital code when a particle is detected. These digital codes are developed using the same principles of CDMA telecommunication networks and can be uniquely recovered through simple mathematical calculations. We demonstrated that our technology could readily be applied to detect human ovarian cancer cells on a multi-channel microfluidic chip. Importantly, our technology can also resolve particles with >90% accuracy if they coincide in time, a feature that is required to process samples with a high particle density. Microfluidic CODES offers a simple, all-electronic interface for tracking particles on microfluidic devices and is particularly well suited to create integrated, low-cost lab-on-a-chip devices for cell- or particle-based assays that are needed for point-of-care tests in resource-limited settings.

CHAPTER 4. THE MODELING OF MICROFLUIDIC CODES [127]

In a code-division multiplexed network such as a Microfluidic CODES device, it is crucial that each source in the network is assigned a distinct code that can reliably be distinguished from others. This requires that (1) we design a code-set, in which individual codes can computationally be recovered even if they interfere with others in the set when multiple sources are actively transmitting; (2) based on this code-set, we design a sensor network architecture that produces the desired signal waveforms. After the building of the code set proper for our applications, in this chapter, we develop an equivalent circuit model for a network of code-multiplexed resistive pulse sensors to accurately predict the sensor output based on the microfluidic device geometry and sample properties. In our model, we first use the Foster-Schwan model and conformal mapping to model the cell-electrode interaction in a non-uniform electric field. We then develop an equivalent circuit model that is dynamically reconfigured to model cell flow over the micromachined surface electrodes. Using electrical circuit simulators, we solve for the steady-state current flow in the equivalent circuit to construct time waveforms. Finally, we compare our results with experimentally obtained signals using cell lines. Overall, the modeling framework presented here will enable the design of code-division multiplexed resistive pulse sensors optimized to produce desired waveform patterns to ensure reliable and efficient decoding in a code-division multiplexing scheme.

4.1 Foster-Schwan model

We modeled the operation of our microfluidic device by developing an electrical circuit model for the cell-electrode interaction. In this model, we used the Foster-Schwan

model, which is commonly employed to estimate the electrical properties of cells suspended in a liquid medium [128,129]. In the previous work [64,131-134], the analysis typically involved one pair of electrodes, and the Foster-Schwan model was strictly used to model the scenarios when the cell is at the midpoint between two electrodes. Besides including a large number of electrodes, our device requires modeling of the cell-electrode interaction for arbitrary cell position within the microfluidic channel to simulate dynamic sensor waveforms with sufficient temporal resolution. To solve these unique challenges, we used conformal mapping to partition cells and used circuit simulators for large-scale electrical network analysis.

In the Foster-Schwan model, a cell in a liquid is modeled as a serially connected cytoplasm resistance (R_i) with membrane capacitance (C_{mem}) in parallel with the medium resistance (R_m) and capacitance (C_m) (Figure 4.1) [128].

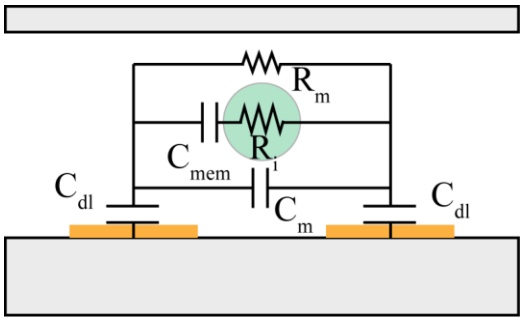

Figure 4.1 – The schematic of the Foster-Schwan model. The cell is modeled as four electrical components.

Each of these components depends on the material properties and the device geometry as given by

$$R_m = \frac{1}{\sigma_m \left(1 - \frac{3\Phi}{2}\right) G_f} \tag{4.1}$$

$$C_m = \varepsilon_\infty G_f \tag{4.2}$$

$$C_{mem} = \frac{9}{4} \Phi R C_{mem,0} G_f \tag{4.3}$$

$$R_i = \frac{4(\frac{1}{2\sigma_m} + \frac{1}{\sigma_i})}{9\Phi G_f} \tag{4.4}$$

where σ_m and σ_i are the conductivity of the medium and the cytoplasm, respectively. Φ is the volume fraction the cell occupies in the medium, G_f is the geometry constant, $C_{mem,0}$ is the cell membrane capacitance per unit area, and ε_∞ is the limiting high-frequency permittivity of the suspension which is given by

$$\varepsilon_\infty = \varepsilon_m [1 - 3\Phi \frac{\varepsilon_m - \varepsilon_i}{2\varepsilon_m + \varepsilon_i}] \tag{4.5}$$

according to Maxwell mixture theory [128,135], where ε_m and ε_i are the permittivities of the medium and cytoplasm, respectively.

To construct our model, we first divide each microfluidic channel into smaller unit blocks based on the electric field distribution dictated by the arrangement of coplanar electrodes (Figure 4.2). According to the different types of interaction between a cell and unit blocks, we consider four distinct scenarios that occur as the cells flow over coding electrodes: (1) no cell in a unit block, (2) a cell in one unit block, (3) a cell shared by two

neighboring unit blocks (i.e., a cell is only partially in one unit block). The electrical field distribution in the outermost unit blocks is different from that in inner unit blocks, so we also consider (4) a cell in an outermost unit block, as another distinct scenario.

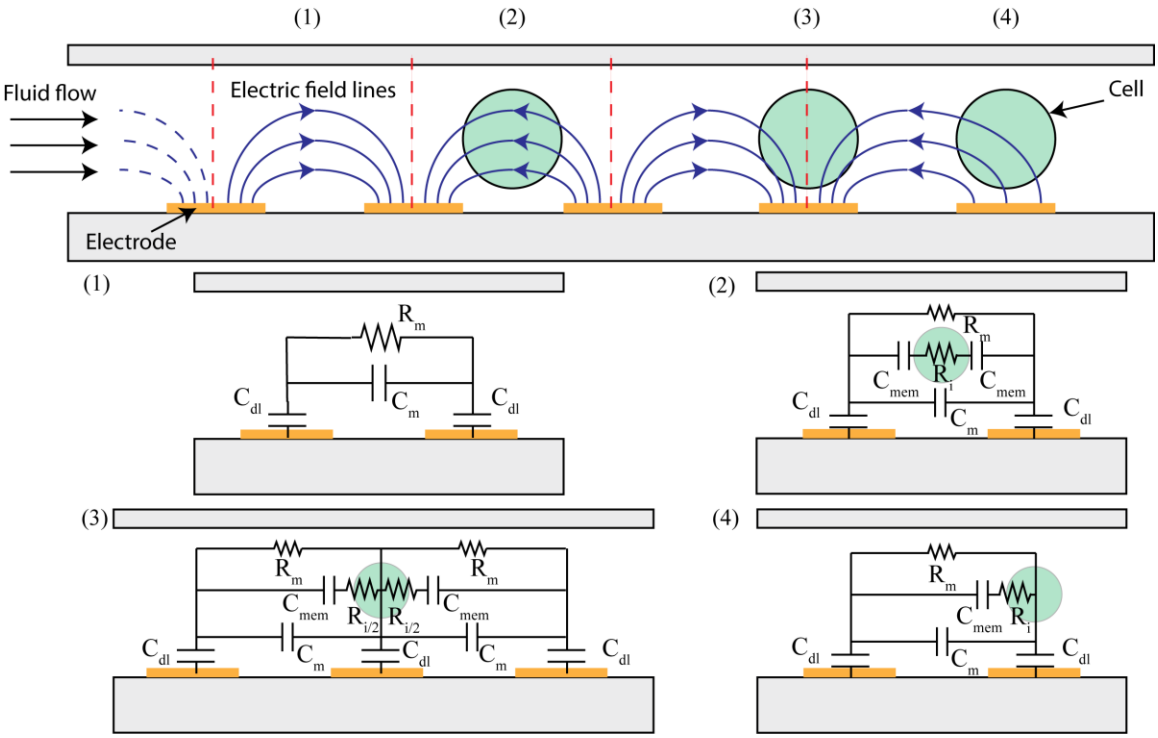

Figure 4.2 – Electrical modeling of the interaction between surface electrodes and cells (a) four different scenarios considered in modeling the system based on the cell position in the microfluidic channel and the circuit models for each of them. The cases are: (1) no cell in a unit block, (2) one cell in one unit block, (3) one cell shared by two neighboring unit blocks, and (4) one cell is in an outermost unit block.

In the scenario (1), the model only includes a parallel resistor (R_m) and a capacitor (C_m) representing the electrical properties of the medium (Figure 4.2(1)). In the scenario (2), the cell is represented by a serially connected resistor (R_i) and a capacitor (C_{mem}) in parallel to the medium resistor (R_m) and capacitor (C_m) (Figure 4.2(2)). In the scenario (3), the cell simultaneously interacts with the three electrodes. We, therefore, divide the cell into two, and model each electrode pair separately (Figure 4.2(3)). In the scenario (4), the

cell is modeled in the same way as in the scenario (2), but we also considered the differences in the spatial distribution of the electric field in contrast to the inner electrodes. Our model neglects the outermost traces due to the large gap and hence larger impedance between them and coding electrodes. For each scenario, we also included the electric double layer capacitance (C_{dl}). The double layer capacitance represents the capacitive effect due to the accumulation of electrolyte ions on the electrode surface and depends on the surface area of the electrodes [136].

4.2 Conformal Mapping of Non-uniform Electric Fields

To calculate the values of individual elements in the circuit model, we first need to calculate two parameters: the geometry constant (G_f) and the cell volume fraction (Φ). To achieve this, we use a conformal mapping approach to account for the non-uniform electric field distribution due to coplanar electrodes.

4.2.1 The calculation of the geometry constant

In our model, G_f is the geometry constant (also referred to as the cell constant in the literature 137-139) of a pair of electrodes. While for two parallel counter-facing electrodes, G_f is simply calculated by dividing the electrode surface area by the distance between them, coplanar geometry requires a conformal mapping approach. Previously Jacobs et al. introduced a method to calculate the G_f for the coplanar electrodes with semi-infinite electric field distribution [137] and Linderholm et al. expanded this work by developing a three-step method applicable to the coplanar electrodes' geometries with finite channel height [140]. Both approaches consider only a single pair of electrodes.

While Olthuis et al. calculated G_f for a multiple-electrode geometry [138], his solution assumes a channel filled with homogenous media and therefore cannot directly be used to model cell flow over the electrodes. To model our device, we first partition the microfluidic channel into small blocks based on electric field distribution, and assume there is no electrical coupling between individual blocks. We then calculate G_f for each block individually using a conformal mapping approach, and transform the non-uniform electric field distribution in our device to a plane that it can be represented as a uniform electric field (Figure 4.3).

Our unit block contains the part of the microfluidic channel in between the midpoints of two adjacent coplanar electrodes. For the conformal mapping process, we first place the unit block in a complex *Z*-plane such that it is centered at the origin (Figure 4.3(a)). Due to the symmetry of the problem, we assume the left semi-plane is identical to the right semi-plane for our uniformly arrayed electrodes. As such, we only consider half of the geometry in our calculations and divide the result by 2 to calculate the G_f for the entire unit block. To simplify our calculations, we also assume the problem can be treated as a semi-infinite rectangular geometry for conformal mapping. Our assumption is justified by the fact that the fringing electrical field outside the geometry is small. The simplified geometry of the unit block (Figure 4.3(b)) based on these assumptions is then solved using the conformal mapping introduced in ref. 140 and 141.

Coordinates for the two half electrodes in Figure 4.3(b) are given by $z_1 = h/2$, $z_2 = -h/2$, $z_3 = -h/2 + ig/2$, and $z_4 = -h/2 + i(g + w)/2$, where h is the height of the microfluidic channel, w is the width of our electrodes, and g is the distance between

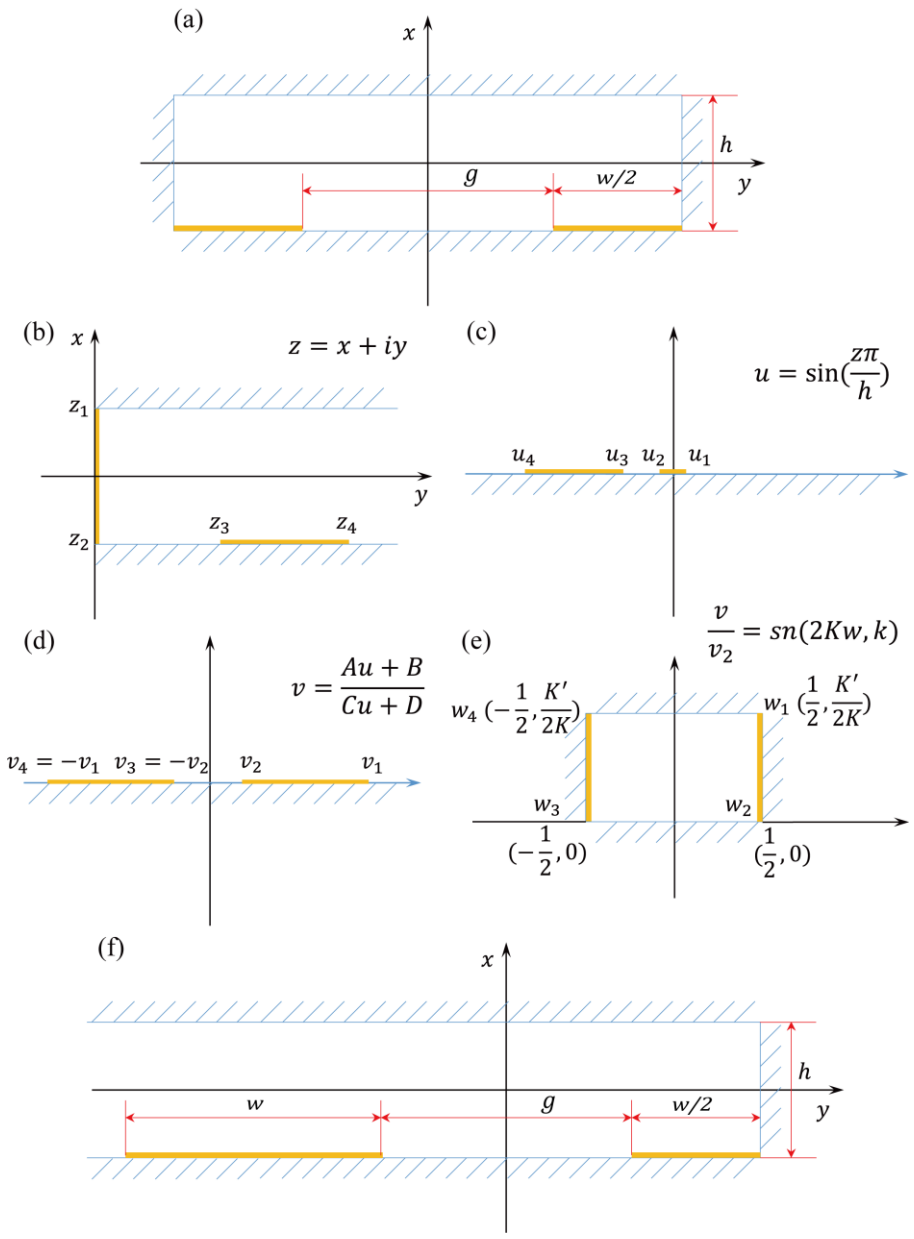

Figure 4.3 – Three-step conformal mapping process to account for the non-uniform electric field distribution due to coplanar electrodes (a) Cross-sectional geometry of an inner unit block. (b) Simplified semi-infinite rectangular geometry of the half unit block constructed based on the symmetry of the problem. (c) The result of sine-transformation to convert the electrode boundary coordinates in (b) into the real axis of the U-plane. (d) The result of the bilateral transformation to convert the electrode geometry in (c) into isometric lines. (e) The Schwarz-Christoffel mapping process to convert the electrodes in (d) into parallel plate electrode geometry. (f) The cross-sectional geometry of an outermost unit block.

two electrodes. First, we use the Schwarz-Christoffel mapping (SCM) of a trigon by using a sine-transformation [142], namely

$$u = \sin\left(\pi \frac{z}{h}\right) \tag{4.6}$$

At the end of this process, the left side wall and the bottom electrodes could both be placed on the same real axis of the *U*-plane, and all the points inside the semi-rectangular are mapped to the top semi-plane, as shown in Figure 4.3(c). Then, we apply a bilinear transformation, described as

$$v = \frac{Au + B}{Cu + D} \tag{4.7}$$

We determine A, B, C and D in Equation 4.7 to transform u_1, u_2 and u_3, u_4 into *V*-plane and to create two equal-length segments that are symmetric around the vertical axis (Figure 4.3(d)).

Next, we perform another SCM operation to transform the coplanar geometry in the *V*-plane into a planar geometry in *W*-plane to simplify calculations (Figure 4.3(c)). The relation between the *V*-plane and *W*-plane is given by

$$\frac{v}{v_2} = sn(2Kw, k) \tag{4.8}$$

where $sn(.,k)$ is the Jacobi elliptic function with elliptic modulus k. In our case, $k = \frac{v_2}{v_1}$, and the geometry constant for the *W*-plane geometry can be expressed as

$$G_f' = \frac{K'(k)}{2K(k)} \tag{4.9}$$

where $K(k)$ is the complete elliptic integral of the first kind, and $K'(k)$ is the complete elliptic integral of the first kind taken in the complementary modulus k'.

$$K(k) = \int_0^1 \frac{dt}{\sqrt{(1-t^2)(1-k^2t^2)}} \tag{4.10}$$

$$K'(k) = K(k') \tag{4.11}$$

$$k' = \sqrt{1-k^2} \tag{4.12}$$

To calculate the final block constant, we consider the full unit block as a serial connection of two half blocks, and also take the length (l) of the electrodes into consideration [137]. The block constant of our device is then given by

$$G_f = \frac{lK'(k)}{4K(k)} \tag{4.13}$$

Finally, note that the electric field distribution due to the outermost coding electrodes is different than the inner electrodes. Specifically, the field lines from the adjacent half-electrode are mapped to cover the whole surface of the outer electrode (Figure 4.2). We address this difference by defining a unit cell, which includes the whole outermost electrode and half of the adjacent electrode (Figure 4.3(f)). We also assume that the field lines are perpendicular to the bisecting plane positioned at the midpoint between two

electrodes. Under these assumptions, the final block constant of the outermost unit block in our device is given by

$$G_{f,out} = l/\left(\frac{2K(k)}{K'(k)} + \frac{2K(k_{out})}{K'(k_{out})}\right) \tag{4.14}$$

4.2.2 The calculation of volume fraction

Next, we need to calculate volume fraction Φ occupied by the cell and how it changes as the cell flows in the microfluidic channel. For a parallel-electrode geometry with uniform electric field distribution, the volume fraction can be calculated by dividing the volume of the cell by the volume of the unit block [143]. However, this approach cannot be used for a non-uniform electric field distribution between coplanar electrodes. In a geometry with high volume fraction and non-uniform field such as our device, we need to use a corrected equation based on Schwarz-Christoffel mapping [144]. This equation, however, is only applicable to calculate the volume fraction of a particle when it is exactly positioned at the midpoint between electrodes.

To calculate the volume fraction Φ occupied by the cell in our device, we developed a graphical conformal mapping method that allows us to calculate the volume fraction occupied by the cell in a non-uniform electric field and importantly at arbitrary positions along the microfluidic channel (e.g., when the cell is at different vertical positions above the coplanar electrodes or is asymmetrically positioned between the pair of coplanar electrodes). Our method is based on the graphical determination of the cell size in a grid formed by electric field lines and equipotential lines using image processing techniques. For uniform field distribution, the grid is uniform and the volume fraction is determined

from the physical volume of the cell. For the non-uniform field distribution, the grid is distorted and the volume fraction cannot directly be obtained from its physical size.

In the graphical conformal mapping process, we first simulate a 2D electric field distribution in the microfluidic channel between coplanar electrodes using COMSOL Multiphysics software. We then overlay a circle, representing one of the cross-sections of a cell, with the grid formed by the electric field and equipotential lines, and graphically quantify its area (i.e., how many grid units it encompasses) in this grid using a custom-built program (Figure 4.4). We repeat this process for circles of varying diameters, which represent different cross-sections of a spherical cell. Finally, we calculate the cell occupation fraction by integrating the calculated areas for different cross-sections. Using our graphical conformal mapping method, we found that the cell, when it is directly above one of the electrodes, has higher occupation fraction than a cell in between the coplanar electrodes. For example, a 14 μm-diameter cell flowing in our device has a volume fraction of 15.20% when it is directly above the electrode (Figure 4.4, bottom), and 12.62% when it is at the midpoint between two electrodes (Figure 4.4, top).

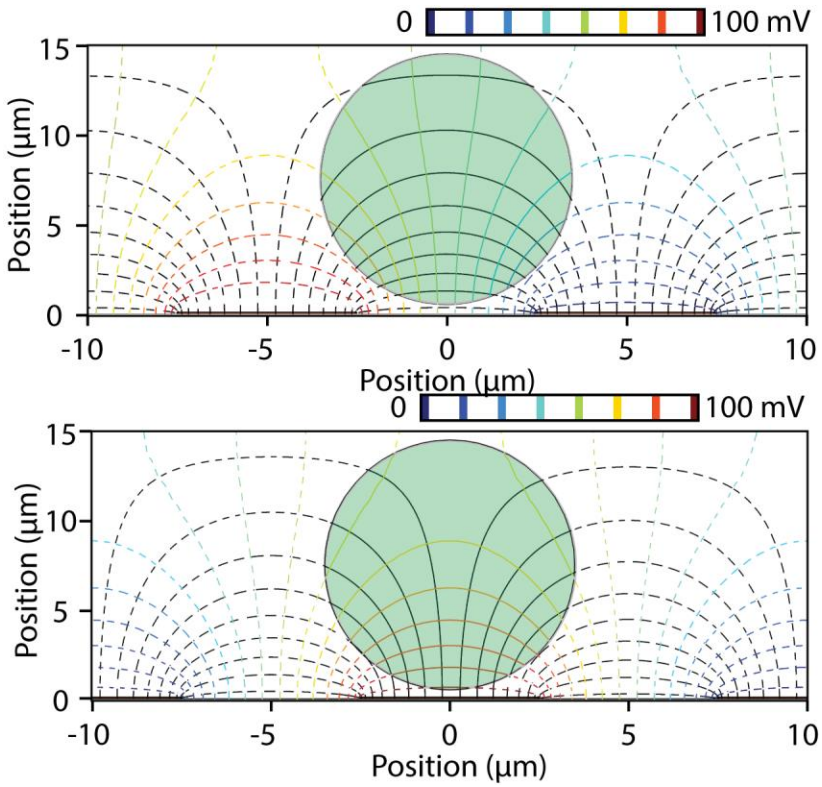

Figure 4.4 – Graphical conformal mapping of volume fraction for the case when a cell is in between two electrodes (top) and directly above an electrode (bottom)

4.3 The equivalent circuit model of the sensor network

We combined unit circuit blocks to create an equivalent circuit model for the whole code-multiplexed resistive pulse sensor network. For example, an equivalent circuit configuration representing a single time point, when 5 cells are simultaneously interacting with the sensor network at different locations is demonstrated in Figure 4.5. The sensor network includes four code-multiplexed resistive pulse sensors, each encoded based on 7-bit Gold sequences, and contains 60 electrode pairs (Figure 4.5, top). The locations of 5 cells on the sensor network at the given time point determine which of the possible circuit configurations (Figure 4.2) each unit block adopts (Figure 4.5, bottom). In our equivalent circuit model, we also included the resistance of electrode traces and used previously

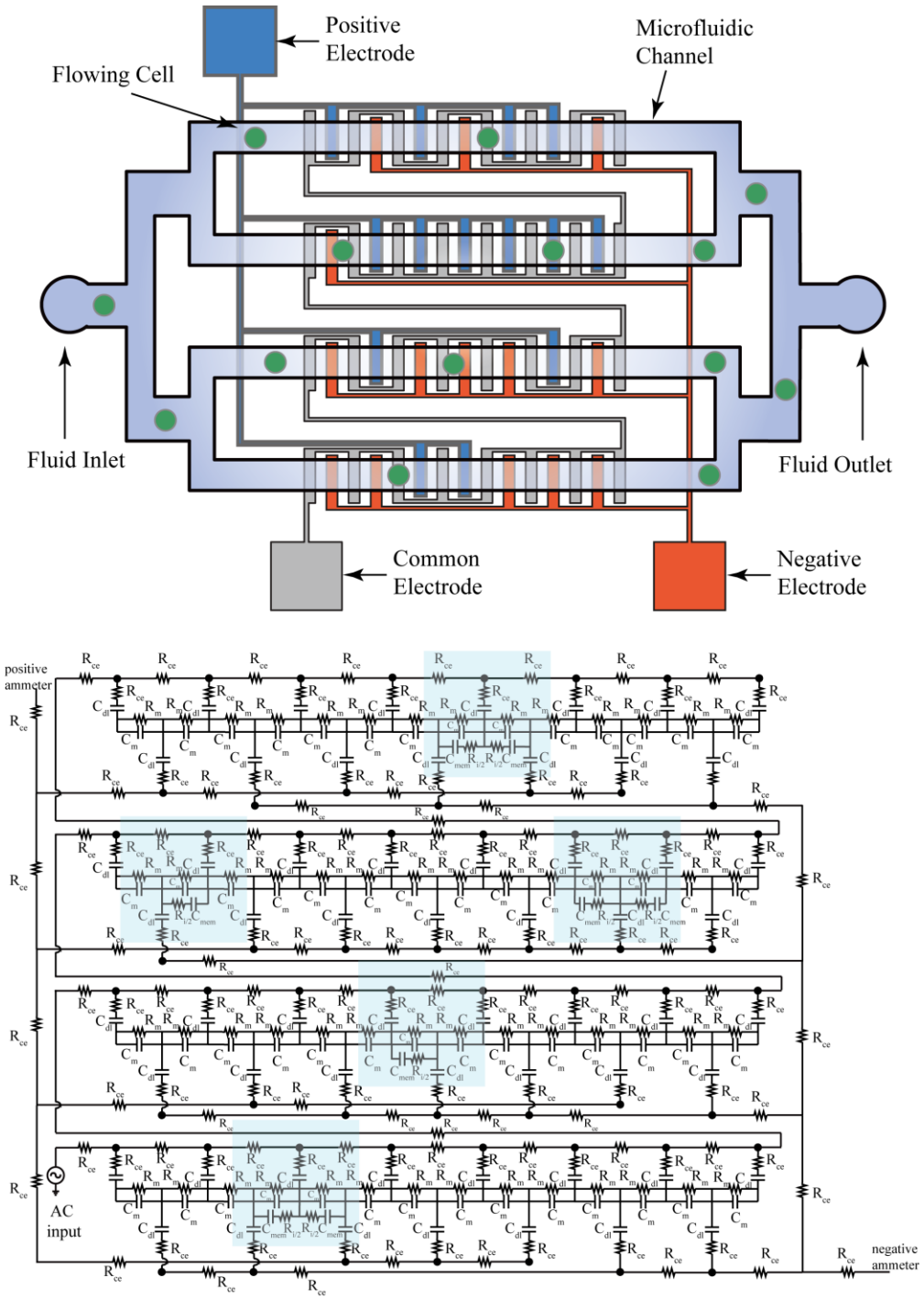

Figure 4.5 – Equivalent circuit model for the whole code-multiplexed resistive pulse sensor network. A schematic (top) and the corresponding equivalent circuit model (bottom) for a hypothetical case where 5 cells are simultaneously in the sensing region at a given time-point. Each cell in the equivalent circuit model is represented using one of the unit blocks in Figure 4.2 based on the position of the cell.

reported resistivity of thin polycrystalline gold films [89] to calculate the resistance (R_{ce}) values.

To simulate the cell flow in the microfluidic channel, we simulated a series of circuit configurations, where the circuit components are sequentially updated to represent the changing cell position at different time-points. While our conformal mapping approach can be used to model the cell-electrode interaction at an arbitrary position along the microfluidic channel, we discretized the analysis by updating the cell position in 2.5 μm steps. This resulted in 117 different equivalent circuit configurations representing the whole sensor network for a single cell traversing the 290 μm wide coding section in our device. The first and the last circuits of the set represented the time points where the center of the cell coincides with the edges of the first and the last electrode, respectively. To simulate coinciding cells with different speeds, a time base was chosen based on one of the cells, and the location of other cells was snapped to the closest grid point. We used MATLAB Simulink to solve for the current flow in each of the equivalent circuit models and calculated the differential current flow from positive and negative electrodes to calculate the sensor output. We then created estimated signal waveforms by combining current values calculated for different cell positions. The device geometry parameters and physical constants used in our model are given in Table 4.1. Table 4.2 provides the calculated values of circuit components used to model the interaction of a 14 μm-diameter cell with coplanar electrodes at representative locations.

Table 4.1 – Parameters and constants used in the model

Parameter or Constant	Value
Channel dimension	
Channel height	15 μm
Channel width	30 μm
Electrode width	10 μm
Electrode gap	10 μm
Electrical properties	
Media conductivity	1.4 S/m
Media relative permittivity	80
Cytoplasm conductivity	0.5 S/m
Cytoplasm relative permittivity	60
Cell membrane capacitance $C_{mem,0}$	0.2001 $F \cdot m^{-2}$
Vacuum permittivity ε_0	8.854e-12 $F \cdot m^{-1}$
Thin gold layer conductivity	8e-8 Ω·m

Table 4.2 – Impedance values for representative locations (values for a 14 μm-diameter cell)

	R_m	C_m	R_i	C_{mem}
No cell in one block	42.548 kΩ	0.011890 pF		
Cell in the middle of two electrodes	52.487 kΩ	0.011482 pF	494.30 kΩ	0.66794 pF
Cell on electrode	48.024 kΩ	0.011645 pF	820.86 kΩ	0.40222 pF

4.4 Finite element analysis

To compare with the results from our equivalent circuit model, we simulated the sensor operation using finite element analysis. In this analysis, we used COMSOL Multiphysics v5.2 AC/DC module to perform a steady-state analysis of current flow between coplanar electrodes for a number of cell positions along the microfluidic channel. We only considered a single 7-bit coded resistive pulse sensor. The simulation model consisted of a rectangular block that is 15 μm high, 30 μm wide and 320 μm long to represent the microfluidic channel. To model the electrodes in the channel, we defined a total of 15 10 μm × 30 μm sized surface patches separated by 10 μm gaps at the bottom

surface of the rectangular block. The electric potential of individual electrodes was set based on the electrode type (i.e., common, positive or negative) as a boundary condition. In order to emulate the electrical double layer (EDL) effect in COMSOL, we used a technique previously introduced in references 146 and 147. The EDL was modeled as a 0.5-μm thick rectangular block placed over the electrodes. These blocks had the same contact impedance as the double-layer capacitors in our equivalent circuit model. The cell was modeled as a sphere that is vertically centered in the microfluidic channel. The electrical properties of the cell were set the same as the values used in our circuit model, namely conductivity (σ_i) = 0.5 S/m and permittivity (ε_i) = 60. A 100 nm-thick cell membrane was approximated by the contact impedance boundary condition assuming the membrane conductivity and the membrane relative permittivity to be 10^{-8} S/m and 11, respectively. The medium (the material of the rectangular block representing the microfluidic channel) was modeled as a dilute solution of PBS (σ_m = 1.4 S/m; ε_m = 80).

We performed a parametric study in which the sphere advanced in the microfluidic channel occupying a set of predetermined locations. A 100 mV AC signal at 500 kHz was applied to the common electrodes, while the sensing electrodes were grounded. An insulating boundary condition is applied to all other boundaries. To calculate the current flow from an individual electrode, we first calculate the current density on the two section planes symmetrically positioned at the gap midpoints on both sides of the electrode. We then integrate the current density over these cross-sectional planes and add them to calculate the total current flow of a single electrode. Finally, the currents from each electrode are added or subtracted based on its type (e.g., common, positive or negative) to obtain the final sensor output current.

4.5 Experimental validation of the model

To validate our equivalent circuit model, we compared model results with the experimentally obtained sensor signals supported by the high-speed microscopy images taken as cells flow over the coding electrodes. Figure 4.6 shows a recorded sensor waveform and a simulated waveform from our equivalent circuit model for the sensor encoding the signal 1010110. In addition, a series of images indicates the position of the cell in the microfluidic channel corresponding to different time-points in the code waveform (Figure 4.6(a)). Our model results match closely with the recorded sensor signals and successfully capture the deviations from an ideal pulse waveform (Figures 4.6(c), 4.6(d)). For example, the circuit model predicts that the peak signal amplitude is lower for the same-polarity bit sequences (e.g., 11 or 00) than the opposite-polarity bit sequences (e.g., 10 or 01), a result that is also supported by the recorded waveform when signal levels at time-points 6 & 7 are compared to time-points 2 & 4. In addition, our model successfully predicts the ripples observed in the signal even if the cell is passing through the same polarity bits. Based on our model, these are circuit-level effects and occur due to cross-coupling between electrodes in the sensor network. On the other hand, discrepancies between the model result and the experimental signal are mainly because our model does not consider perturbation in the electric field due to the cell. In fact, the comparison between conformal mapping results using unperturbed and perturbed field lines, simulated using finite element analysis (FEA), show that cell volume fraction is overestimated in the unperturbed field distribution (Figure 4.7). This inevitably leads to inaccuracy in the calculation of resistor and capacitor values in the equivalent circuit model.

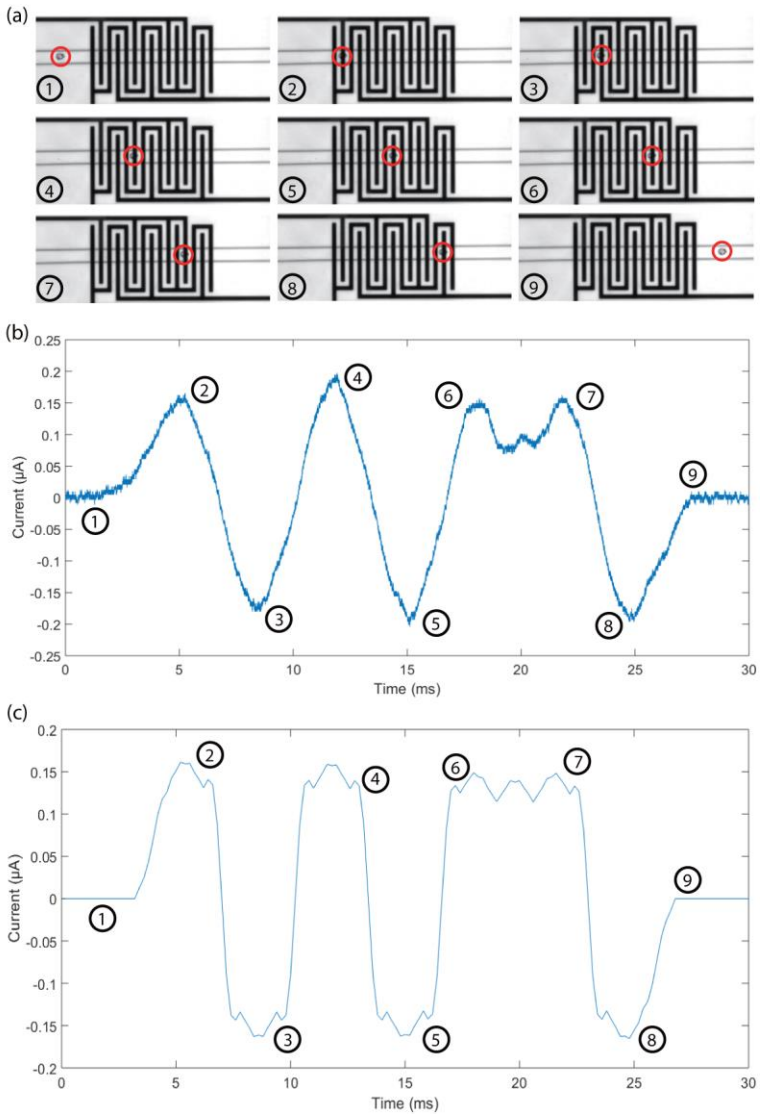

Figure 4.6 – Validation of our model results using experimental measurements. (a) Series of high-speed microscopy images indicating the position of the cell in the microfluidic channel corresponding to different time-points in the code waveforms. (b) A recorded sensor waveform corresponding to code 1010110. (c) Corresponding simulated waveform obtained using our equivalent circuit model.

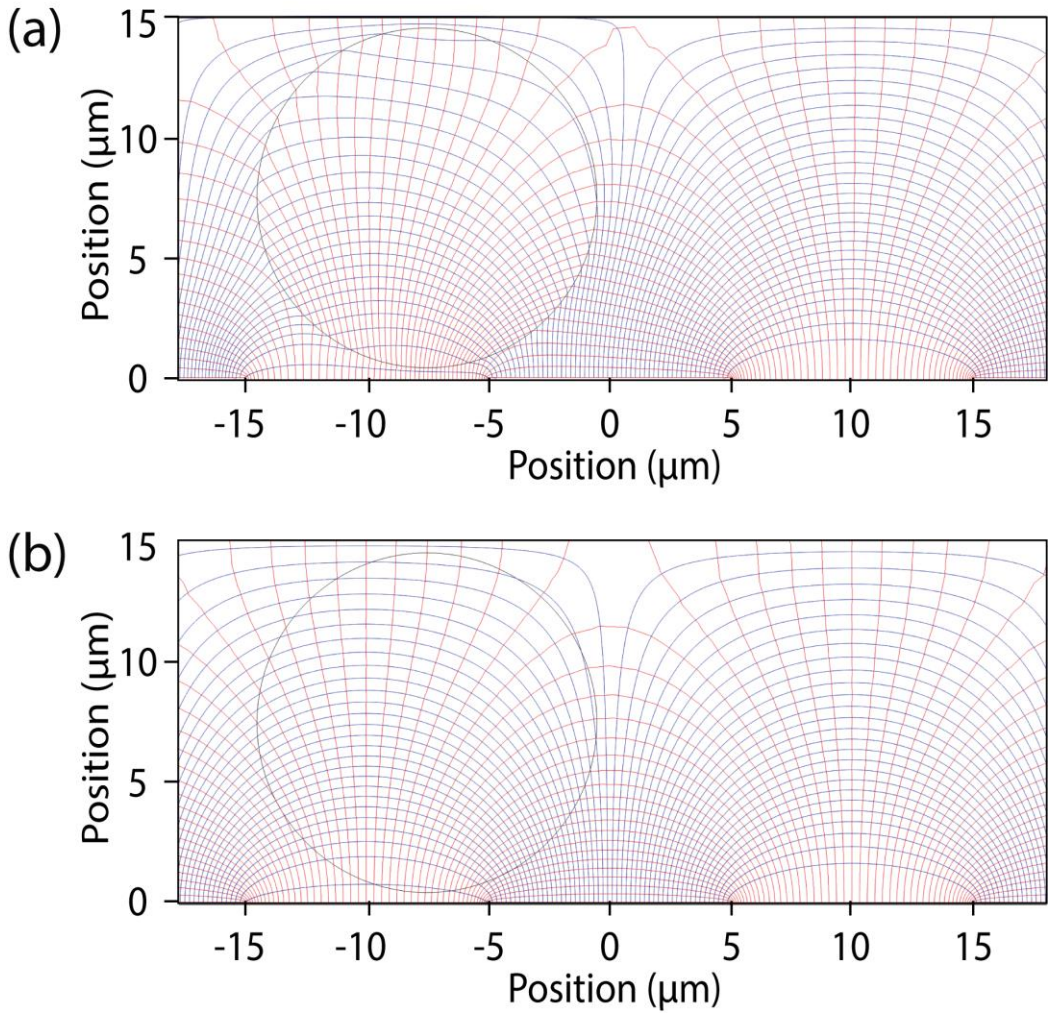

Figure 4.7 – Comparison of electric field line distribution within the microfluidic channel simulated using finite element analysis (a) with and (b) without the electric field perturbation due to the presence of the cell. The cell has a 7 µm radius, is vertically centered in a 15 µm-high microfluidic channel.

We applied our model to simulate sensors designed based on different coding sequences. Figure 4.8 shows recorded sensor signals, equivalent circuit model results and FEA simulation results for each of the four code-multiplexed sensors in our device presented here. For each sensor in this plot, we arbitrarily selected a cell from a recorded data stream, extracted the signal waveform corresponding to that cell, measured its size from simultaneously captured high-speed microscopy image, and then simulated the sensor

output using our equivalent circuit model and FEA. From optical measurements, the radii of the cells detected by sensors 1 - 4 in Figure 4.8 were determined to be 6.17 μm, 6.2 μm, 6.42 μm, and 6.23 μm, respectively. Simulation results closely match with experimental results and successfully predict the output waveform for all of the sensors. We think that the small differences (<15%) in the peak amplitudes between the model, FEA and experimental results can be due to several factors: (1) the exact vertical position of the cell in the microfluidic channel was not known in our simulations [148,149], (2) the measurement of the cell size from high-speed microscopy images could only be done with limited accuracy, (3) our equivalent circuit simulations did not include the field perturbation due to cell as well as the conductivity and the capacitance of the cell membrane [143], and , (4) the electrical properties of deposited gold films were not known and the FEA simulation did not include the additional resistance due to electrode traces.

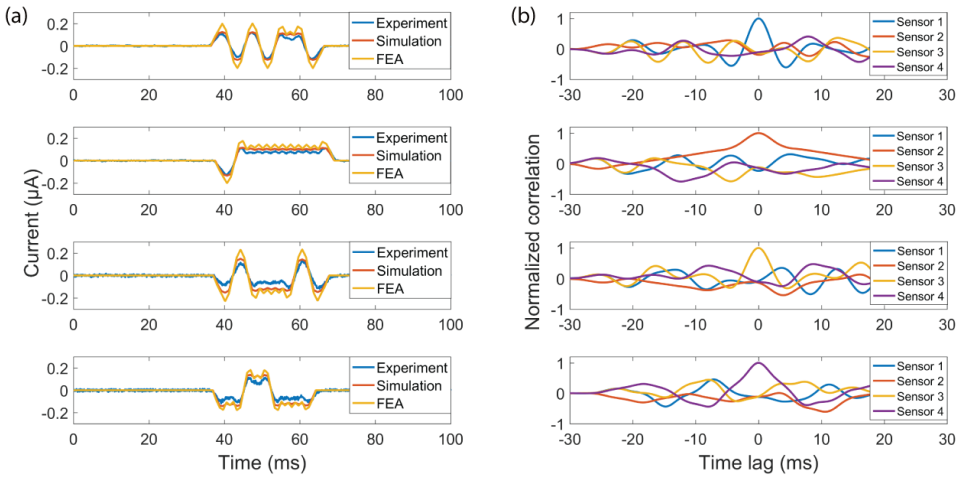

Figure 4.8 – Comparison of experimental signals with simulation results. (a) Recoded sensor signals (blue), equivalent circuit model results (red) and FEA simulation results (yellow) for arbitrary signals from each of the four code-multiplexed sensors in our device. (b) Cross-correlation coefficients between the experimental signal from each sensor and the simulated waveforms generated by our equivalent circuit model for all of the sensors as a function of time delay.

In Microfluidic CODES, we previously decoded the sensor signals by correlating the signal with a template library, which was constructed using experimentally obtained non-overlapping code signals from each sensor. By identifying the specific template producing the maximum cross-correlation peak among all the candidates, we obtained the spatiotemporal information on the particle. Here, we calculated cross-correlation coefficients between the experimental signal from each sensor and the simulated waveforms generated by our equivalent circuit model for different time delays (Figure 3.8, right). For each sensor, cross-correlation of the experimental signal only with the matching simulated waveform at zero time delay produces a peak correlation value, which can also be considered as the autocorrelation peak. Therefore, these results demonstrate the potential utility of using our circuit model to generate simulated waveforms in constructing a template library or a matched filter bank that can be used to decode the experimental signals.

Unlike a conventional CDMA telecommunication network, where the information is encoded with electronically synthesized digital codes of fixed pulse width, the pulse width of digital sensor signals in our microfluidic system depends on the particle flow speed. Therefore, different particle speeds due to the parabolic flow profile in a pressure-driven microfluidic system cause pulse broadening/narrowing in the digital sensor signals. To analyze this effect on the decoding of sensor signals, we first calculated the aperiodic correlation of an experimentally recorded sensor signal with the corresponding model-simulated code waveforms of different durations (Figure 4.9(a)). Our results demonstrate that the peak correlation amplitude corresponds to the cross-correlation of the experimental signal with the simulated waveform of matching pulse-width at zero-time lag. These results

demonstrate that it is possible to estimate the duration or the pulse width of a recorded sensor signal by correlating it with a library of template waveforms with varying durations.

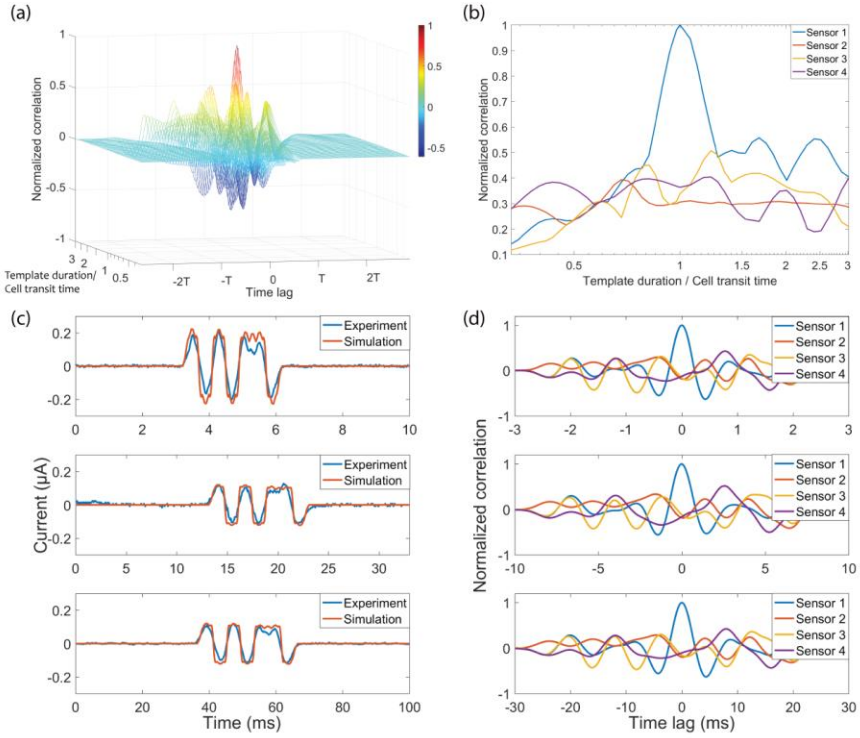

Figure 4.9 – Analysis of the effect of cell speed variation on the distinguishability of sensor signals. (a) Cross-correlation of a recorded sensor signal (1010110) with model-generated code templates of durations ranging from 1/3 to 3 times of the signal duration. (b) Peak amplitude from the cross-correlation of a recorded sensor signal (1010110) with model-generated code templates corresponding to all four sensors in the network as a function of template duration. (c) Comparison between sensor signals (blue) recorded under different flow speeds and the model-generated template waveforms (red) that produced the highest correlation value. (d) Cross-correlation of the sensor signals with the model-generated template waveforms in (c) and with templates of matching duration corresponding to other sensors in the network.

Next, we calculated the cross-correlation of the recorded sensor signal with simulated waveforms of varying durations corresponding to all of the sensors in the network. Comparison of the peak cross-correlation amplitudes indicates that the sensor signal can be differentiated from other sensors in the network without prior knowledge of the particle speed (Figure 4.9(b)). We also analyzed sensor signals acquired under different

flow speeds, and estimated the cell transit time by calculating the cross-correlation with simulated waveforms of various durations. The close match between the timing of simulated waveform and the experimental signal demonstrates that sensor signals from particles with different flow speeds can be accurately resolved (Figures 4.9(c), 4.9(d)).

As in any resistive pulse sensor employing coplanar electrodes, particle size, and its proximity to the surface electrodes are two important factors that affect the amplitude of sensor signals in our system. Therefore, the accurate modeling of the sensor response requires these two parameters to be taken into consideration. As previously described, our graphic conformal mapping method provides a simple and fast approach to simulate particles with different sizes at arbitrary vertical positions within the microfluidic channel. To demonstrate this capability, we first simulated sensor code signals for a set of cells of varying radii (1 - 7 μm) flowing vertically centered (i.e., 7.5 μm above the electrodes) in a 15 μm-high microfluidic channel (Figure 4.10). Our simulations show that signal pattern (i.e., code) is preserved for different cell sizes. As expected, the peak signal amplitude increases with cell size due to the larger cell leading to a larger impedance change in the channel [150].

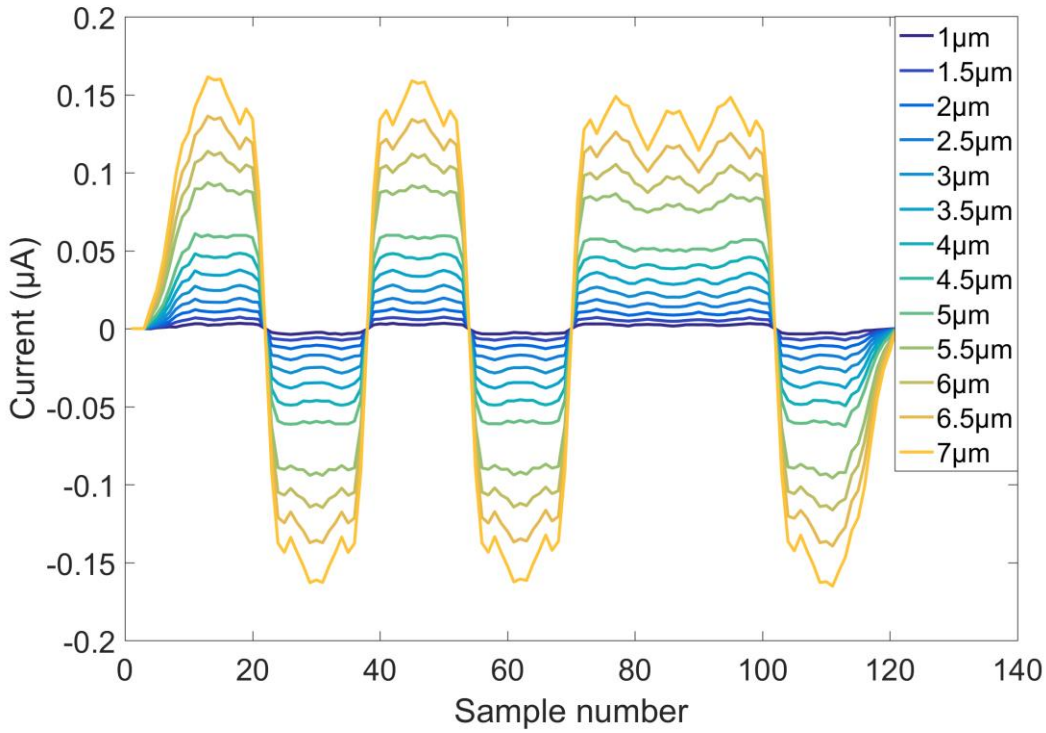

Figure 4.10 – Analysis of the effects of particle size on the signal amplitude. (a) Code waveforms simulated using our equivalent circuit model for cells with different sizes (radii ranging from 1 μm to 7 μm) flowing vertically centered (i.e., 7.5 μm above the electrodes) in a 15 μm-high microfluidic channel.

Next, we analyzed the effect of cell-electrode proximity by simulating the sensor response for the same 2.5 μm-radius cell at vertical positions corresponding to 1/4, 1/2, and 3/4 of the 15 μm-high microfluidic channel (Figure 4.11). As expected, the signal amplitude is higher for a cell closer to the electrodes. This is because a cell closer to the electrode occupies a volume of higher electrical field density compared to a cell further away, and therefore effectively leads to a higher volume occupation fraction and larger modulation in the current flow. In addition, the simulated waveform for the cell close to the electrode shows significant ripples in the code waveform - a phenomenon not observed in recorded sensor signals. This discrepancy is due to the lack of cell-induced electric field perturbation in our model. Neglecting electric field perturbation leads to dramatic

differences in the calculated cell volume fraction in the conformal mapping process, particularly when cells are positioned at locations of dense field lines (e.g., closer to electrodes) (Figure 4.12).

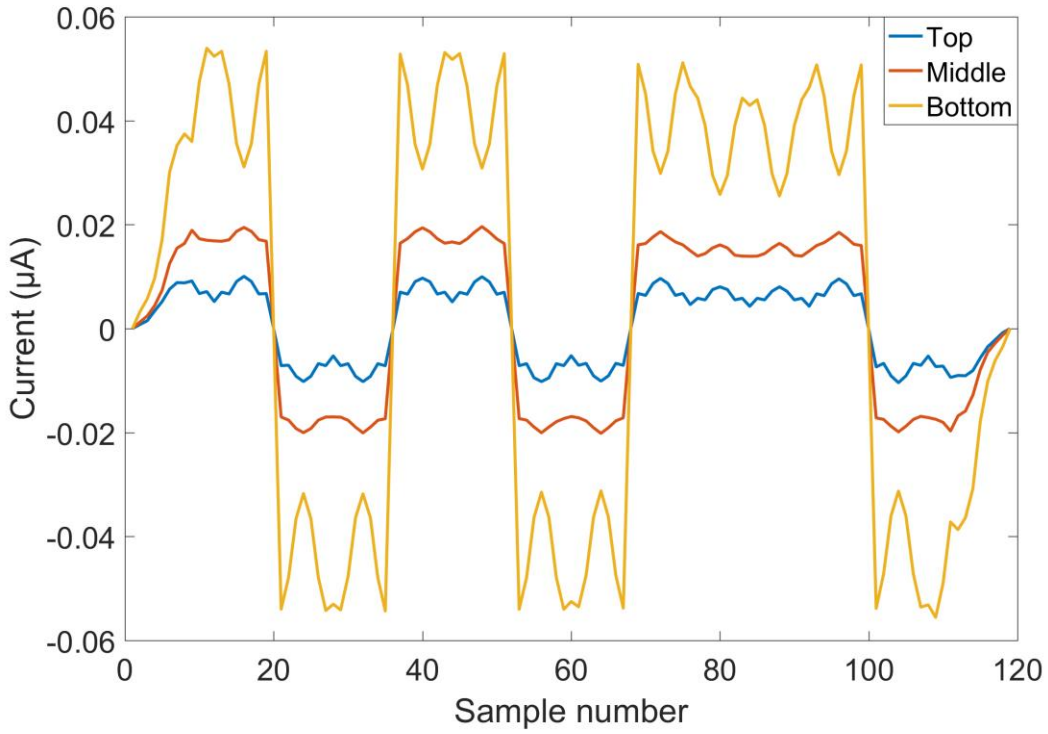

Figure 4.11 – Analysis of the effects of particle proximity to the surface electrodes on the signal amplitude. Code waveforms simulated using our equivalent circuit model for a 2.5 μm-radius cell at vertical positions corresponding to 1/4, 1/2, and 3/4 of the 15 μm-high microfluidic channel.

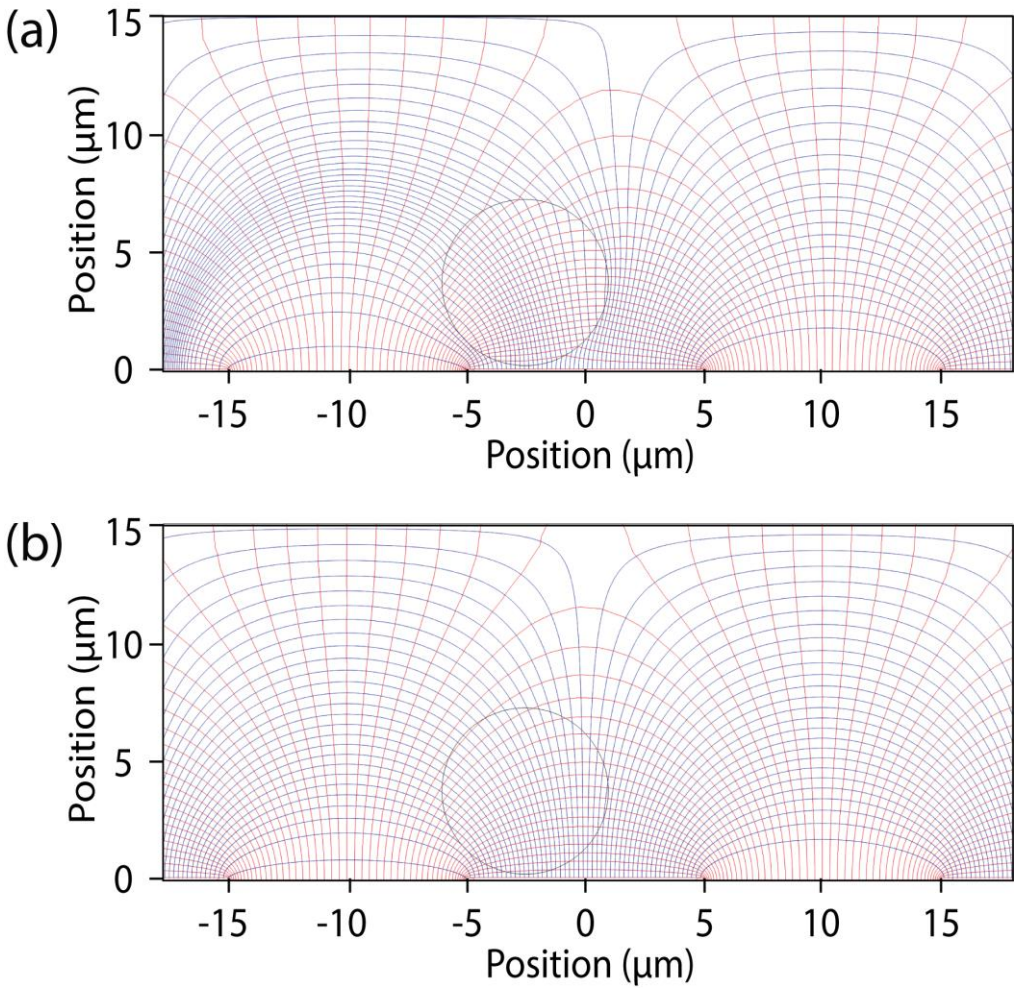

Figure 4.12 – Comparison of electric field line distribution within the microfluidic channel simulated using finite element analysis (a) with and (b) without the electric field perturbation due to the presence of the cell. The cell has a 2.5 µm radius, is positioned at a vertical position corresponding to ¼ of the 15 µm-high microfluidic channel.

Our circuit model can also be used to predict sensor signal interference patterns due to coincident cells in the sensing volume. To demonstrate this capability, we analyzed matching high-speed microscopy images and identified a signal corresponding to four interfering sensors due to four coincident cells simultaneously interacting with the electrodes (Figure 4.13). We first measured the sizes, speeds, and the relative timing of coincident cells from the optical data. (The sizes of the cells detected by sensors 1 to 4 are

7.40 µm, 5.79 µm, 5.09 µm, and 6.01 µm, respectively). We then generated an equivalent circuit model that includes all the cells simultaneously occupying the sensor network. As explained before, the circuit configuration was dynamically updated to simulate the varying cells' positions due to fluid flow and the output waveform was generated using MATLAB Simulink. A comparison of model results with the experimental data shows that our model can successfully predict the interference pattern (Figure 4.13, right). Mismatches at certain points between the simulated waveform and the experimental signals can be explained by several factors. First, in our circuit model, the distance between any two coincident cells can only increment discretely, and this introduces a quantization error in the time delay between interfering signals. Second, the inaccuracies in predicting individual sensor signals as outlined above also affect the simulation of interference between those signals.

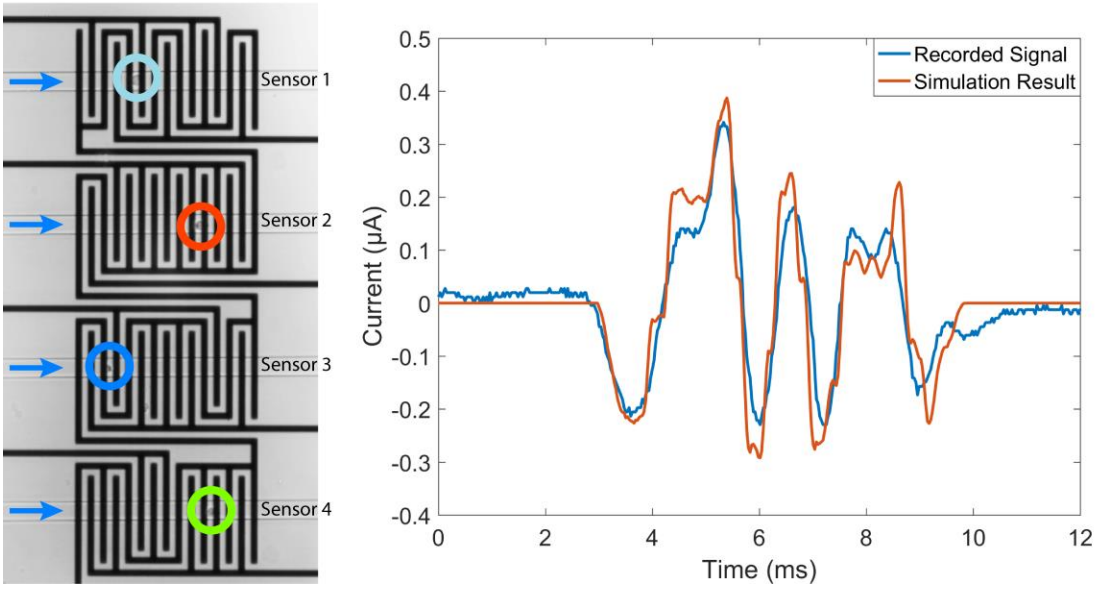

Figure 4.13 – Experimental analysis and simulation of a case, where four sensor signals interfered as a result of four cells simultaneously interacting with the electrodes. (a) Simultaneously recorded high-speed microscope image showing four overlapping cells. (b) Recorded sensor signal (blue) and our simulation results from an equivalent circuit that represents four coincident cells (red).

One of the unique strengths of the Microfluidic CODES is its ability to spatiotemporally resolve coincident particles in the sensing volume. To decode interfering signals, we use a modified successive interference cancellation approach that is used in multi-user detection in CDMA communication networks [116,151,152]. Here, we demonstrate this process in decoding the signal of Figure 3.13 with a template library constructed using the waveforms generated using our equivalent circuit model (Figure 4.14). Briefly, in this process, the recorded signal is correlated with a library of pre-constructed templates that correspond to code waveforms from all the sensors in the network. Once the dominant correlation peak is identified, it is regarded as the autocorrelation peak, and its timing and the peak amplitude are used to estimate the individual sensor signal from the matching template waveform. Next, the estimated sensor signal is subtracted from the original recorded signal, and the process is iterated until the residual signal cannot be associated with any of the template waveforms to reveal the remaining sensor signals. The fact that sensor signals from smaller cells can successfully be resolved despite being shadowed by signals from larger cells demonstrates the strength of our successive interference cancellation approach.

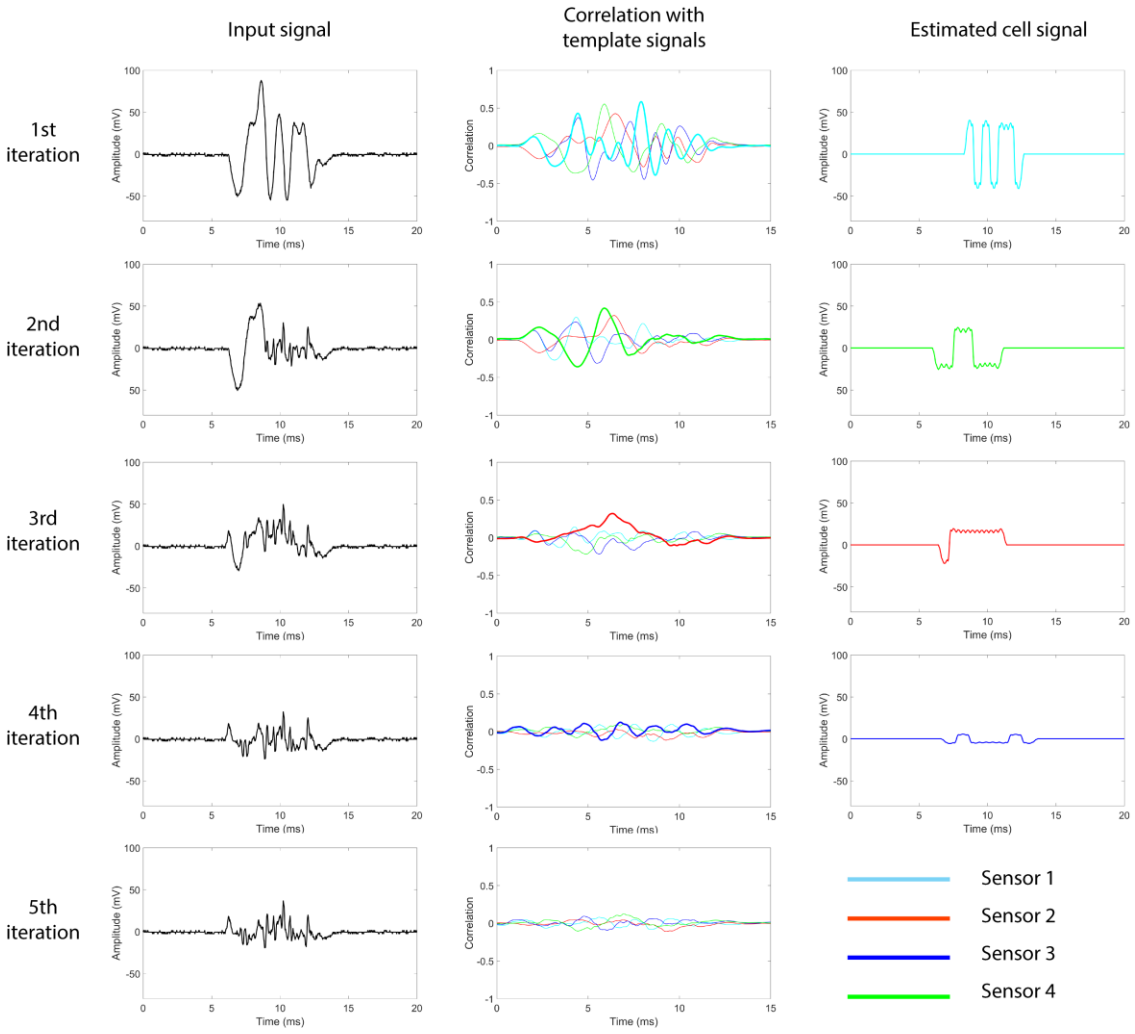

Figure 4.14 – Step-by-step demonstration of the successive interference cancellation algorithm used to resolve interfering sensor signals due to four coincident cells with different sizes and flow speeds

Finally, to demonstrate the applicability of our circuit model regardless of the cell size, speed and coincidence, we arbitrarily selected a time window, in which 13 cells flow over our sensor network. Using the optical data, we determined the size, speed, timing, and the sensor they interacted with were determined from optical data (Table 4.3). Using these parameters, we simulated the sensor response using our model, and compared it with the recorded sensor signal (Figure 4.15). The close match between the estimated signal and the

experimental data suggests that our model can robustly and accurately predict the sensor response to different cells with differing properties.

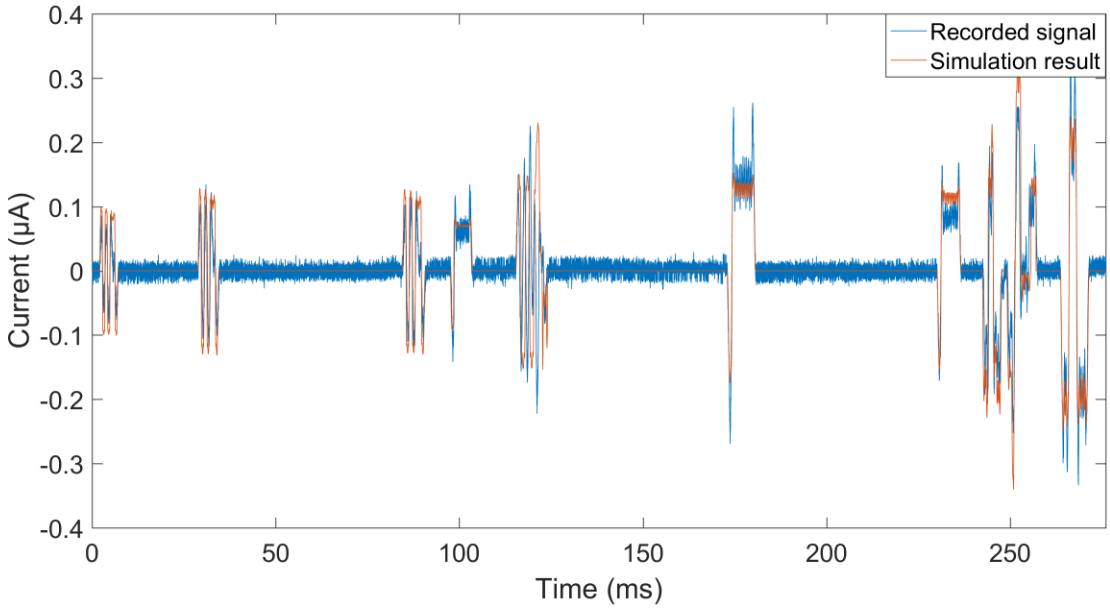

Figure 4.15 – Comparison of recorded sensor signals with equivalent circuit model generated waveforms corresponding to 13 cells of varying sizes and speeds in an arbitrarily selected time window.

Table 4.3 – Information of cells in the selected time window

Flow order	Cell radius (μm)	Time delay (ms)	Cell speed (mm/s)	Sensor number
1	5.64	0	54.7	1
2	6.34	27	48.3	1
3	6.31	83	48.3	1
4	5.31	96	50.9	2
5	6.80	114	50.9	1
6	5.70	117	67.4	1
7	7.02	171	41.4	2
8	6.68	228	48.3	2
9	7.23	241	61.7	4
10	3.20	242	67.4	4
11	6.95	247	50.9	4
12	7.20	248	43.3	2
13	7.91	262	39.7	4

4.6 Conclusions

Microfluidic CODES employs a network of micromachined coplanar electrodes such that particles passing over these electrodes produce distinguishable code sequences. In this chapter, we introduced an equivalent circuit model for a network of code-multiplexed resistive pulse sensors by utilizing the Foster-Schwan model and conformal mapping, to model dynamic cell-electrode interaction in a non-uniform electric field. Our results closely matched with both experimental measurements using cell lines and finite element analysis. The modeling framework presented here will enable the design of code-division multiplexed resistive pulse sensors optimized to produce desired waveform patterns to ensure reliable and efficient decoding.

CHAPTER 5. THE SCALING OF MICROFLUIDIC CODES [153]

The utility of our distributed sensing approach to creating integrated lab-on-a-chip devices for complex assays increases with the number of on-chip nodes that can simultaneously be monitored. Therefore, in this chapter, we aim to investigate the scaling of code-multiplexed electrode networks to accommodate more Coulter sensors by theoretically and experimentally evaluating the challenges associated with such network expansion. Specifically, we model the electrical interface to the microfluidic chip as a telecommunications channel and utilize the coding theory not only to optimize the sensor waveforms but also to analyze the decoding performance by analytically calculating the error rate as a function of the network size and the sample properties. We also investigate the effects of the scaled network layout on the system sensitivity and optimize the electrode configuration accordingly. Finally, we develop an algorithm to process the scaled sensor network data and experimentally characterize the device performance using cell suspensions. Taken together, our work represents a foundation for the development of large-scale code-multiplexed electrical sensor networks to be used in distributed Coulter detection of particles manipulated in microfluidic devices in order to transform extensive sample manipulation capabilities of microfluidics into integrated lab-on-a-chip systems for quantitative sample analysis.

5.1 Device design, fabrication, and operation

The design, fabrication, and operation of the large-scaled sensor Microfluidic CODES device are similar to those of simple Microfluidic CODES devices introduced in Chapter 3 (Section 3.2, 3.3, and 3.4). A photo of the 10-sensor Microfluidic CODES device

as a representative is shown in Figure 5.1. The codes used in the sensor network are listed in Table 5.1, and the individual signals from each of the sensors in the network are represented in Figure 5.2.

Table 5.1 – The codes used in the 10-sensor multiplexed sensor network

Sensor #	Code
Sensor 1	10101110110001111100110100100000
Sensor 2	10110101000111011111001001100000
Sensor 3	00011011110110100011111101000000
Sensor 4	11000011001000111001101101101010
Sensor 5	01101101111001000101011001001010
Sensor 6	00000100111011101011101000110110
Sensor 7	01110010110100001101001100111100
Sensor 8	01001100101110011101100111010000
Sensor 9	00100101101100110011010110101100
Sensor 10	10010100010000000111110111111010

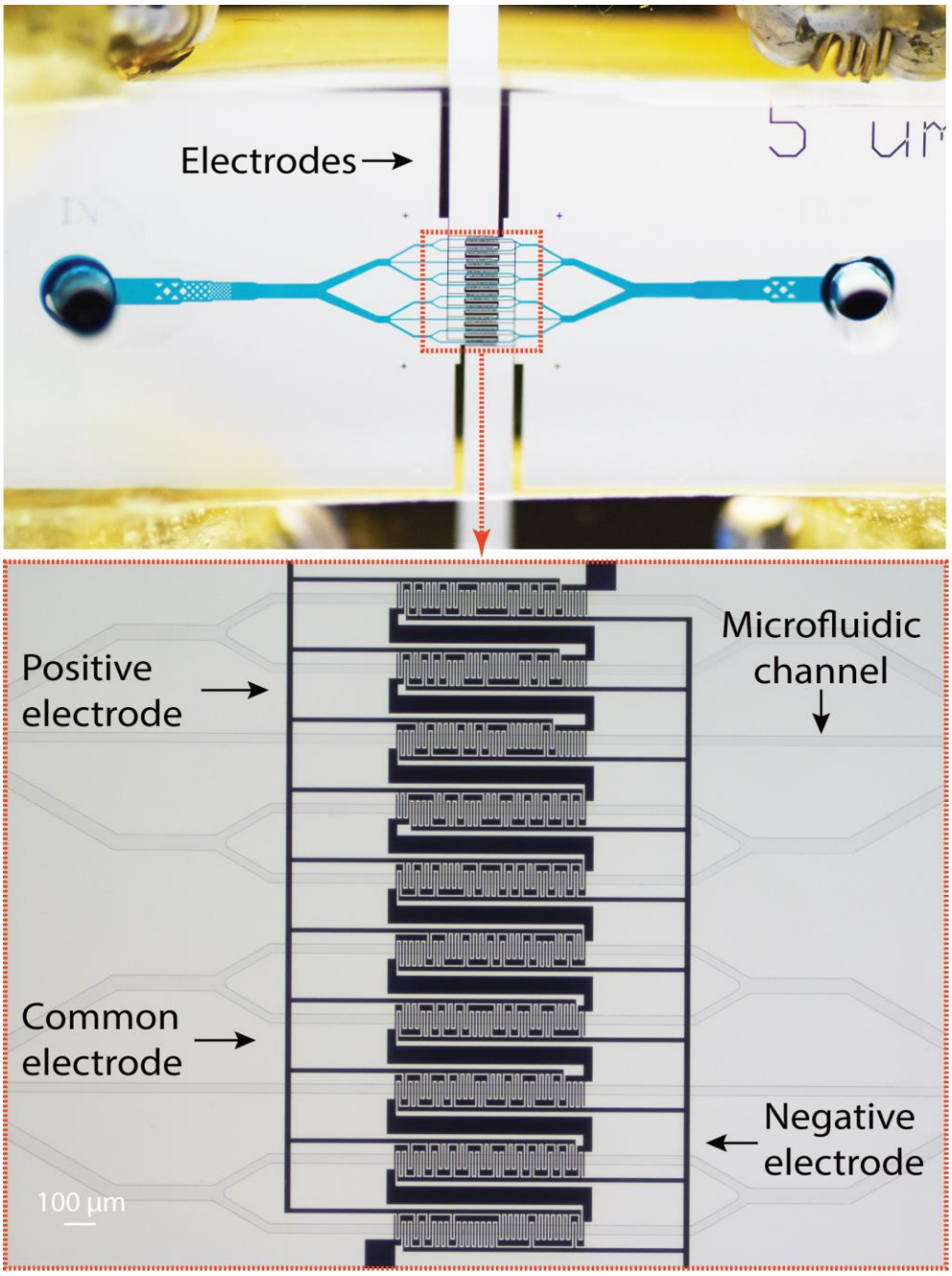

Figure 5.1 – 10-sensor Microfluidic CODES device. On top shows a photo of the microfluidic device integrated with a network of 10 code-multiplexed sensors. The microfluidic chip is fabricated using soft lithography on a glass slide with micropatterned Au electrodes. The microfluidic channel layer is filled with a blue dye for imaging purposes. At bottom shows the microscope image of the surface electrode network forming 10 Coulter sensors, each encoding a different 31-bit Gold sequence. The image also demonstrates the alignment of the glass substrate patterned with coded electrodes with the PDMS microfluidic channel layer.

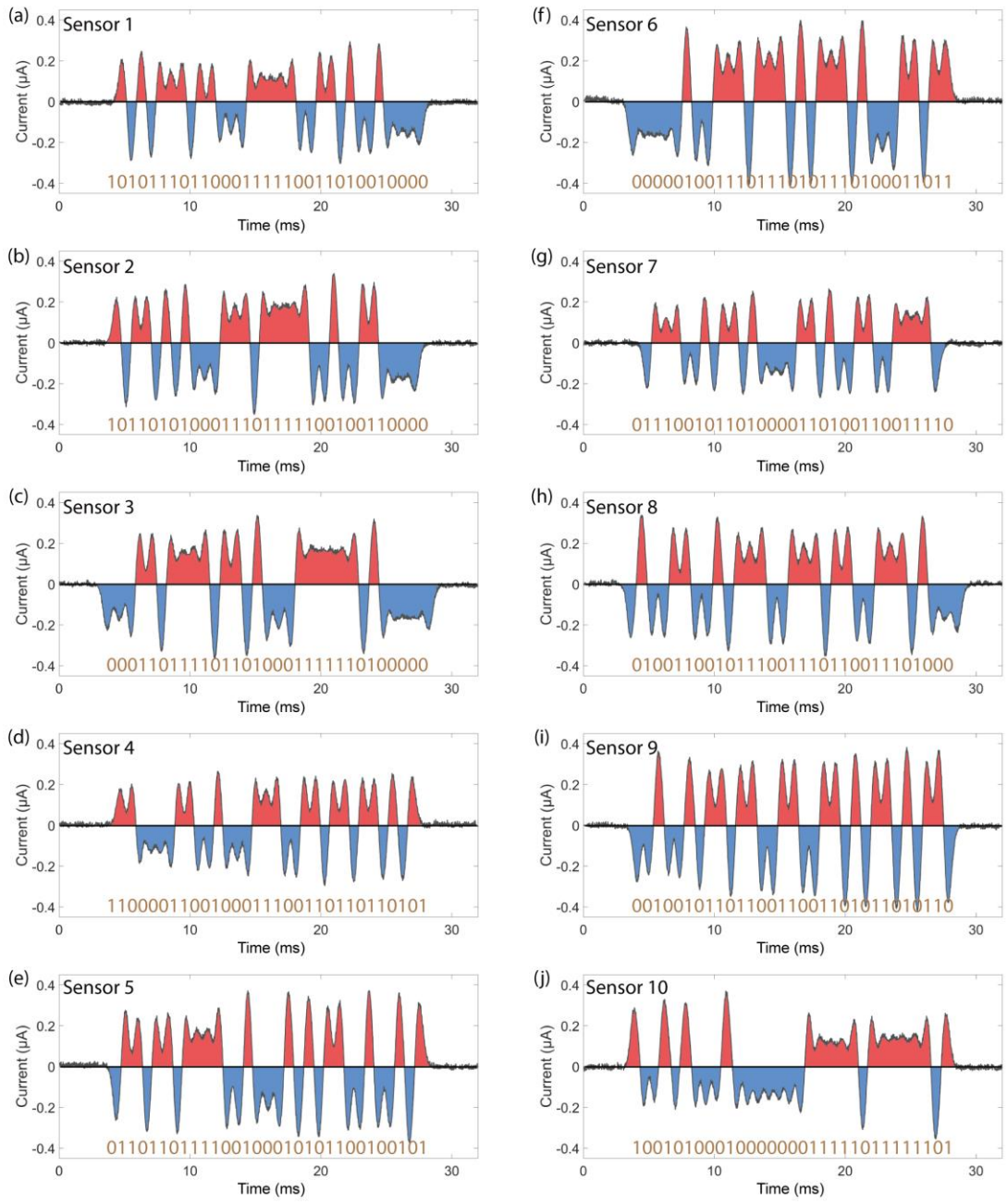

Figure 5.2 – Representative individual sensor signals recorded from each of the 10 sensors in the network. In each signal, positive values are interpreted as "1" while negative values represent "0". For each sensor, the output signal closely follows the specific bit sequence of the 31-bit Gold sequence encoded by the sensor. Corresponding digital code sequences for the signals shown in the figure are: (a) 1010111011000111110011010010000, (b) 1011010100011101111100100110000, (c) 0001101111011010001111110100000, (d) 1100001100100011100110110110101, (e) 0110110111100100010101100100101, (f) 0000010011101110101110100011011, (g) 0111001011010000110100110011110, (h) 0100110010111001110110011101000, (i) 0010010110110011001101011010110, (j) 1001010001000000011111011111101.

5.2 Sensor demultiplexing

The orthogonal signal waveforms generated by individual sensors in the network can be distinguished from each other with high SNR through a matched filter bank (Figure 5.3). For the decoding process, we first construct a set of code templates based on the averages of experimentally obtained sensor signals. Using these templates, we generate code waveforms broadened or compressed to account for different flow speeds of the particles. A matched filter bank is then constructed in MATLAB based on the whole template set and applied on the recorded signal.

When multiple cells simultaneously interact with the electrode network, individual sensor signals from those coincident cells interfere at the output signal. Interfering signals have random delays (due to asynchronous arrival of particles), and can have different amplitudes (due to different particle sizes) and durations (due to different particle flow speeds). In addition, the interference can be generated from particles interacting with different sensors (Figure 5.4(a)) or with the same sensor (Figure 5.4(b)). We can successfully demultiplex interfering sensor signals as we rely on the fact that pseudorandom noise (PRN) sequences (i.e., Gold sequences) ensure a sharp autocorrelation peak only when the template and the signal are completely aligned in time and sequence (Figure 5.3). Once an autocorrelation peak is identified, we subtract an estimate of the dominant sensor waveform from the signal to eliminate the crosstalk in detecting sensor signals with less power from smaller particles [116,126].

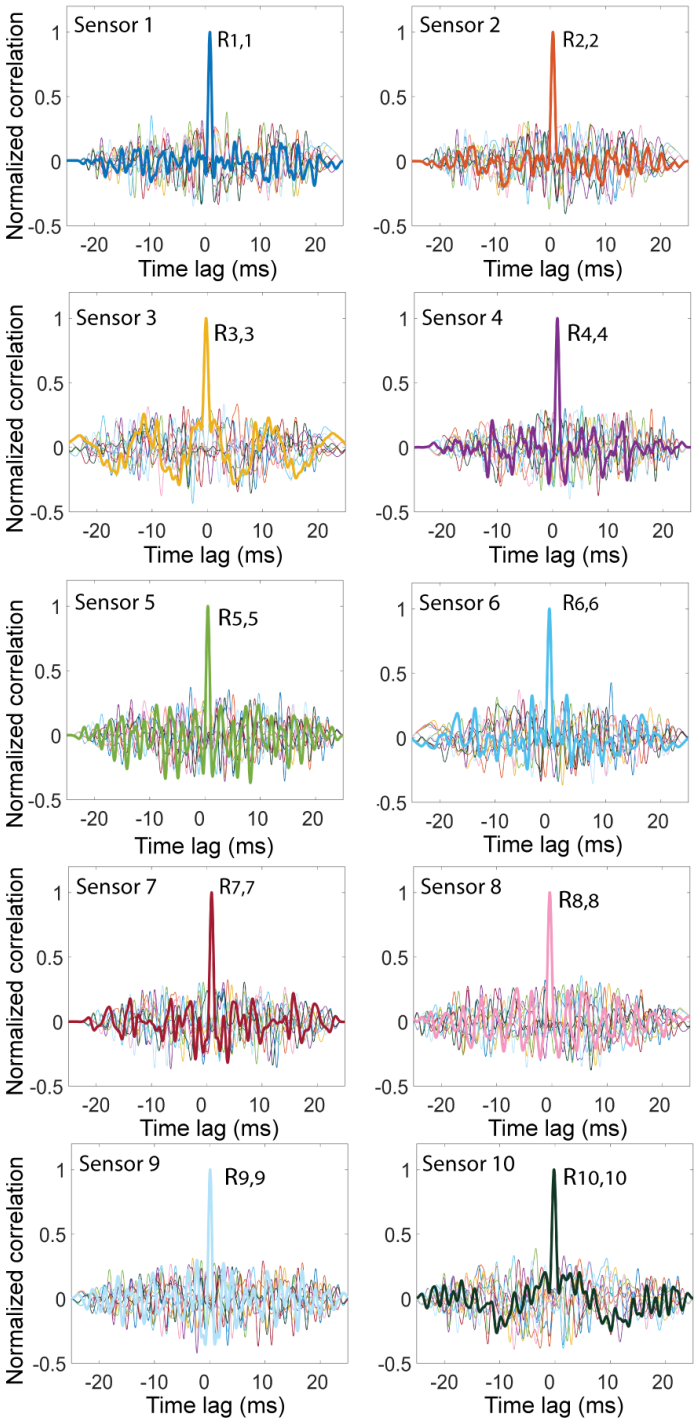

Figure 5.3 – Demultiplexing of coded sensor signals through correlation analysis. Sensor signals are correlated with a template library consisting of representative signals from all sensors in the network. Figures show results for 10 different sensor signals from their correlation with the template library for different time delays. A dominant autocorrelation peak at zero-time delay can be easily identified in each case, because the code sequences are specifically designed to be orthogonal to each other.

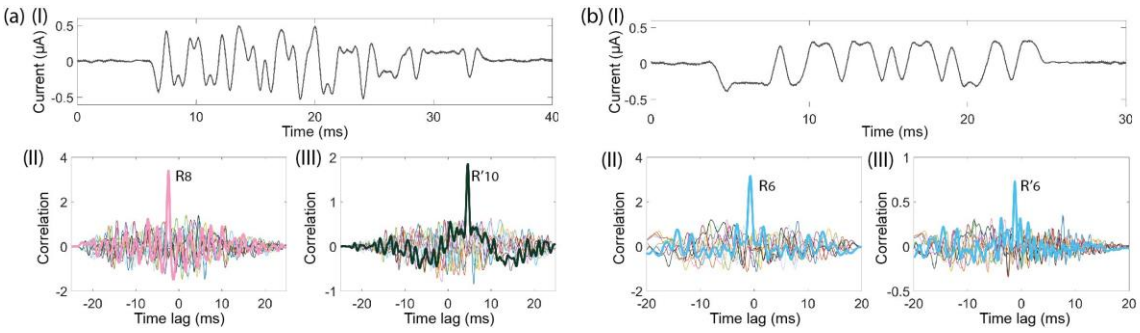

Figure 5.4 – Demultiplexing of coded sensor signals through correlation analysis (coincident case). Coincident particles lead to interference of signals from (a) different sensors or (b) the same sensor. Correlating the interference signal (I) with the template library produces a dominant peak that corresponds to the largest particle (II). The estimated signal for the largest cell is subtracted from the original signal, and the residual signal is correlated with the template library again to recover the sensor signal due to the next largest particle (III).

Besides enabling the construction of a larger orthogonal code-set to expand the sensor network, longer codes yield higher sensitivity in identifying individual sensor signals in the presence of interference from others in the network. This is because, a matched decoder selectively amplifies the target signal (i.e., autocorrelation) while suppressing the other sensor signals as they appear as random noise to the decoder. This selective amplification, called CDMA processing gain, provides higher gain with longer code sequences. A comparison of decoder output from our device based on 31-bit Gold sequences with another system based on 7-bit Gold sequences, demonstrates the higher sensitivity (Figure 5.5). Note that the signals obtained from relatively small cells are specifically chosen to demonstrate the effect of processing gain in suppressing the electronic noise.

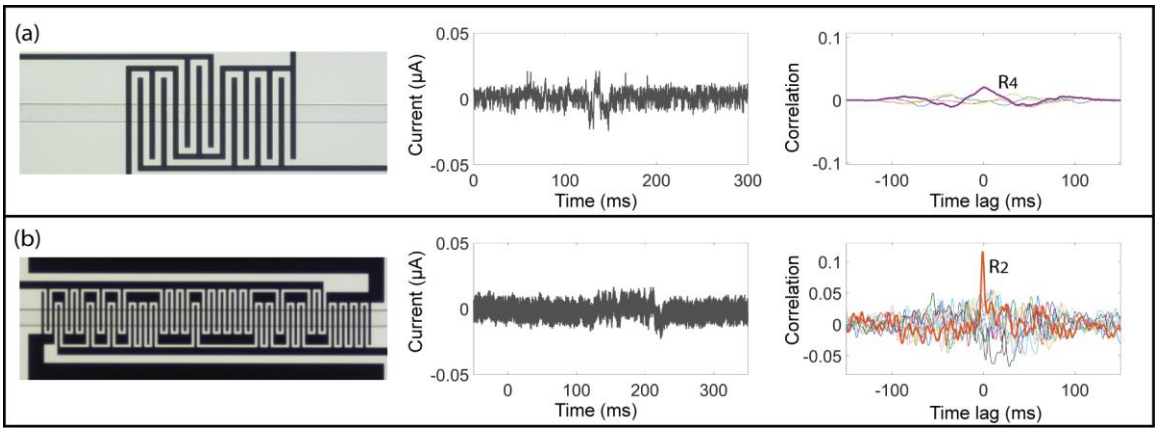

Figure 5.5 – Comparison of (a) 7-bit and (b) 31-bit sensor signals due to a small particle. For each case, sensor layout (left), time waveform (middle) and the correlation results (right) are shown. The correlation results show that a longer sequence can be distinguished with higher sensitivity due to higher processing gain.

5.3 Error Rate Estimation

Interference from one sensor appears as noise in the output of a decoder designed to receive signals from another sensor. Therefore, interference due to coincident particles leads to lower SNR and eventually leads to errors in decoding of the sensor network data. To theoretically calculate the error rate due to multiplexing, we model the sensor interference by first assuming individual sensor signals (s_k) as sequences of random bipolar pulses (c_k) mixed with the excitation signal at frequency f_c.

$$s_k(t) = \sqrt{2P_k}c_k(t)\cos(2\pi f_c t) \tag{5.1}$$

$$c_k(t) = \sum_{i=0}^{N-1} c_{k,i}\Pi\left(\frac{t - iT_c}{T_c}\right), \quad c_{k,i} \in \{-1,1\} \tag{5.2}$$

where P_k is the signal power from the k-th sensor, N is the number of bits in the digital code and $\prod(t)$ is the rectangular function that equals 1 for $0 < t < 1$ and 0 otherwise. For

k coincident cells (Figure 5.6), the output I of the correlation decoder designed to receive the signal from the sensor with code c_0 is given by

$$I = \int_0^T c_0(t)\cos(2\pi f_c t)\left(\sum_{k=0}^{K-1}\sqrt{2P_k}c_k(t-\tau_k)\cos(2\pi f_c t)\right)\mathrm{d}t \tag{5.3}$$

I may be divided into two parts and expressed as

$$I = I_0 + I_k = \sqrt{\frac{P_0}{2}}T + \frac{1}{2}\int_0^T\left(\sum_{k=1}^{K-1}\sqrt{2P_k}c_k(t-\tau_k)c_0(t)\right)\mathrm{d}t \tag{5.4}$$

where I_0 is the desired contribution to the output from the "matched" sensor, I_k is the multiple access interference from all other sensors, and τ_k is the delay for the k-th sensor. Note that the delay τ_k is between the code waveforms while the AC signal from each sensor is in phase, unlike the carrier waves in the wireless communication channel. The noise is not included in the calculations as the decoder performance is clearly interference limited.

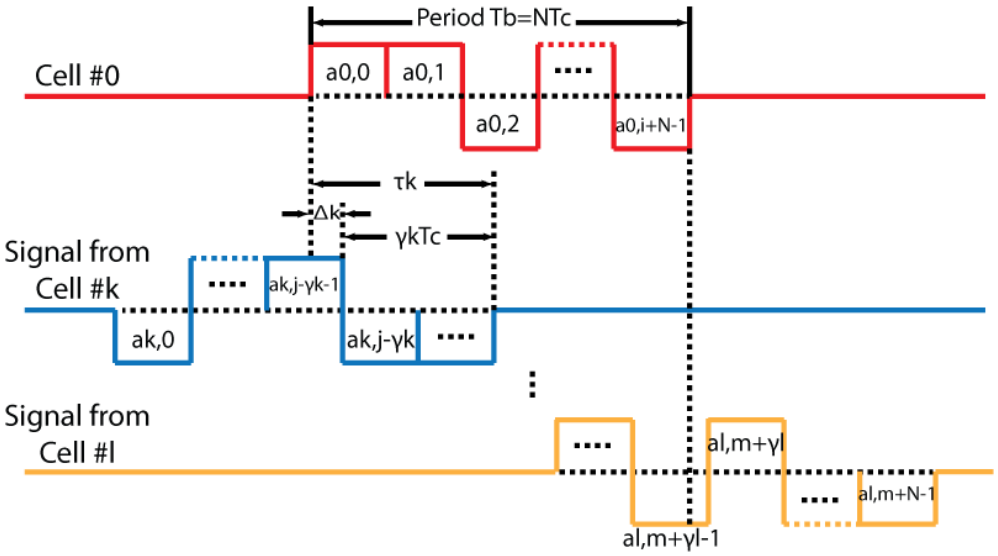

Figure 5.6 – Mathematical framework to model sensor signal interference. Sensor signals are assumed to be digital waveforms with random delays between interfering signals.

Modeling of the interference between code-multiplexed information sources and its effect on the bit error rate has been studied extensively in the context of wireless communications [154,155]. We model the interference of k particles in our device with the Improved Gaussian Approximation (IGA) [156,157] which is used to analyze multi-access interference among k transmitters. In IGA, we model the variance of the interference as a Gaussian random variable (Ψ) with a mean μ_Ψ and a variance σ_Ψ^2, which are calculated as

$$\mu_\Psi = \frac{TN}{3}(K-1)\mu_p \tag{5.5}$$

$$\sigma_\Psi^2 = (K-1)\frac{T^4}{4}\left[\left(\frac{7N^2+2N-2}{15}\right)\sigma_\mathrm{p}^2 + \left(\frac{1}{45}N^2 + \left(\frac{1}{9}K - \frac{4}{45}\right)N - \left(\frac{1}{9}K - \frac{4}{45}\right)\right)\mu_\mathrm{p}^2\right] \tag{5.6}$$

where μ_p and σ_p^2 are the mean and variance of the sensor signal power levels. We determine from our data on cell experiments (Figure 5.7) that $\sigma_p = 2.4\,\mu_p$. If we also assume that an error occurs when the interference random variable becomes larger than the desired signal, the error probability can be expressed as

$$P_{e0} = E\left[Q\left(\sqrt{\frac{P_0 T^2}{2\Psi}}\right)\right]$$

$$\approx \frac{2}{3}Q\left(\sqrt{\frac{P_0 T^2}{2\mu_\Psi}}\right) + \frac{1}{6}Q\left(\sqrt{\frac{P_0 T^2}{2\left(\mu_\Psi + \sqrt{3}\sigma_\Psi\right)}}\right) \tag{5.7}$$

$$+ \frac{1}{6}Q\left(\sqrt{\frac{P_0 T_b^2}{2\left(\mu_\Psi - \sqrt{3}\sigma_\Psi\right)}}\right)$$

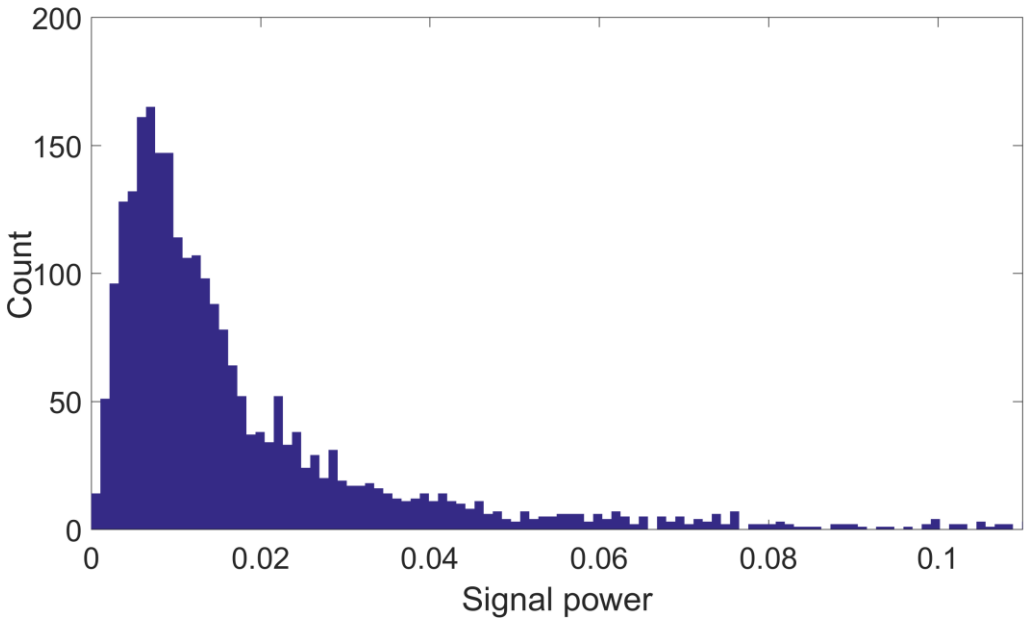

Figure 5.7 – The histogram showing the distribution of the sensor signal power from the sensor network interacting with a cell population.

Because the error rate (P_e) is a function of the power of the target signal, average error probability is calculated by averaging Equation 5.7 over all possible sensor signal power levels and is given by

$$P_e = \int_0^\infty P_{e0} f_{P_0}(P_0) \mathrm{d}P_0 \tag{5.8}$$

where f_{P_0} is the probability density function for sensor signal power levels. Using experimentally measured sensor power levels, we estimated the error rate as a function of expected coincident cells (Figure 5.8). In our system, the number of coincident cells can be modeled as a random variable (X) with Poisson distribution:

$$P(X = k) = \frac{e^{-\lambda}\lambda^k}{k!} \tag{5.9}$$

where λ is the expected number of coincident cells. The average error rate can be calculated as

$$E = \sum_{i=2}^{\infty} P_e(k) \frac{e^{-\lambda}\lambda^k}{k!} \tag{5.9}$$

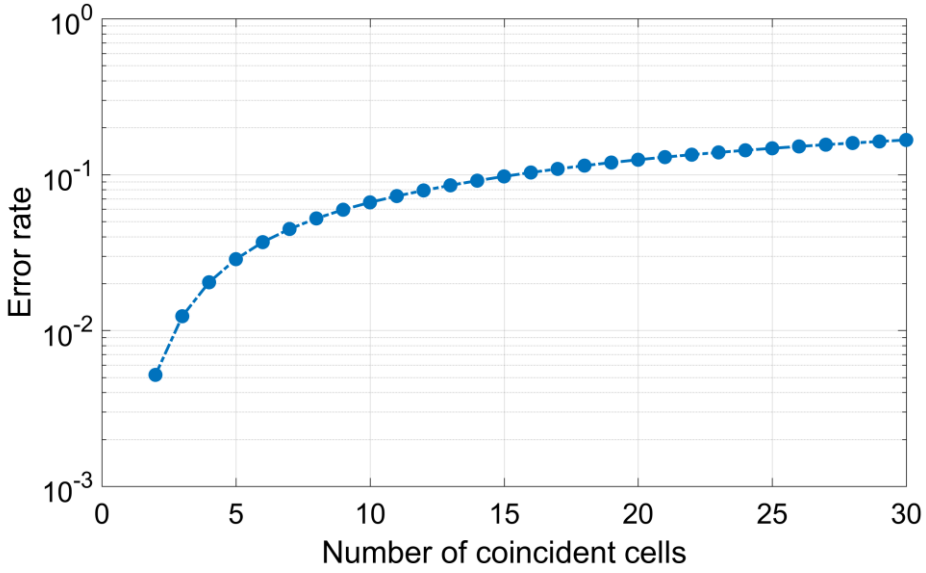

Figure 5.8 – Theoretical analysis of the effect of sensor signal interference due to coincident cells on the decoder performance. The estimated bit error rate in the decoder as a function of the number of coincident cells.

Because, the expected number of cells (λ) depends on the particle concentration (c) and the sensing volume (V) (i.e., $\lambda = c \times V$), the average error rate can also be calculated as functions of sample and device properties (Figure 5.9). These results not only give us a theoretical estimate for the device performance when processing different samples, but they also provide guidance in device design by demonstrating that sensor volume should be minimized to achieve the lowest error rate for a given particle density. By the same token, the particle density can be tuned through dilution to achieve a target error rate for a given sensor network design.

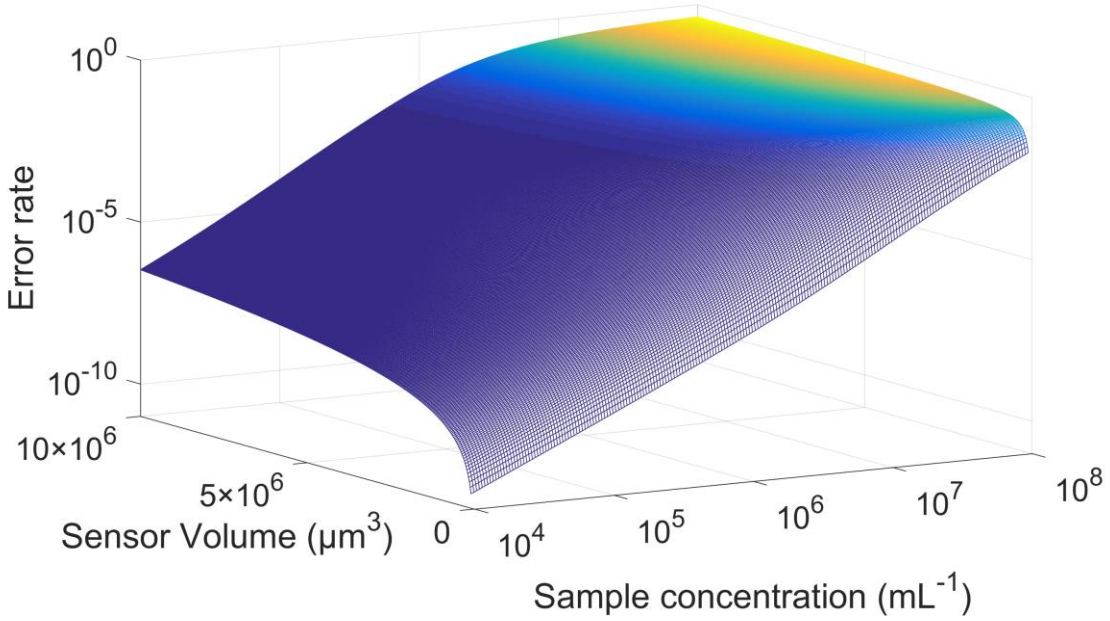

Figure 5.9 – Theoretical analysis of the effect of sensor signal interference due to coincident cells on the decoder performance. The estimated bit error rate in the decoder as a function of the sample concentration (i.e., number of particles per unit volume) and the sensor network size (i.e., the total volume of liquid monitored by the sensor network)

5.4 Electrode Layout Optimization

Because code waveforms are generated through physical interaction between electrodes and flowing particles, the layout of electrodes needs to be optimized at both the individual sensor-level and the network-level to maximize performance.

At the sensor-level, the electrode pitch is an important parameter that determines the pulse duration, which corresponds to the "chip duration" [118,123] in a conventional CDMA system. In our device, the center-to-center distance between two common-electrode fingers defines the spatial extent of individual bits. When this distance is less than the particle size, inter-symbol interference occurs between adjacent bits and the code waveform is distorted. When the distance is larger than the particle size, there are two

drawbacks: First, the baseline microfluidic channel impedance will be higher, and therefore the SNR in the detection of impedance modulation due to particles will be lower. Second, spacious bits will result in larger sensors to implement the same code and therefore will lead to more cell coincidence and higher error rate. Therefore, the optimum solution to this trade-off is to design bits similar in size to the target particle. In our model device (Figure 5.10), we employed 5 μm-wide electrodes separated by 5 μm gaps to create a 20 μm bit size, specifically based on the 15 μm mean diameter of the target cell population.

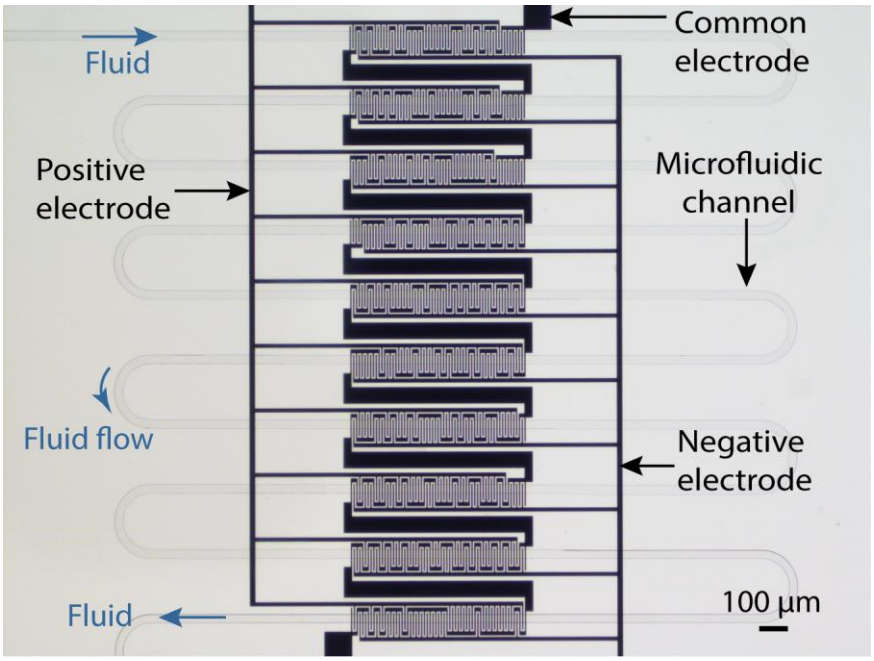

Figure 5.10 – An image of the microfluidic device used to characterize the performance of different sensor network layouts. A serpentine microfluidic channel in the device ensures all sensors in the network to interact with the same particle.

At the network-level, the number of sensors and their locations determine the length of electrodes used in building the circuit, which needs to be optimized to minimize resistive losses. Inevitably, a greater number of networked sensors encoding longer code sequences require more coding electrode pairs, resulting in longer electrode traces. Importantly, in

our device layout, two sensing electrodes are placed freely and the common electrode is placed between two electrodes meanderingly to generate bipolar signals. As a result, the scaling of the sensor network leads to a dramatic increase in the length of the common electrode trace (Figure 5.10). In estimating the resulting electrode resistance, the minimum length of Gold sequences (i.e., # of bits, denoted by b) required to multiplex m sensors on the microfluidic chip can be calculated as

$$b = 2^n - 1 \tag{5.10}$$

where

$$n = \lceil \log_2(m-1) \rceil + \left\lfloor 1 - \frac{\lceil \log_2(m-1) \rceil - \left\lfloor \frac{\lceil \log_2(m-1) \rceil}{4} \right\rfloor \times 4}{4} \right\rfloor \tag{5.11}$$

For an m-sensor network, with each sensor coded b bits using an array of $l \times w$ sized electrodes separated by a distance of g, the minimum length (L) of the common electrode can be parametrically expressed as

$$L = 2mb(w+g) + m\frac{b}{2}l \tag{5.12}$$

This expression assumes an average of $\frac{b}{2}$ bit polarity changes (“01” or “10”) in a b -bit long Gold sequence since it is a pseudorandom noise sequence. Each polarity change requires a common electrode crossover in the sensor geometry adding to the trace length (Figure 5.10). For a 10-sensor network constructed with 5-μm electrode fingers, the total

length of the common electrode can be more than 20 mm, leading to the electrode resistance values on the order of tens of kiloohms (Figure 5.11).

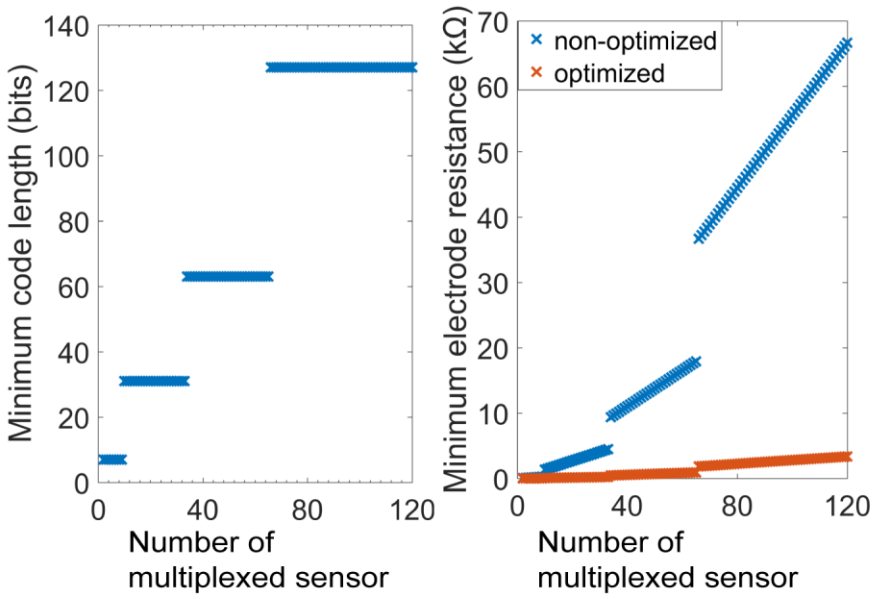

Figure 5.11 – Calculated minimum Gold code length (# of bits) (left) and the minimum common electrode resistance required to implement such a code (right) for both non-optimized (blue) and optimized (red) devices as a function of the number of multiplexed sensors in the sensor network.

We experimentally investigated the effects of the potential drop over the common electrode due to higher trace resistance using a device with sensors serially placed along a serpentine-patterned microfluidic channel. This analytical device configuration allowed us to directly compare signals from different sensors along the microfluidic path, since all sensors interacted with the same cell sequentially, eliminating the effects of the size and electrical properties of the cell. When non-optimized, the signal power was observed to gradually decrease with increasing distance between the sensor and the driving voltage source (Figure 5.12). This is problematic for the device operation since (1) it reduces the SNR in measurements and risks weaker signals from farther sensors to be buried in noise,

(2) it introduces artifacts in the output by creating a non-uniform sensitivity between sensors in the network, leading to bias in error rates.

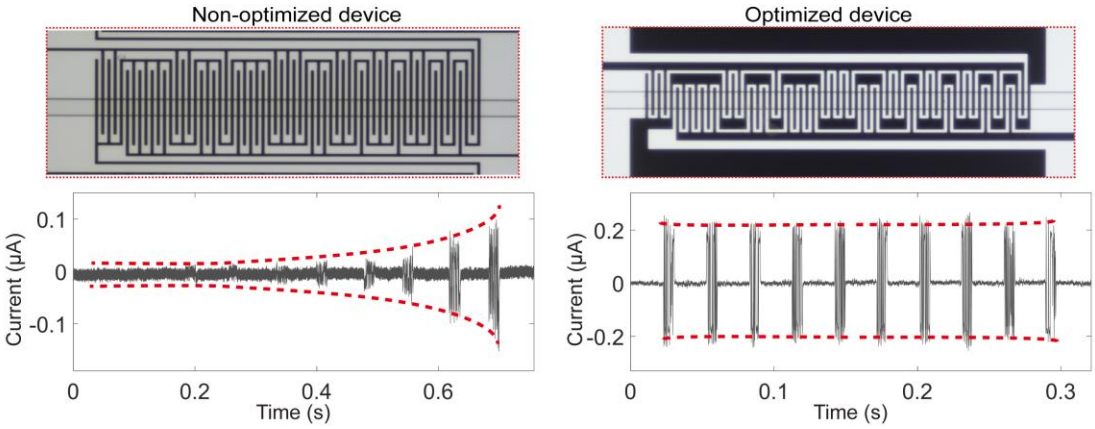

Figure 5.12 – Optimization of the sensor network layout to maximize SNR. Close-up images and the recorded sensor signals of a representative sensor layout in non-optimized (left) and optimized (right) devices. A comparison of waveforms shows the improvement in sensor signal uniformity achieved by optimized design.

To optimize the network design for signal uniformity among sensors, we systematically investigated the effects of the device geometry, film thickness, and the electrode material in minimizing the common electrode resistance (Figure 5.13). We optimized the device geometry in several ways. First, we increased the width of sections of the common electrode that fell outside of the microfluidic layout. Note that the width of the coding electrodes crossing the microfluidic channel remained unaltered to preserve the electrode pitch so that code waveform is generated without inter-symbol interference. Second, we shortened redundant parts of the electrodes that were specifically reserved to accommodate fabrication misalignment between the microfluidic layout and the coding electrodes. In addition to the structural modifications on the electrode network layout, we also applied the driving voltage from both ends of the common electrode trace, effectively halving the peak trace length. With these geometrical modifications alone, we were able to

significantly reduce the signal variation among sensors (Figure 5.13(a)). Next, we explored globally increasing the thickness of the electrode network. Because the resistivity of gold decreases nonlinearly with its thickness for a thin (~100 nm) layer of gold [145], increasing the gold film thickness to 480 nm decreased the electrode trace resistance beyond what would be expected from geometrical scaling of the electrode cross-section (Figure 5.13(b)). Finally, we compared gold to platinum, another metal commonly used to build electrolyte-interfacing sensors, as the electrode material and found that higher resistivity (~4.5×) of the platinum resulted in not only greater attenuation of signals with the trace length, but also a polarity-wise unbalanced response due to higher resistance mismatch between the two sensing electrodes (Figure 5.13(c)). Combining these results, we developed an optimized device with significantly reduced trace resistance that produced a uniform response among sensors in the network, demonstrating a negligible voltage drop over the common electrode trace (Figure 5.12).

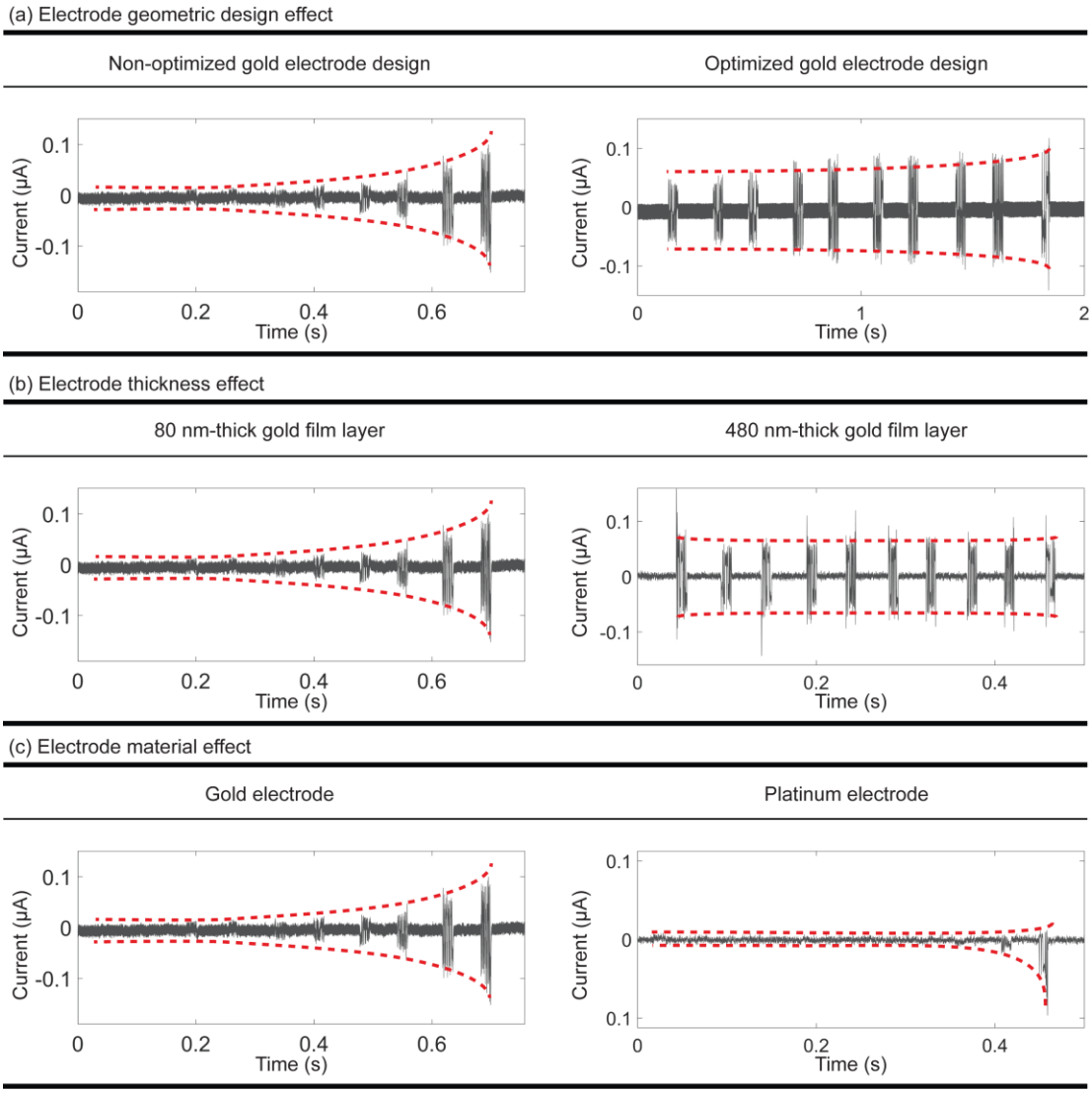

Figure 5.13 – Comparison of recorded signals from the serpentine devices with electrodes fabricated with different (a) geometries, (b) film thicknesses, and (c) materials.

5.5 Processing of Microfluidic Sensor Network Data

From the perspective of the hardware setup and signal acquisition, our device operates very similarly to a conventional Coulter counter, as the electrodes are driven by an AC source, and the output waveform consists of fluctuations due to flowing particles intermittently changing the impedance between electrodes (Figure 5.14). However, unlike a conventional Coulter counter, data from the network of coded Coulter counters (i.e.,

sensors) includes an additional layer of information and the output signal should be computationally analyzed to recover signals coming from different locations on the microfluidic chip.

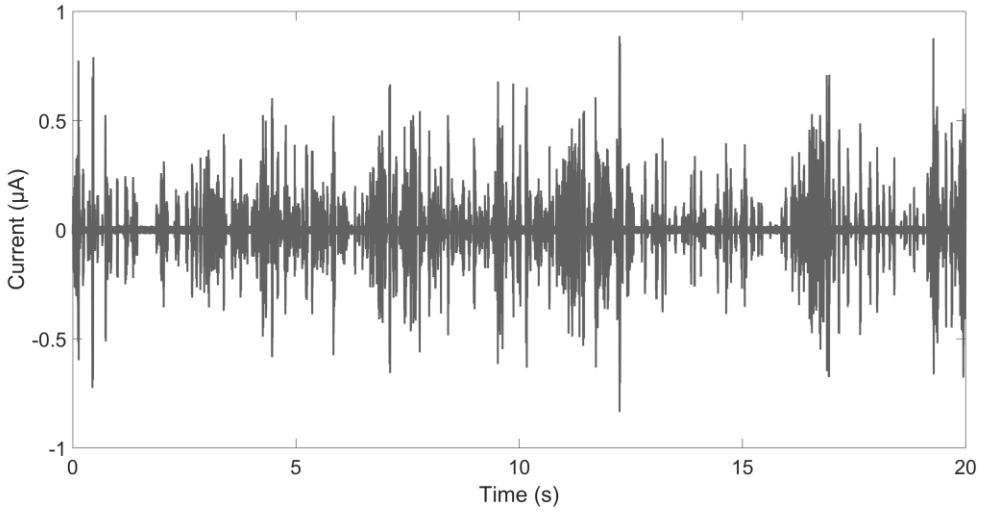

Figure 5.14 – A 20-second-long waveform arbitrarily selected from the recorded data from the microfluidic device processing suspended human cancer cell line. The waveform consists of transients due to flowing cells over the sensor network.

To process sensor network data, we developed a LabVIEW program to implement custom decoding algorithms (Figure 5.15). In the program, the data signal, initially oversampled (50 kHz) to prevent aliasing, was first low-pass-filtered (with a cut-off frequency of 5 kHz) to eliminate the high-frequency noise. The whole waveform was first analyzed to eliminate idle time frames with no sensor activity to increase the efficiency of the decoding process. To identify idle time frames, the zero-crossing rate (ZCR) was used as the discrimination parameter, as ZCR for noise is expected to be greater than that of sensor signals. Specifically, ZCR was calculated for every 200 samples (20% of the estimated particle transit time), and only time frames with ZCR < 0.2 were considered as sensor-active time frames (containing sensor signals).

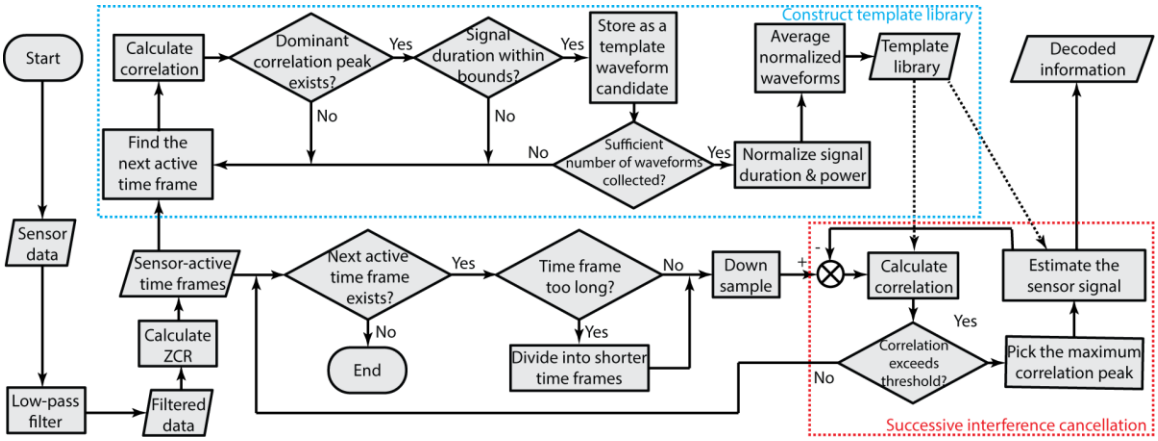

Figure 5.15 – Computational processing of sensor signals to recover individual sensor signals. The schematic showing the process flow of the developed decoding software. Following the filtering of the input signal, templates are automatically obtained from the input signal. The waveform is divided into time blocks, which are individually correlated with templates. A successive interference cancellation algorithm iteratively decodes the interfering signals starting from the sensor signal with the highest power

Next, sensor-active time frames were analyzed to create a template library based on the recorded sensor signals. In this process, we provided the set of digital codes implemented in the device, dimensions of the microfluidic device and the volumetric flow rate of the sample to the program, which used these parameters to automatically search the acquired data for the sensor signal waveforms. A waveform was only scored as a template waveform if (1) it produced a dominant correlation peak with only one of the codes in the provided codeset (i.e., the amplitude of the largest correlation peak was more than twice of that of the secondary correlation peak) and (2) the waveform duration was in agreement with the one calculated based on the expected particle flow speed (i.e., the signal duration was within 150% of the estimated signal duration). These conditions guaranteed that only non-interfering waveforms due to target particles were considered in template generation. Scored waveforms were then clustered for individual sensors, and when the program accumulated enough (n>20) waveforms for each sensor, time- and power-normalized waveforms were averaged to obtain the templates. Construction of the template library

based on the experimental data is important as it allowed us to accommodate variations in the signal due to artifacts in device fabrication.

Once the template library was established, we processed the recorded sensor network data using a decoding algorithm based on the successive cancellation of interfering signals [116]. Sensor-active time frames were transferred from the previous step, and the prolonged ones (with a duration greater than 5× of the expected particle transit time) were divided into shorter time frames. Then all time frames were down-sampled by 5× to increase the decoding efficiency and then analyzed individually using successive interference cancellation. Each time frame was first compared with the template library through correlation, and the largest correlation peak and the matching template were used to reconstruct the signal with the most power. Following the subtraction of the estimated signal from the signal frame, the algorithm recursively searched for the coincident sensor signals by eliminating the strongest signal until the correlation of the residual signal with the template library could not exceed a predetermined threshold value. At the end of the process, the original output waveform can be decomposed into data streams from individual sensors (Figure 5.16). These data not only include the locations of the particles on the microfluidic chip based on the unique sensor waveform but also provides information on the size and the speed of each particle based on the signal amplitude and duration, respectively.

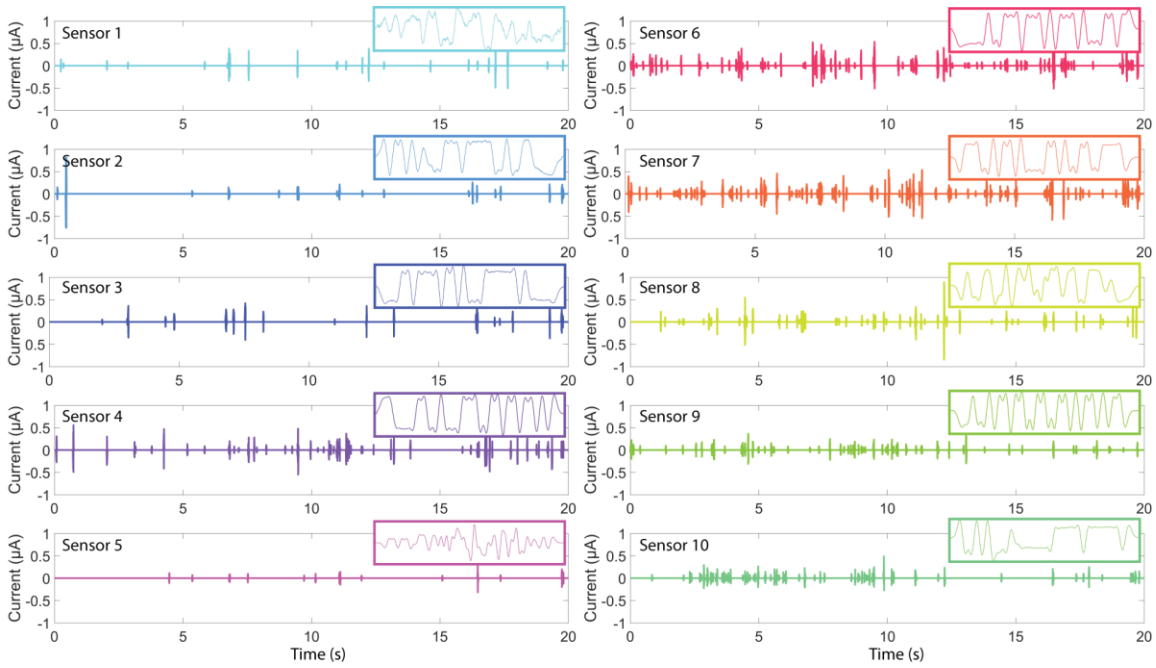

Figure 5.16 – The signals generated by each sensor in the network are recovered from an arbitrarily chosen 20-second-long waveform (See Figure 5.14). Individual sensor waveforms reconstructed based on the correlation amplitude and the matching template are illustrated. Templates used to recover sensor signals are also provided for each sensor waveform.

5.6 Conclusions

Microfluidic CODES is a platform technology that enables distributed Coulter detection of particles across a microfluidic chip. It employs sensors micromachined to generate distinct waveforms that can uniquely be linked to different locations on a microfluidic chip for a code-multiplexed readout. The number of code-multiplexed sensors can be increased to enhance the utility of this sensing approach by designing individual sensors to generate signals that are computationally distinguishable from each other. Interference among code-multiplexed Coulter sensors increases with the network size decreasing the SNR, and therefore, the sample concentration should be adjusted to achieve a target error rate for a given size of the network. Design and physical implementation of the scaled sensor network should also prioritize the minimization of the electrode trace

resistance to ensure a uniform response from the sensors in the network. The theoretical, experimental, and the algorithmic framework established in this paper will enable the development of distributed Coulter sensor networks with higher complexity.

CHAPTER 6. AN ALTERNATIVE: THE BLANKET ELECTRODE COULTER COUNTER [158]

Microfluidic devices integrated with Coulter sensors have been widely used in counting and characterizing suspended particles. In most microfluidic devices, Coulter sensors are created by micromachined coplanar electrodes on the floor of microfluidic channels rather than utilizing the full channel geometry [159-163]. While coplanar electrodes can be realized with a simple fabrication process that is compatible with the soft lithography, they not only generate non-uniform electric field affecting sensor performance (Figure 6.1), but also complicate the design of large-scale multiplexed electrical sensor networks (e.g., Microfluidic CODES sensors) [153,164-166], due to the need to route multiple electrode traces on a plane, as we mentioned in Chapter 5.

The use of counter-facing parallel electrodes in microfluidic channels can address the aforementioned problems. However, conventional approaches to build a parallel-electrode Coulter sensor in microfluidic devices typically rely on forming a glass-polyimide-glass sandwich structure [167], which not only involves complex fabrication process that requires a critical alignment between layers but also lacks the benefits of molded biocompatible polymers employed in the soft-lithography process [168-172]. To address these issues, in this chapter, we introduce a simple and robust fabrication method, compatible with soft lithography, to create parallel-electrode sensors in microfluidic devices, which we called blanket electrode Coulter sensors [158]. Also, we comparatively analyze the performance of coplanar-electrode and parallel-electrode Coulter sensors using computer simulations and experiments.

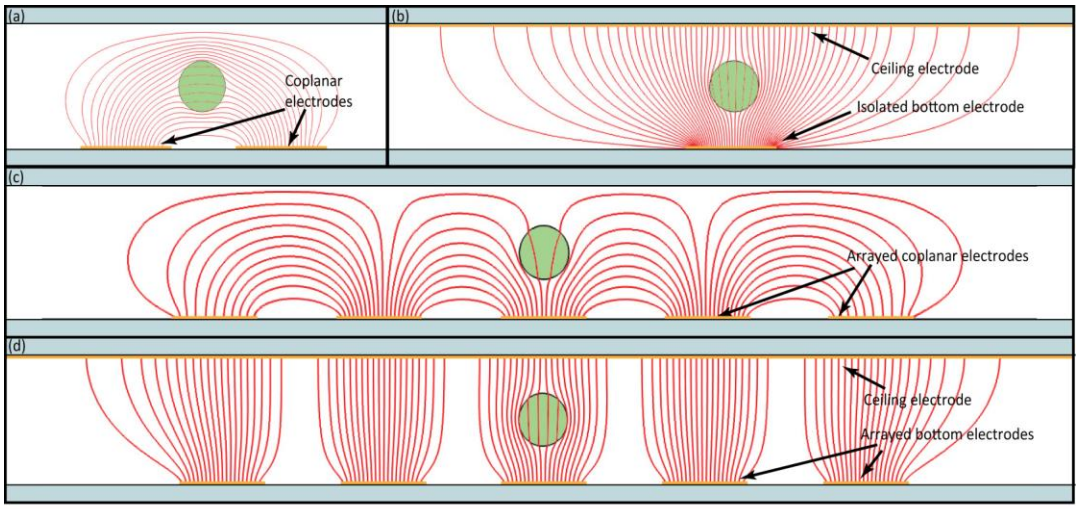

Figure 6.1 – Simulation of the electrical field distribution generated by (a)(b) isolated coplanar (a) and parallel (b) electrode sensor, and (c)(d) arrayed coplanar (c) and parallel (d) electrode sensors fabricated using our approach.

6.1 Device design, fabrication, and characterization

In our method, one of the electrodes of the Coulter sensor is formed by a thin metal film blanket-deposited on the inner walls of a microfluidic channel, while the other electrodes are lithographically patterned on the substrate according to the desired arrangement. We selectively deposit a metal film onto the inner surface of a PDMS microchannel as one of the sensor electrodes. When this metal-coated PDMS is bonded to the micropatterned surface electrodes, parallel-electrode sensors are formed. The electrode covering the microfluidic channel is conceptually analogous to ground planes in printed circuit boards and significantly simplifies the sensor network layout.

The device consists of a glass substrate with micropatterned gold electrodes fabricated using a lift-off process and a PDMS microfluidic channel fabricated with a soft lithography process (Figure 6.2). A thin layer of negative photoresist was spun and patterned on a glass wafer using an optical lithography process, followed by the

evaporation of a 20/80 nm Cr/Au stack. The wafer was then transferred to an acetone bath to remove the non-patterned region and diced into individual chips. The PDMS layer was created from a 15 μm-thick SU-8 mold patterned with photolithography. After the fluidic inlet, outlet, and the electrical auxiliary holes were created using a biopsy punch, the inner walls of the PDMS microchannel were coated with a 100 nm-thick gold film with sputtering. Next, the coated PDMS substrate was transferred onto a sticky tape to selectively remove the gold-sputtered on the surface to prevent short circuits while leaving the gold within the microfluidic channel intact. Next, the PDMS and glass substrates were activated in oxygen plasma, aligned under a microscope, and bonded. Finally, we injected a conductive epoxy-coated wire from the auxiliary electrical port to form an electrical connection to the blanket electrode and created the final device.

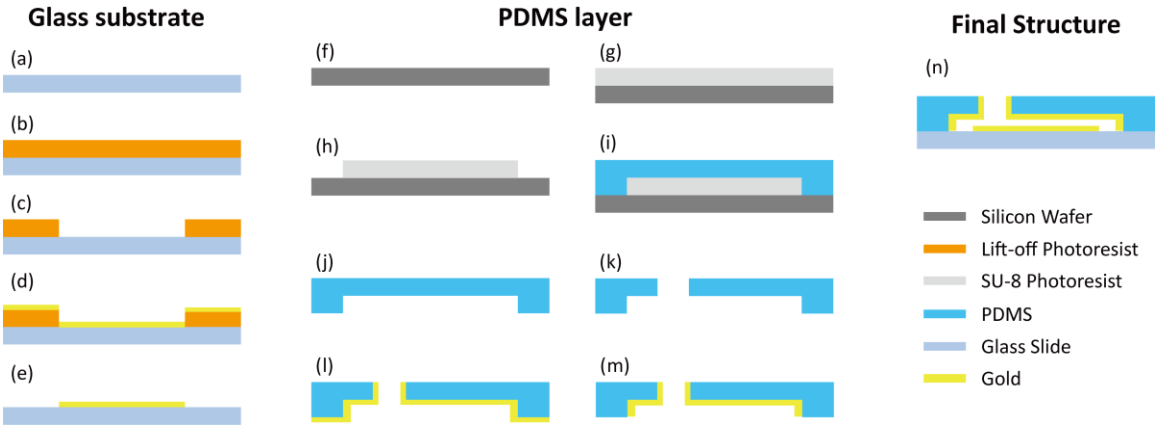

Figure 6.2 – The schematic showing the fabrication process to create parallel electrodes in a microfluidic device. (a)~(e) The fabrication of the glass substrate with micropatterned surface electrodes. (f)~(m) The fabrication of the metal-coated PDMS microchannel. (n) Bonding of the two components to form the final device.

We used cultured human breast cancer cells (MDA-MB-231) suspended in PBS as a sample to test our devices. The sample was driven through the microfluidic device using a syringe pump at a flow rate of 100 μL/h.

To measure the change in electrical impedance of the microfluidic channel in response to flowing cells, we excited the sensor with 500 kHz sine wave and measured the resulting electrical current flow. The current signals from both sensors were first converted into voltage signals using transimpedance amplifiers, and then measured using a lock-in amplifier.

Our results show that individual cells flowing in microfluidic channels could be detected from the differential current signal (Figure 6.3).

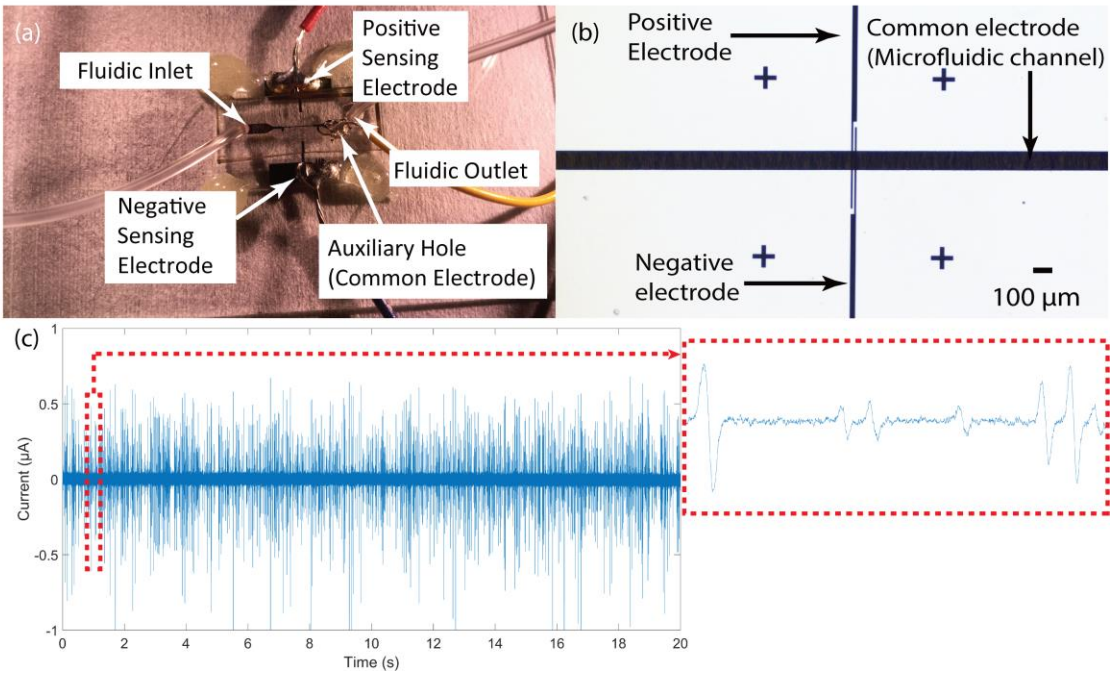

Figure 6.3 – Images of the fabricated microfluidic device and characterization results. (a) A photo of the fabricated device with fluidic and electrical connections and (b) a close-up of the parallel electrode sensor. (c) Approximately 2500 cancer cells were detected by the sensor during 20 s period. (d) A close-up figure showing the signals for 7 detected cells in 0.04 s.

6.2 Comparison between different structured Coulter sensor

6.2.1 Finite element analysis

We used COMSOL Multiphysics v5.3 AC/DC module to simulate Coulter sensor operation with coplanar or parallel electrode configurations and compared their performance. We first simulated electric field distribution within a microfluidic channel for different electrode configurations (Figure 6.1). When electric field distributions due to a single pair of coplanar electrodes (Figure 6.1(a)) and an electrode paired with a parallel blanket electrode (Figure 6.1(b)) are compared; while the parallel electrode configuration provides a more uniform electric field throughout the height of the microfluidic channel, it also leads to a broadened non-uniform field distribution due to fringing effects due to the size mismatch between ceiling and bottom electrodes. This fringing effect could partially be alleviated by arraying bottom electrodes, which limits the broadening of the field for the inner electrodes (Figure 6.1(d)) and provides a more uniform electrical distribution compared to arrayed coplanar electrodes (Figure 6.1(c)).

To quantitatively analyze the sensor performance, we calculated the electrical current flow in the microfluidic channel and compared the amplitude of electrical current modulation in response to particles flowing between the electrodes. For these calculations, we assumed PBS as the electrolyte and human cells as suspended particles. Corresponding electrical parameters used in our simulations for modeling particle-electrode interaction are summarized in Table 6.1.

Table 6.1 – Parameters used in computer simulations

Parameter	Cell count
Media conductivity	1.4 S m^{-1}
Media relative permittivity	80
Cytoplasm conductivity	0.5 S m^{-1}
Cytoplasm relative permittivity	60

We first calculated the decrease in electrical current as a measure of the sensor sensitivity for a 10 μm-diameter cell at multiple vertical positions in a 30 μm-wide microfluidic channel that is 15 μm- (Figure 6.4(a)), 35 μm- (Figure 6.4(b)), or 65 μm-high (Figure 6.4(c)). We considered three different electrode configurations: A coplanar electrode pair (Figure 6.1(a)), a surface electrode in parallel to a larger ceiling electrode (Figure 6.1(b)), and a surface electrode paired with an electrode that covers both the ceiling and the sidewalls of the microfluidic channel. Because the ceiling electrode extends over the sidewalls of the microfluidic channel with our fabrication technique, sidewalls need to be considered especially for a narrow microfluidic channel. In our 3D simulations, we assumed that the cells were flowing in the central streamline (i.e., center-positioned 15 μm from each sidewall). We found the current modulation for the parallel-electrode sensor to be higher than the coplanar-electrode sensor for the same particle. The enhancement in sensitivity was more pronounced for cells at elevated vertical positions due to the electrical field being confined to the floor of the microfluidic channel for coplanar electrodes. We also observed that the extension of the ceiling electrode over the sidewalls increased the parallel-electrode sensitivity only when a cell was positioned below a crossover elevation.

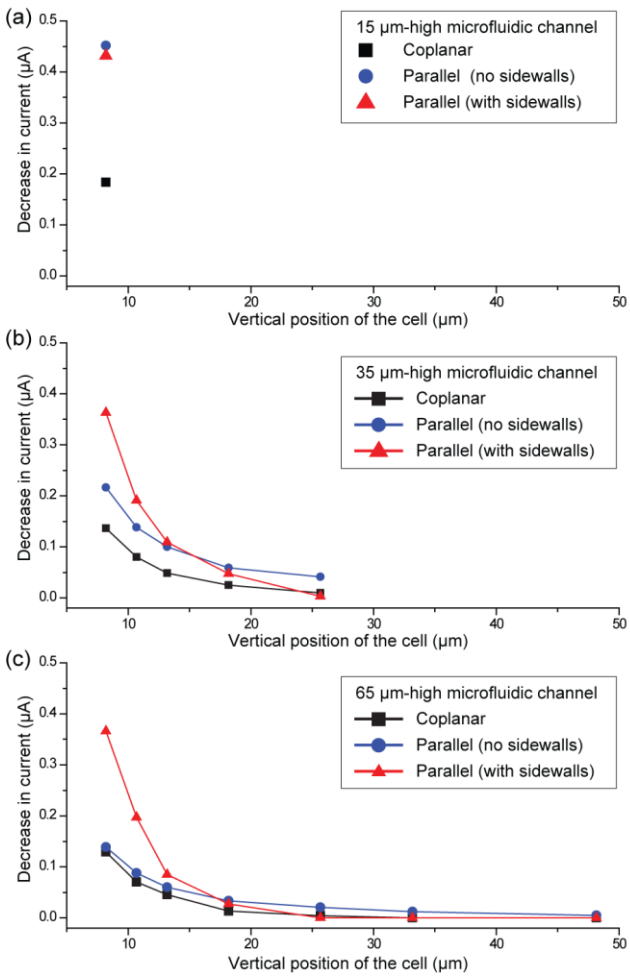

Figure 6.4 – Simulated electrical current modulation in response to cells in microfluidic channels integrated with different electrode configurations. A 10 µm-diameter cell is positioned in the center streamline of the 30 µm-wide microfluidic channel with (a) 15 µm-, (b) 35 µm-, and (c) 65 µm-height. The current modulation is simulated for a cell at various vertical positions for each scenario.

We also investigated the effect of the cell size on the sensitivity of coplanar- and parallel-electrode sensors. We specifically compared the decrease in electrical current for the parallel- and coplanar-electrode configurations in a 35 µm-high and 30 µm-wide microfluidic channel for 6 µm-, 10 µm-, and 14 µm-diameter cells. Based on these simulations (Figure 6.5), we concluded that the sensitivity enhancement is higher for smaller cells (2~5× for 6 µm diameter cell) than larger cells (1.5~2× for 14 µm-diameter

cells). In addition, the effect of the cell size on the sensitivity enhancement was found to be generally higher for cells at higher elevations in the microfluidic channel.

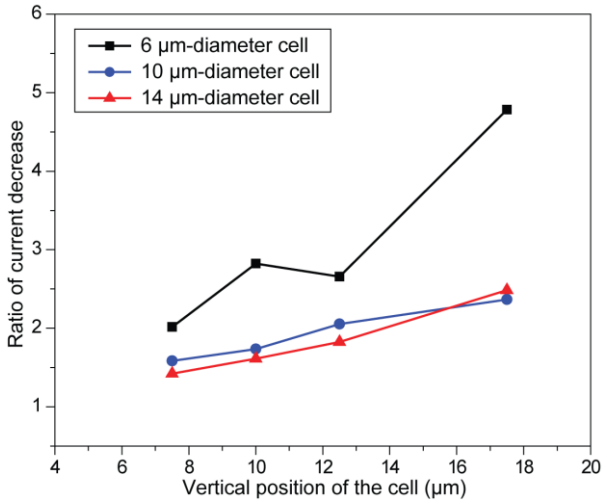

Figure 6.5 – The ratio of the simulated current modulation between a parallel-electrode and a coplanar-electrode sensor. The ratio was calculated for different cell sizes at different elevations in a 30 μm-wide and 35 μm-high microfluidic channel.

6.2.2 Experimental verification

To experimentally compare the performance of coplanar- and parallel-electrode Coulter sensors, we created a microfluidic device that integrates two sensors based on coplanar electrodes and parallel electrodes along the same microfluidic channel (Figure 6.6). On the left side of the microfluidic channel, two 5 μm-wide coplanar electrodes separated by a 5 μm gap were created on the glass substrate. On the right side of the microfluidic channel, the inner walls of the microfluidic channel are coated with a gold film, and only a single 5 μm-wide surface electrode was created on the glass substrate (Figure 6.6(b)). Because the same particle flowing in the microfluidic channel sequentially interacts both sensors, this experimental platform allowed us to directly compare signals from the two sensors.

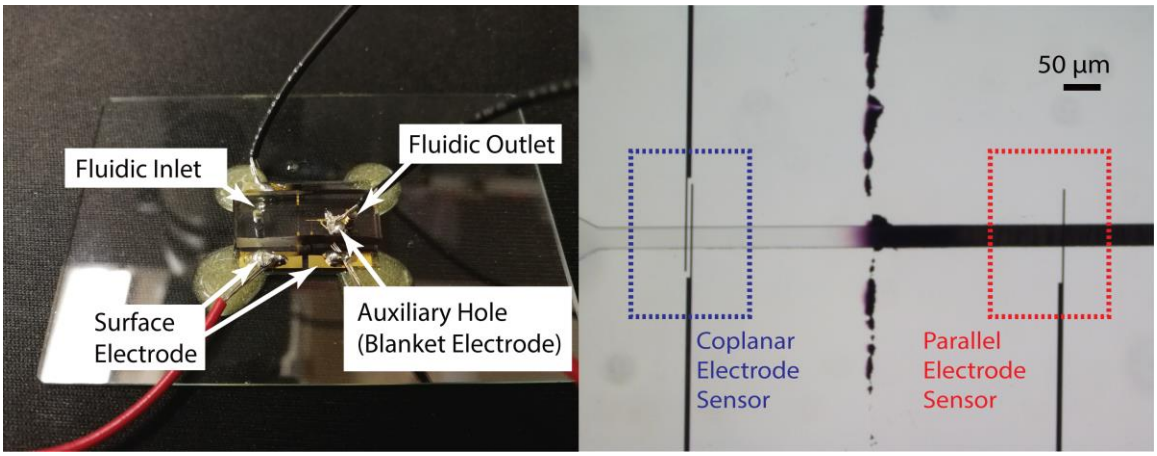

Figure 6.6 – Images of the fabricated microfluidic device that contains both the coplanar- and parallel-electrode sensors. (a) A photo of the final device with fluidic and electrical connections and (b) a close-up microscope image of the two sensors formed along the same microfluidic channel.

We used the same settings as we used in the device characterization (Section 6.1) to measure the change in electrical impedance of the microfluidic channel in response to flowing cells in this device. We excited both coplanar- and planar-electrode sensors with a 500 kHz sine wave and measured the resulting electrical current flow. In our measurement setup, we excited both sensors with the same AC signal from the common electrode (i.e., the surface electrode for the coplanar-electrode sensor and the blanket electrode for the parallel-electrode sensor), and acquired the current from the surface electrode for each sensor.

We compared the two sensor output waveforms containing signals for ~200 cells and found that the current modulation amplitude was 2~4× higher for the parallel-electrode sensor compared to the coplanar-electrode sensor for the same cell (Figure 6.7). These results agree well with our simulation results.

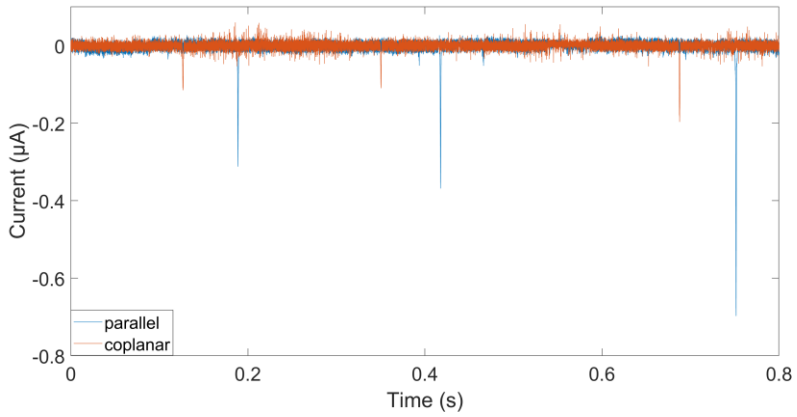

Figure 6.7 – Electrical current modulation in response to the same cell recorded from a coplanar-electrode and a parallel-electrode sensor sequentially placed on the same microfluidic path. The microfluidic channel is 15 μm-high and 30 μm-wide. The peak signal amplitudes generated due to the same cell are 2~4× higher for the parallel-electrode sensor.

6.3 Blanket electrode Coulter sensor device

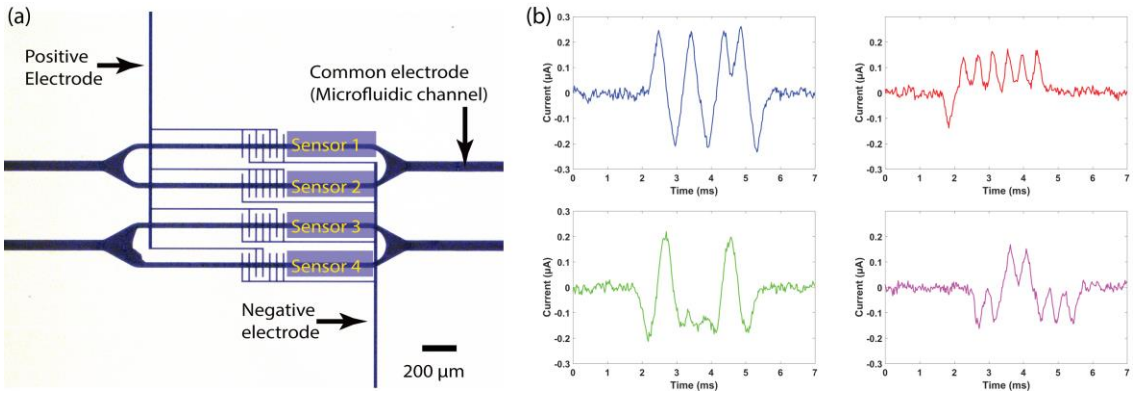

Figure 6.8 – Microfluidic CODES device formed by parallel electrodes and the resulting representative signals from individual sensors. (a) A close-up image of the 4-sensor Microfluidic CODES device fabricated by the reported method. Sensors are encoded with orthogonal digital codes "1010110", "0111111", "0100010", "0011000", respectively. (b) Representative signals corresponding to each sensor in the device shown in (a).

We also fabricated a device with a network of four code-multiplexed sensors encoding 7-bit orthogonal Gold sequences (Figure 6.8) [116]. The recorded signals from each sensor showed that our approach was able to generate distinct bipolar code signals

from an electrode layout that was significantly simplified compared to the coplanar electrode arrangement otherwise required to generate similar signal waveforms.

6.4 Conclusions

In this chapter, we introduced a simple and robust fabrication procedure that can create parallel-electrode Coulter sensors in microfluidic devices. Our technique not only produces more uniform electric fields than conventional coplanar electrodes, but also is more suitable for the construction of complex electrical sensor networks in microfluidic devices due to greater layout flexibility. We also comparatively analyzed the performance of the parallel-electrode Coulter sensor against the conventional coplanar-electrode Coulter sensor for microfluidic devices fabricated using soft lithography. Based on both computer simulation results and experiments with cell suspensions, we found that the parallel-electrode Coulter sensor yields a higher sensitivity than the coplanar-electrode Coulter sensor, and the sensitivity enhancement is a function of the cell size, elevation, and microfluidic channel geometry.

CHAPTER 7. THE ALL ELECTRONIC ANTIBODY MICROARRAY [173]

In this chapter, we will integrate the multiplexed sensor network technique, Microfluidic CODES, with the antibody microarray as mentioned earlier that is used for the detection of multiple cell surface markers on the cells, to create the all-electronic microfluidic antibody array for the immunophenotyping of cell populations, whose results are acquired by only one electrical readout. The microfluidic device consists of an array of microfluidic cell capture chambers, each functionalized with a different antibody to recognize a target antigen, and a network of code-multiplexed Coulter counters placed at strategic nodes across the device to quantify the fraction of cell population captured in each microfluidic chamber (Figure 7.1). With our technique, we interpret the electrical data providing cell capture statistics across the device in light of the specific antibody sequence each cell was subjected to, for calculating the prevalence of different subpopulations in a sample. Moreover, by electrically coding cell capture data, we compress the cell capture statistics across the whole device into a single electrical output without any information loss. The development of our device provides exciting opportunities for the diagnosis of various disease types at the point of care or resource-limited settings.

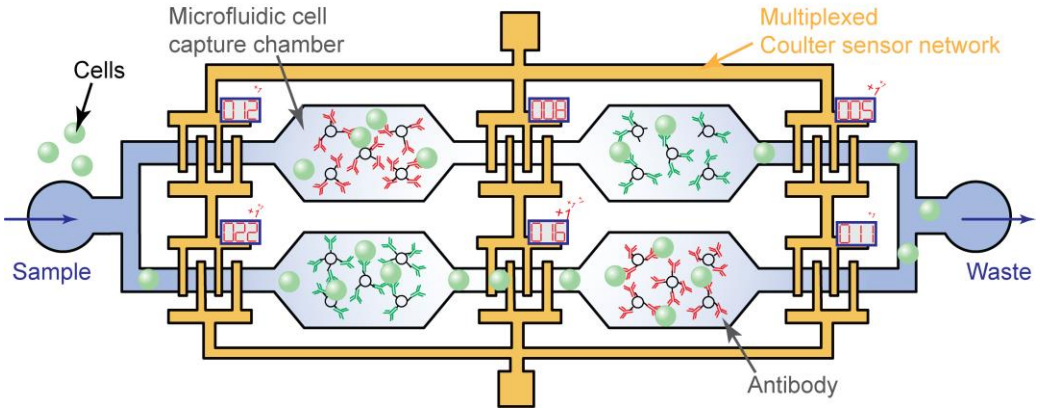

Figure 7.1 – A schematic showing the operation of the device. Each microfluidic cell capture chamber is functionalized with a different antibody. Cells expressing the target antigen are immunocaptured in the microfluidic chambers. The number of captured cells in each chamber is determined by an on-chip network of electrical sensors placed at strategic nodes across the device.

7.1 Device design and operation

In this chapter, we designed and fabricated a two by two microfluidic antibody microarray with an electrical readout as a representative of our device (Figure 7.2). The device is composed of a PDMS microfluidic layer that accommodates the cell capture chambers (Figure 7.2, top right) and a glass substrate with a code-multiplexed Coulter sensor network made up of micropatterned gold electrodes (Figure 7.2, bottom right). In the microfluidic layer, the sample inlet bifurcates into two separate microfluidic paths, with each path consisting of two cascaded cell capture chambers. In both microfluidic paths, cells sequentially interact with two different antibodies immobilized in the microfluidic chambers before all cells are merged and discharged from the waste outlet. Code-multiplexed Coulter sensors log each and every cell as the cell enters the device if it passes from one capture chamber to another, and if it gets discharged from the device, to determine

the antigen-positive cell count in each cell capture chamber from a mass balance calculation.

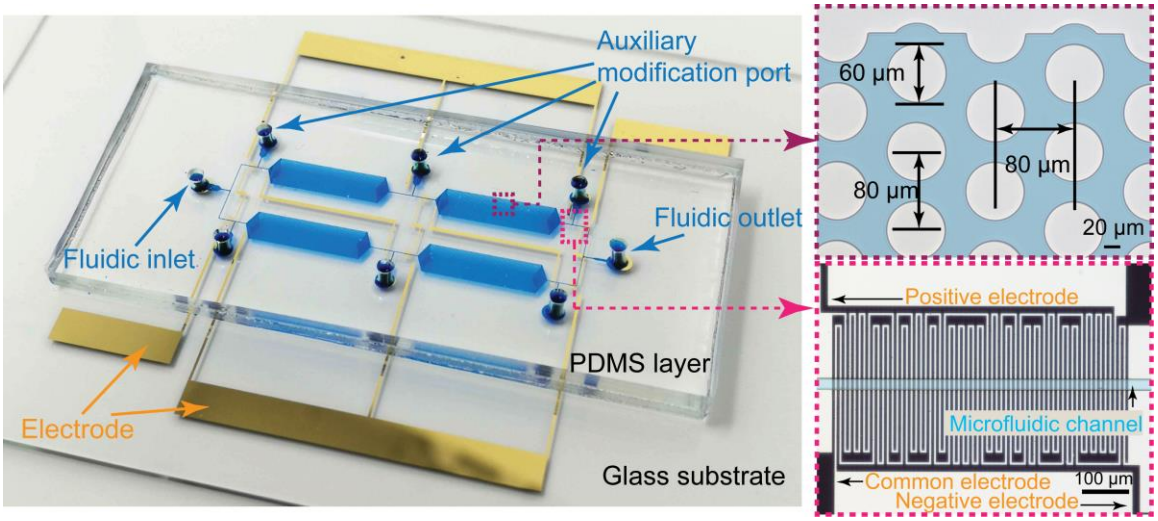

Figure 7.2 – The operation principle and the design of the electronic antibody microarray. (a) A photo of the fabricated device filled with blue dye for illustration. The fabricated device is made up of a PDMS layer with microfluidic channels and cell capture chambers, and a glass substrate with a micropatterned metal layer forming the sensor network. Besides the sample inlet and outlet, auxiliary ports were created on the microfluidic layer for selective functionalization of individual cell capture chambers. (b) A close-up image of the cell capture chamber. 60 µm-diameter pillars are arranged in a staggered array with an 80 µm-pitch, to enhance the cell capture rate. The channel is filled with a blue dye for visualization purposes. (c) A close-up image of one of the electrical sensors on the device. The sensor is specifically designed to form an electrode pattern to produce a 31-bit digital code (0111001011010000110100110011110), each time a cell flows over it. Other sensors are coded with different orthogonal codes enabling a code-multiplexed readout shared by all sensors.

In our device, microfluidic cell capture chambers replace antibody spots in a conventional assay and are designed to capture the cells expressing target surface antigens efficiently. Each cell capture chamber measures 9 mm in length and 3 mm in width. Within each cell capture chamber, we placed 60 µm-diameter pillars to increase the cell capture area and to structurally support the cell capture chamber ceiling (Figure 7.2, top right). The pillars form a staggered two-dimensional array with an 80 µm-pitch to increase the

likelihood of cell-pillar contact under laminar flow. To selectively modify each chamber with a specific antibody, we added a set of auxiliary functionalization ports in the PDMS layer. These auxiliary ports are located close to the inlet and outlet of each cell capture chamber (Figure 7.2), to exclusively deliver the functionalization reagents to the desired cell capture chamber. Following the functionalization process, auxiliary ports were sealed to prevent leakage during the assay, and the device was interfaced via a single fluidic inlet and outlet.

To functionalize cell capture chambers with antibodies, we employed a four-step chemical modification protocol at room temperature (Figure 7.3). First, the microfluidic device was wetted with ethanol, and within 10 minutes of the PDMS-glass bonding, (3-aminopropyl)triethoxysilane (APTES) in ethanol (2% v/v) was introduced to the device and incubated for 30 minutes. Second, the device was rinsed with ethanol and DI water and a glutaraldehyde solution in DI water (1% v/v) was introduced and incubated for 30 minutes. Third, the device was rinsed with DI water and PBS, and capture antibodies in PBS were introduced into the cell capture chambers and incubated for 1 hour. Fourth, the device was washed with PBS to remove unbound antibodies, and the cell capture chambers were incubated with bovine serum albumin (BSA) blocking buffer for 1 hour to block the non-specific binding sites. Finally, the device was rinsed with PBS to complete the functionalization process.

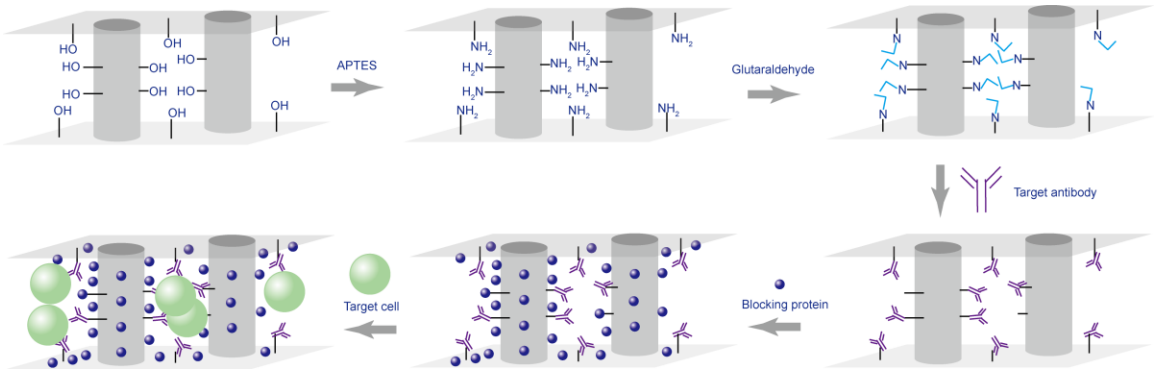

Figure 7.3 – A schematic showing the step-by-step functionalization process and specific chemistry used to immobilize antibodies on the device surface.

To selectively immobilize different antibodies in the intended cell capture chambers, we used auxiliary functionalization ports. In this process, capture antibodies for different cell capture chambers were simultaneously introduced into the device through their dedicated functionalization ports at the same flow rate (Figure 7.4(i)). Simultaneous injection of antibody solutions through symmetrically designed microfluidic paths combined with the laminarity of the flow ensured that each antibody is exclusively directed into the desired cell capture chamber without mixing with others. To minimize antibody loss from the waste ports in this process, Tygon tubes were employed to increase the hydraulic resistance of the waste path diverting most (>80%) of the solution into the capture chambers. The characterization of this concurrent functionalization approach using different colored dyes demonstrated its effectiveness with no observable crosstalk between different cell capture chambers (Figure 7.5). While the diffusion across different cell capture chambers during incubation may induce mixing, the distance between different chambers makes its effect negligible in the functionalization of cell capture chambers. The main advantages of our approach over the printing-based deposition of antibodies [3,174-176] are twofold: First, we can perform the whole functionalization process in a closed

chamber without exposing the antibodies to the ambient during buffer exchanges. Second, we functionalize all inner surfaces of the microfluidic chambers, which enhances capture efficiency. It should also be noted that except for the antibodies, auxiliary functionalization ports were used as outlets in the functionalization process for applying reagents common to all cell capture chambers (APTES and glutaraldehyde) (Figure 7.4(ii)). Once the functionalization process was completed, all auxiliary functionalization ports were sealed, the sample was introduced to the device from a common inlet, and the waste was discharged from the common outlet (Figure 7.4(iii)). Overall, our functionalization process utilizes the same chemistry employed for preparing immunoassays and can also be scaled to create larger assays with more antibodies.

We measured cell capture rates for all microfluidic chambers by electrically tracking cell flow on the assay with the integrated electrical sensor network. To detect coded impedance modulations from cells flowing across the microfluidic assay, the device was excited from the common electrode terminal with a 1 V sine wave at 500 kHz supplied from the output of the lock-in amplifier (HF2LI, Zurich Instruments), and the resulting current signals were acquired from the two sensing electrodes. The current signals were first converted into voltage signals using two transimpedance amplifiers, and then subtracted from each other with a differential amplifier to produce a single electrical waveform. The amplitude of the electrical signal was measured with the lock-in amplifier.

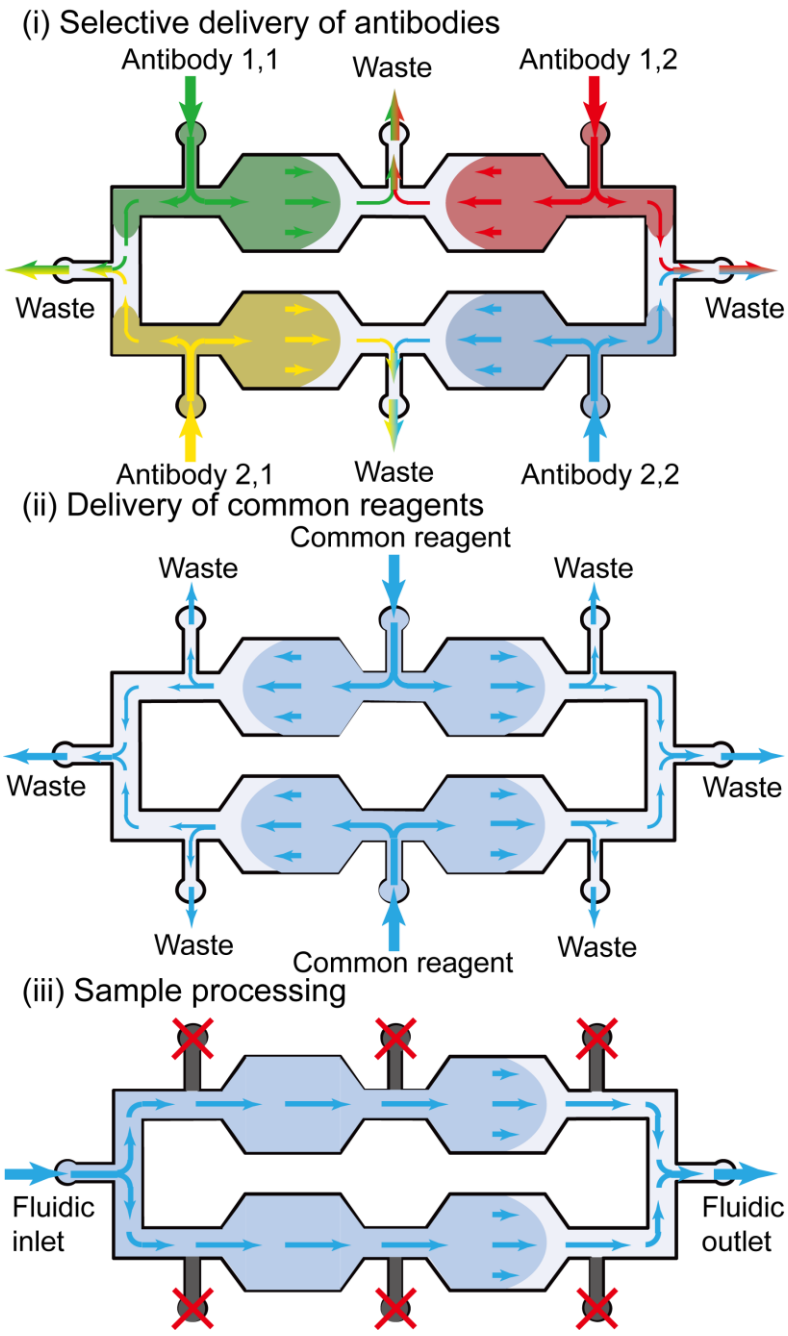

Figure 7.4 – Functionalization of the cell capture chambers. Computer drawings depicting different schemes for interfacing the device for surface functionalization and sample processing. (i) All four antibodies are simultaneously introduced from the auxiliary functionalization ports to specifically deliver the capture antibodies to the desired cell capture chamber. The laminar flow combined with the symmetric device design prevents any mixing between different antibody solutions. (ii) The buffers and reagents common to all cell capture chambers are introduced from an inlet and the auxiliary functionalization ports operate as outlets. (iii) Prior to sample processing, auxiliary functionalization ports are sealed. The sample is then introduced from a single inlet and the waste is collected from a single outlet.

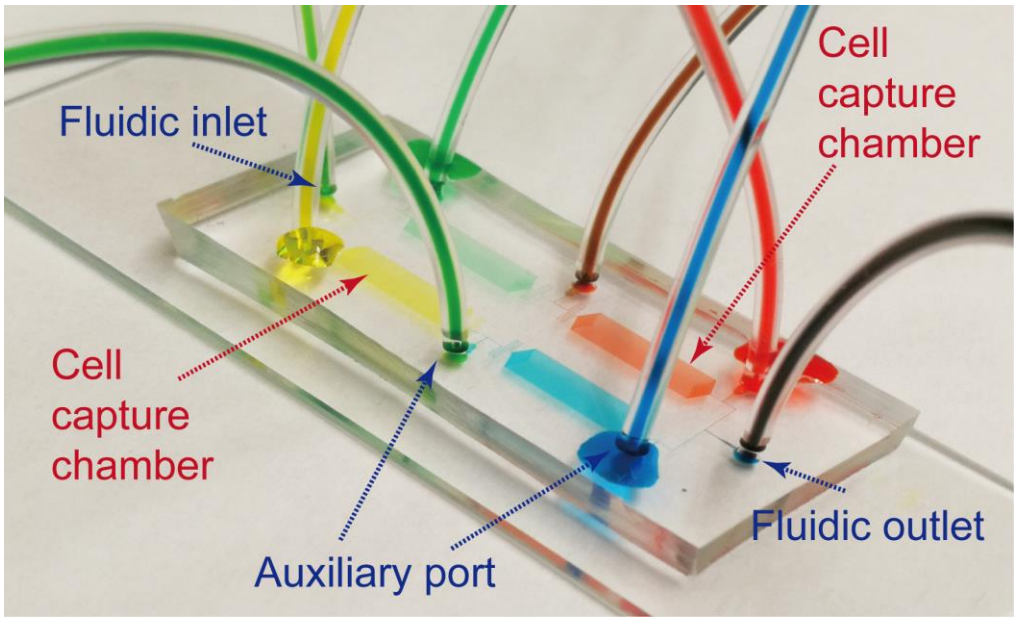

Figure 7.5 – A photo of a device, where four different solutions each containing a different colored dye could successfully be delivered to individual cell capture chambers using the developed process. Lack of mixing between different colors demonstrates the capability to specifically deliver different antibodies to corresponding microfluidic chambers.

During the assay, the sample was driven through the functionalized device by a syringe pump at a controlled flow rate and followed by a brief PBS wash to clear the device of remaining cells. The electrical signal from the device was acquired via electronic hardware and analyzed using a computer (Figure 7.6(a)). To determine the capture location for each cell processed on the device, we processed the output signal using a custom-built decoding algorithm (Figure 7.6(b)). The algorithm was implemented in the LabVIEW and processed the data with the minimal manual intervention [116]. Briefly, our algorithm first reviewed a part of the recorded electrical waveform, identified different code signals present, and classified them into different sensor groups. Once each sensor group contains a sufficient number of code signal instances, signals were normalized and averaged to form a library of code templates that correspond to each and every sensor in the network. The generation of templates based on recorded signals from the sample itself made the

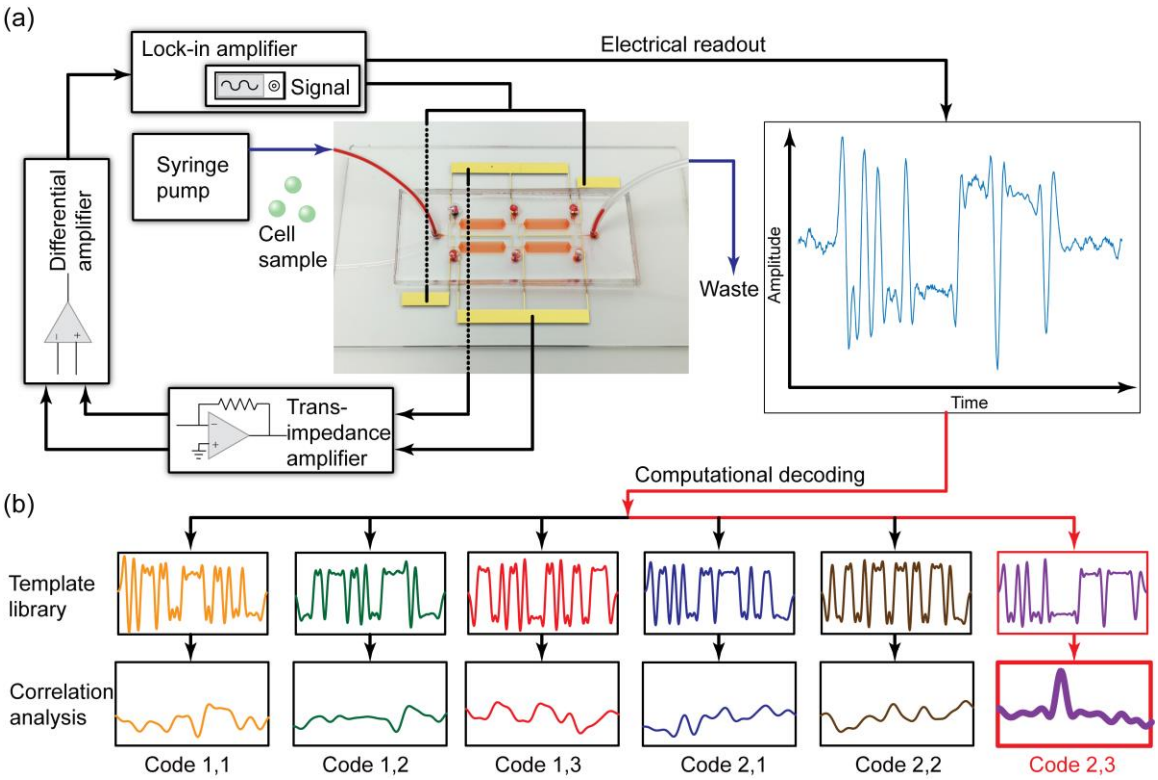

Figure 7.6 – The electrical acquisition of the cell capture statistics across the antibody microarray. (a) A schematic of the experimental setup used for the sample delivery and electrical measurements. Cells are driven through the device at a constant flow rate with a syringe pump. The electrical sensor network is excited using a sine wave generated from the lock-in amplifier, and the resulting current signal is first converted to voltage signals using transimpedance amplifiers, then subtracted from each other by a differential amplifier and the signal amplitude is measured using a lock-in amplifier. (b) The decoding process to identify individual sensor signals in the device output signal. The output signal is correlated with a template library consisting of signature waveforms corresponding to each and every coded sensor in the network using a custom-built algorithm. A correlation peak is used to identify the matching template and the specific sensor that detected the cell. The specific case in the figure demonstrates the decoding of a signal produced by the sensor with the Code 2,3.

templates specific to both the sample and the device, thereby increasing accuracy. The templates were then used to process all sensor data by correlating the output signal with the template library. Because the code signals were specifically designed to be mutually orthogonal, we could not only classify sensor signals robustly with minimal crosstalk but also resolve signal interferences through an iterative process called successive interference

cancellation.[116,153] At the end of this decoding process, the original output waveform was decomposed into data from individual sensors, which was then used to calculate cell capture statistics across the whole device. Specifically, the number of captured cells in each chamber was obtained, by subtracting the exit node cell count from the entry node cell count. (Tables 7.1 and 7.2).

Table 7.1 – The Gold codes used in the multiplexed sensor network for the antibody microarray and the individual cell count from each coded Coulter sensor

Coded sensor	Code	Cell count
Code 1,1	10101110110001111100110100100000	c_{11}
Code 1,2	00011011110110100011111100100000	c_{12}
Code 1,3	01110010110100001101001100111110	c_{13}
Code 2,1	10110101000111011111001001100000	c_{21}
Code 2,2	01001100101110011101100111010000	c_{22}
Code 2,3	10010100010000000111110111111101	c_{23}

7.2 Optimization of the cell capture parameters

7.2.1 Optimization of the antibody concentration

Cells expressing the target antigens and yet not captured by our device lead to false negative results. Therefore, to maximize cell capture efficiency, we first optimized the amount of antibody to coat the microfluidic cell capture chambers. To measure the antibody coverage on the surface, we employed fluorophore-conjugated antibodies and imaged the functionalized device with fluorescence microscopy. Cell capture chambers were first functionalized with FITC anti-CD45 antibody at concentrations ranging from 0.25 μg mL^{-1} to 50 μg mL^{-1} using the immobilization protocol. We observed higher fluorescence emission with increasing antibody concentration, and the differential emission between antibody concentrations was especially apparent on micropillar surfaces,

where deposited fluorophore-conjugated antibody formed high contrast annular patterns around the cross-sections of the pillars (Figure 7.7). Quantitative measurements of mean fluorescence intensities for different concentrations showed a drastic increase in surface antibody concentration until 10 μg mL^{-1} and the changes in fluorescence beyond 25 μg mL^{-1} were not notable, indicating surface saturation (Figure 7.7). Based on these results, we selected 25 μg mL^{-1} as the optimum incubation concentration to ensure complete coverage of the device surface with capture antibodies.

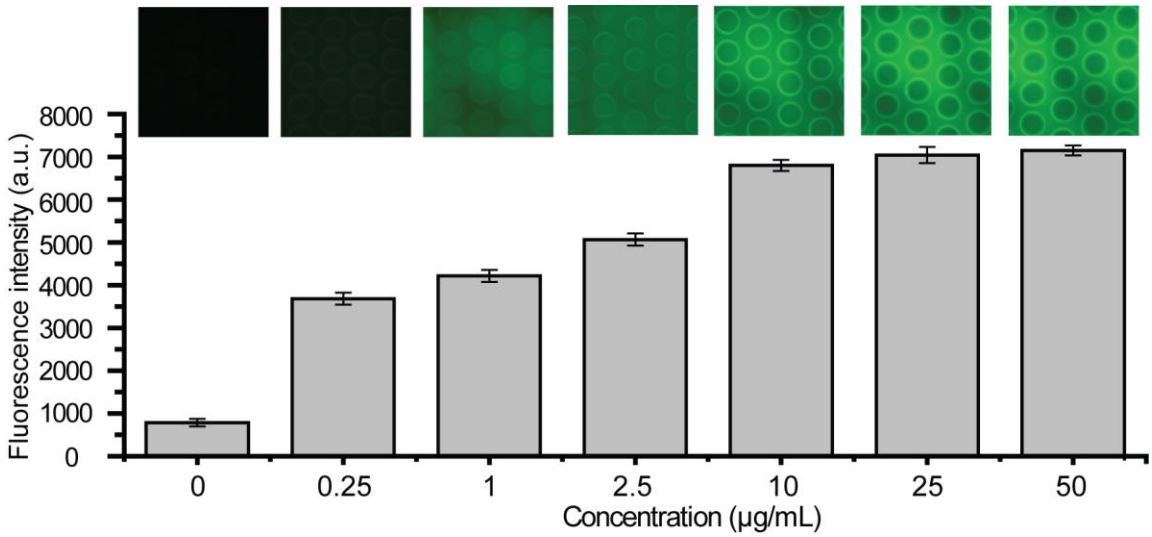

Figure 7.7 – Optimization of the capture antibody amount immobilized on the device surface. Devices were functionalized with FITC-conjugated anti-CD45 antibody at concentrations ranging from 0 to 50 μg mL^{-1}. The amount of the immobilized antibody at different concentrations was measured from the fluorescence intensity.

7.2.2 Optimization of the sample flow speed

We also investigated the sample flow speed as a parameter to optimize the cell capture rate in our microfluidic device. The flow speed is an important factor in our assay because the cell immunocapture is a process with a binary outcome that depends on both the number of matching antibody-antigen pairs and the antibody-antigen interaction time,

controlled by the sample flow speed [177,178]. To optimize sample flow speed, we first functionalized the cell capture chambers with anti-CD45 antibody and tested the leukocyte capture performance under different flow rates. To quantify the effect of sample flow speed on the capture rate, we drove leukocytes through the microfluidic device at flow speeds ranging from 40 μm s^{-1} to 400 μm s^{-1} using a syringe pump and measured the fraction of captured cells in the microfluidic chamber. As anticipated, the cell capture rate showed a strong dependence on the flow speed decreasing from ~99% for flow rates 80 μm s^{-1} to ~64% at 400 μm s^{-1} (Figure 7.8). Based on minimal observed differences between cell capture rates below 80 μm s^{-1} and considering potential problems at low flow rates such as sedimentation and non-specific adhesion induced artifacts, we chose 80 μm s^{-1} as the optimal sample flow speed for our assay. Similar optimization experiments have also been performed for the other antibodies used in this work, and we found that at 80 μm s^{-1}, all produced >96% capture rates. It should also be noted that the sample flow speed could be used as a physical gating mechanism since the required number of the antibody-antigen pairs in the cell adhesion process is related to the interface contact time [178]. For example, a higher cell velocity would increase the minimum number of the antibody-antigen pairs required for cell capture, which would be analogous to a lower gate size in the post-analysis of flow cytometry data. Likewise, a lower flow velocity can be used to compensate for a low affinity antibody-antigen pair and enhance the assay sensitivity.

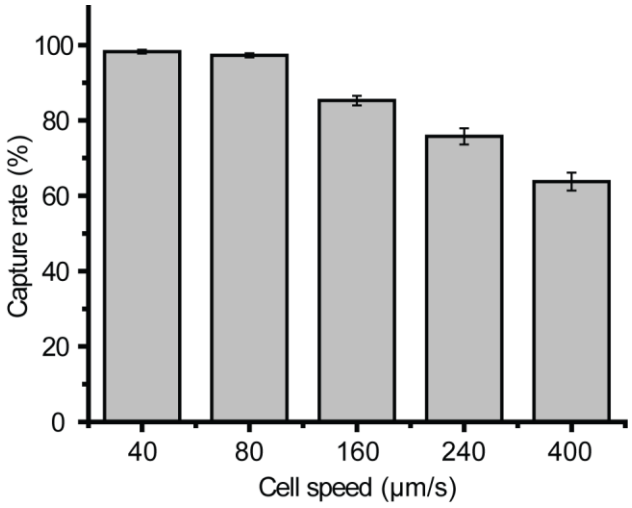

Figure 7.8 – Optimization of the sample flow speed. Measured leukocyte capture rates in devices functionalized with anti-CD45 as a function of sample flow rates ranging from 40 µm s^{-1} to 400 µm s^{-1}.

7.2.3 Optimization of the non-specific binding

To ensure specific capture of target cells in microfluidic capture chambers, we minimized non-specific cell adhesion by blocking the functionalized device surface with BSA. To determine the optimum BSA amount, we first functionalized devices at the predetermined optimum antibody concentration (25 µg mL^{-1}) and treated them with BSA solutions with concentrations ranging from 0 to 10% (w/v) for 1 hour. After washing the devices with PBS, we drove leukocytes at the optimum flow speed (80 µm s^{-1}) and measured the non-specific cell capture rate. In these measurements, we specifically chose the anti-CD115 as the capture antibody since the CD115 is expressed only by <10% of leukocytes (i.e., some monocytes) [179], making most leukocytes potential targets for the non-specific capture. To distinguish specific monocyte capture from non-specific cell capture, captured leukocytes were post-labeled with Alexa Fluor 488 anti-CD115 and counted with fluorescence microscopy. With increasing BSA concentration, a non-specific cell capture rate decreased from >70% for non-blocked devices to ~2% for devices treated

with a 10% BSA solution (Figure 7.9). Finally, we confirmed that specific cell capture was not confounded by blocking, because the capture rate of $CD115^{pos}$ leukocytes remained virtually constant across different BSA concentrations (Figure 7.9, red line). Based on these results, we selected the 10% BSA solution as the optimal blocking buffer for our assay.

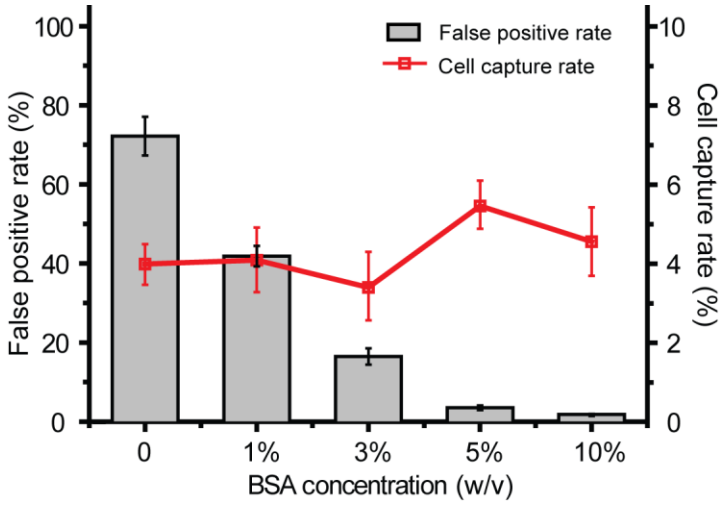

Figure 7.9 – Optimization of the BSA concentration for minimizing non-specific cell capture. Non-specific cell capture rate was measured at BSA concentrations ranging from 0 to 10%.

7.2.4 Immobilization of the antibodies

Following the optimization of surface chemistry for efficient and specific cell capture, we investigated the selective immobilization of capture antibodies to designated cell capture chambers. Specifically, we attempted to coat each of the four cell capture chambers with a different antibody via auxiliary functionalization ports based on the protocol described previously and inspected the resultant spatial arrangement of antibodies across the device with microscopy. To distinguish between different antibodies on the device, we specifically used antibodies conjugated with different-colored fluorophores (Alexa Fluor 594, Alexa Fluor 488, Brilliant Violet 421, and Alexa Fluor 647). Fluorescence images of

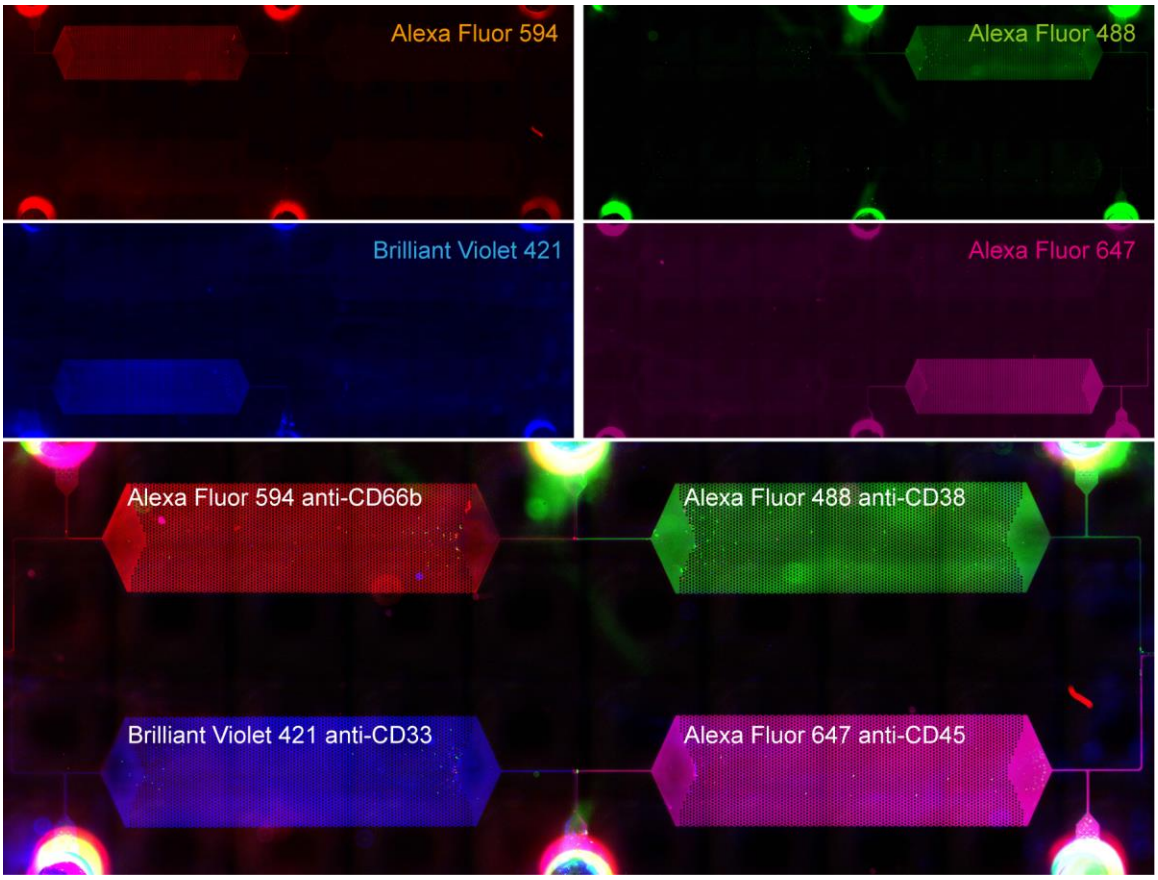

Figure 7.10 – Specific functionalization of microfluidic chambers with four different capture antibodies. (top) Single-channel fluorescence images show the exclusive immobilization of capture antibodies, each labeled with a different fluorophore, in the corresponding cell capture chambers. Each capture chamber is uniformly coated, and no crosstalk can be observed between cell capture chambers. (bottom) A four-channel fluorescence image of the whole device shows the successful functionalization of cell capture chambers. The boundaries between different antibodies are visible along the microfluidic channels that connect cell capture chambers. (Error bars represent standard deviation.)

the functionalized device showed that (1) each cell capture chamber was exclusively coated with the intended capture antibody (Figure 7.10, top), (2) there was no crosstalk between the different chambers as evidenced by distinct boundaries between different immobilized antibodies in the microfluidic channels that connect cell capture chambers (Figure 7.10, bottom), and (3) the antibody coverage was uniform throughout all cell capture chambers. It should also be noted that antibodies immobilized external to the cell capture chambers

do not constitute a problem for our assay since (1) cells flow much faster (40 ×) in microfluidic channels preventing them from being captured on electrodes and (2) any cell trapped at the inlet or outlet reservoirs due to slower flow remain outside of the electrical detection nodes and therefore are not counted.

7.3 Immunophenotyping of tumor cell mixtures

For controlled experiments to validate our assay, we employed human cancer cell lines with differing antigen expression. We cultured three breast cancer cell lines (MCF7, SK-BR-3, and MDA-MB-231) and selectively functionalized cell capture chambers with two different antibodies (anti-EpCAM and anti-CD49f antibodies) specifically chosen to target antigens that are differentially expressed by those breast cancer cell lines: MCF7: $EpCAM^{pos}CD49f^{neg}$, SK-BR-3: $EpCAM^{pos}CD49f^{pos}$, MDA-MB-231: $EpCAM^{low/neg}CD49f^{pos}$ with a secondary $EpCAM^{low/neg}CD49f^{neg}$ immunophenotype [180]. To distinguish these immunophenotypes, we arranged the anti-EpCAM and anti-CD49f antibodies in cell capture chambers as a 2 × 2 checkerboard pattern (Figure 7.11), which enabled us to screen cells for all possible combinations of EpCAM and CD49f expressions. Based on the individual cell counts from the coded electrical sensors on the microfluidic device (Table 7.1), we were able to calculate the fraction of cells captured in each cell capture chamber (Table 7.2) and use the measured cell capture statistics to calculate the prevalence of each combinatorial immunophenotype (Table 7.3) in the sample.

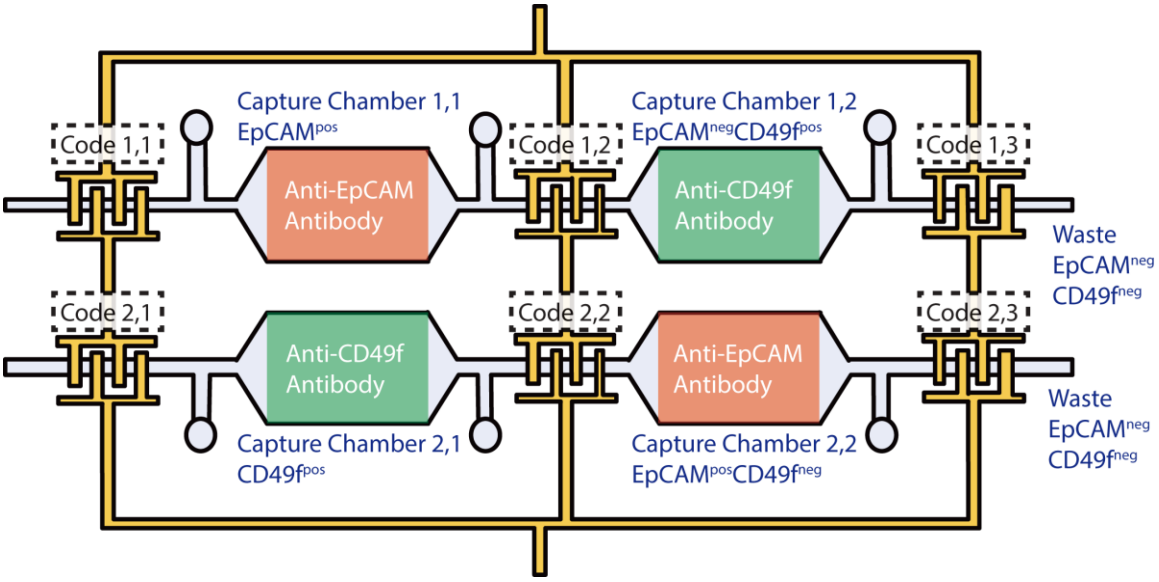

Figure 7.11 – A schematic showing the specific antibody arrangement in the designed microarray. Anti-EpCAM and anti-CD49f antibodies are immobilized in chambers with a checkerboard pattern to fractionate mixtures of MCF7 ($EpCAM^{pos}CD49f^{neg}$), SK-BR-3 ($EpCAM^{pos}CD49f^{pos}$), and MDA-MB-231 ($EpCAM^{low/neg}CD49f^{pos}$) and dual-negative ($EpCAM^{neg}CD49f^{neg}$) cells, which are discharged from the waste outlet.

Table 7.2 – The calculation of the fraction of cells captured in each chamber and non-captured cells discharged into the waste from electrical data

Chamber	Immunophenotype	Fraction
Chamber 1,1	$EpCAM^{pos}$	$p_{11}=(c_{11}-c_{12})/c_{11}$
Chamber 1,2	$EpCAM^{neg}CD49f^{pos}$	$p_{12}=(c_{12}-c_{13})/c_{11}$
Outlet 1	$EpCAM^{neg}CD49f^{neg}$	$p_{1end}=c_{13}/c_{11}$
Chamber 2,1	$CD49f^{pos}$	$p_{21}=(c_{21}-c_{22})/c_{21}$
Chamber 2,2	$CD49f^{neg}EpCAM^{pos}$	$p_{22}=(c_{22}-c_{23})/c_{21}$
Outlet 2	$CD49f^{neg}EpCAM^{neg}$	$p_{2end}=c_{23}/c_{21}$

Table 7.3 – The calculation of the target subpopulation fractions in the cell mixture from the electrical data

Combinatorial immunophenotype	Fraction
$EpCAM^{pos}CD49f^{pos}$	$1-p_{12}-p_{22}-(p_{1end}+p_{2end})/2$
$EpCAM^{pos}CD49f^{neg}$	p_{22}
$EpCAM^{neg}CD49f^{pos}$	p_{12}
$EpCAM^{neg}CD49f^{neg}$	$(p_{1end}+p_{2end})/2$

To test our assay's performance in identifying subpopulations with different antigen expressions, we processed suspensions of MCF7, SK-BR-3, and MDA-MB-231 cancer cells mixed at varying ratios as heterogenous control samples at a flow rate of 80 μm s^{-1}. Our electronic results on the immunophenotype composition of different cell mixtures were consistently in good agreement with the designed mix ratios (Figure 7.12). The differences were mainly due to co-expression of the same immunophenotype by two different cancer cell lines, e.g., MDA-MB-231 cells also express EpCAM, at a low concentration, and were counted in the $EpCAM^{pos}CD49f^{pos}$ immunophenotype that was interpreted as SK-BR-3. Nevertheless, this is not a fundamental problem as measurements can be computationally corrected to accommodate crosstalk between immunophenotypes based on projected antigen co-expression rates of target cell subtypes in a given population.

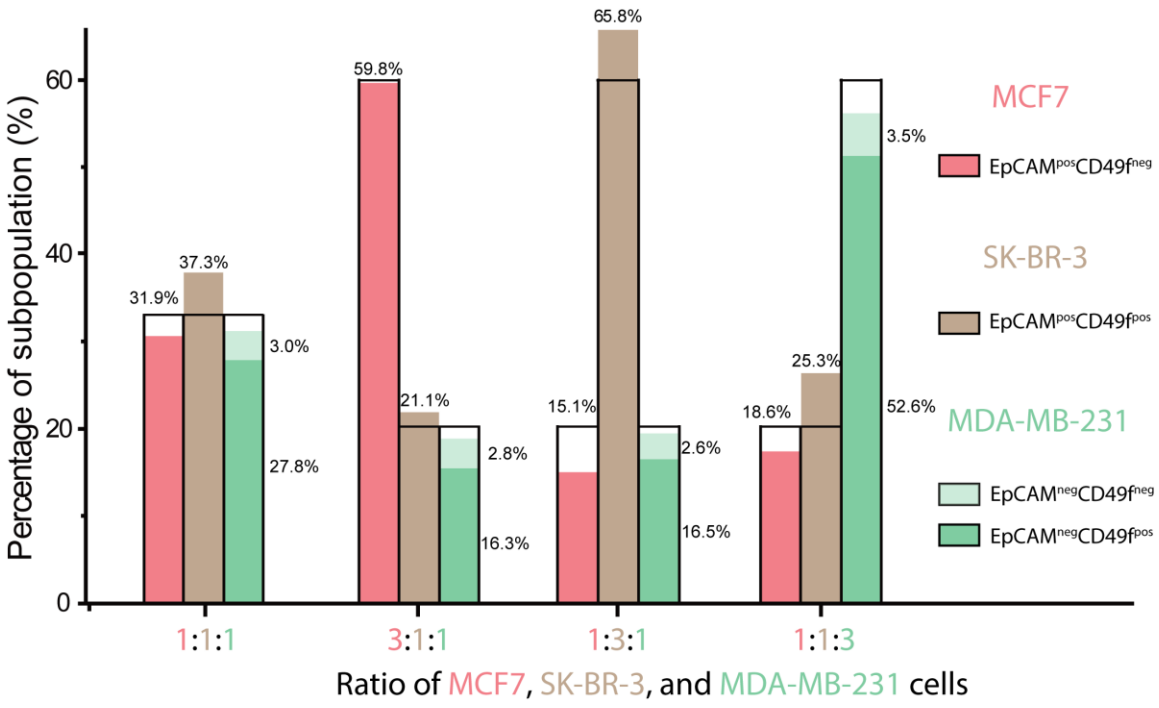

Figure 7.12 – Comparison of the measured frequency (colored bar) and the mix ratios (overlaid unshaded bar) of different cancer cell lines in control samples. Four control samples were prepared by mixing MCF7, SK-BR-3, and MDA-MB-231 cancer cell lines at ratios of 1:1:1, 3:1:1, 1:3:1, and 1:1:3.

To independently validate cell immunophenotype discrimination by our assay, we characterized the expression of tumor cells captured on the chip via fluorescence microscopy after post-labeling them against both EpCAM and CD49f. From the dual-channel fluorescence images of stained cells, differences in the composition of cells captured in different chambers could clearly be observed: Anterior cell capture chambers in the microfluidic cascade (i.e., chambers 1,1 and 2,1) received the full sample composition and captured cells that expressed the target antigen (i.e., EpCAM for chamber 1,1 (Figure 7.13(i)) and CD49f for chamber 2,1 (Figure 7.13(iii))). In both anterior cell capture chambers, dual-expressor cells could also be observed as the expression of another antigen did not interfere with the cell immunocapture. In contrast, cells captured in posterior chambers contained only single-expressor cells with the antigen targeted by the capture antibody immobilized in the corresponding capture chamber (CD49f for chamber 1,2 (Figure 7.13(ii)) and EpCAM for chamber 2,2 (Figure 7.13(iv))). The lack of dual-expressor cells in the posterior chambers is due to the fact that posterior cell capture chambers received only a portion of the sample that was already depleted of cells expressing the antigen targeted by the anterior chamber.

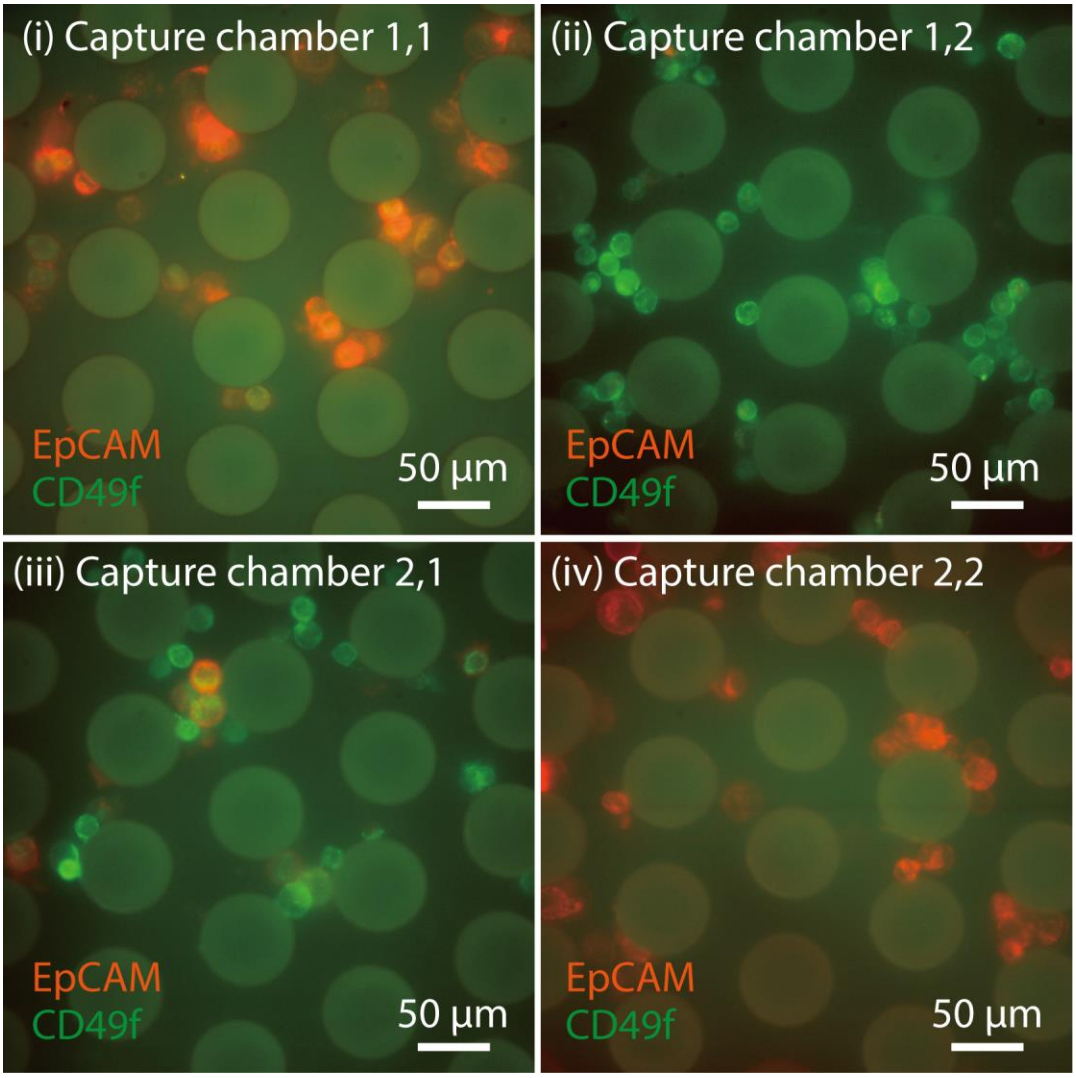

Figure 7.13 – Representative two-channel fluorescence images of the captured cells post-labeled with a cocktail of Alexa Fluor 594 anti-EpCAM and Alexa Fluor 488 anti-CD49f antibodies in (i) chamber 1,1 ($EpCAM^{pos}$), (ii) chamber 1,2 ($EpCAM^{neg}CD49f^{pos}$), (iii) chamber 2,1 ($CD49f^{pos}$), and (iv) chamber 2,2 ($CD49f^{neg}EpCAM^{pos}$).

As a control, we labeled cells in the unprocessed (input) mixture and also in the waste (output) with the same fluorophore-conjugated antibodies and observed cells in the unprocessed sample expressed all possible immunophenotypes (Figure 7.14, left), while cells in the waste were all dual-negative expressing neither EpCAM nor CD49f (Figure 7.14, right). Taken together, these results demonstrated a successful fractionation of a

heterogeneous sample into different cell capture chambers based on the cell immunophenotype and validated the platform for combinatorial phenotyping of cell populations.

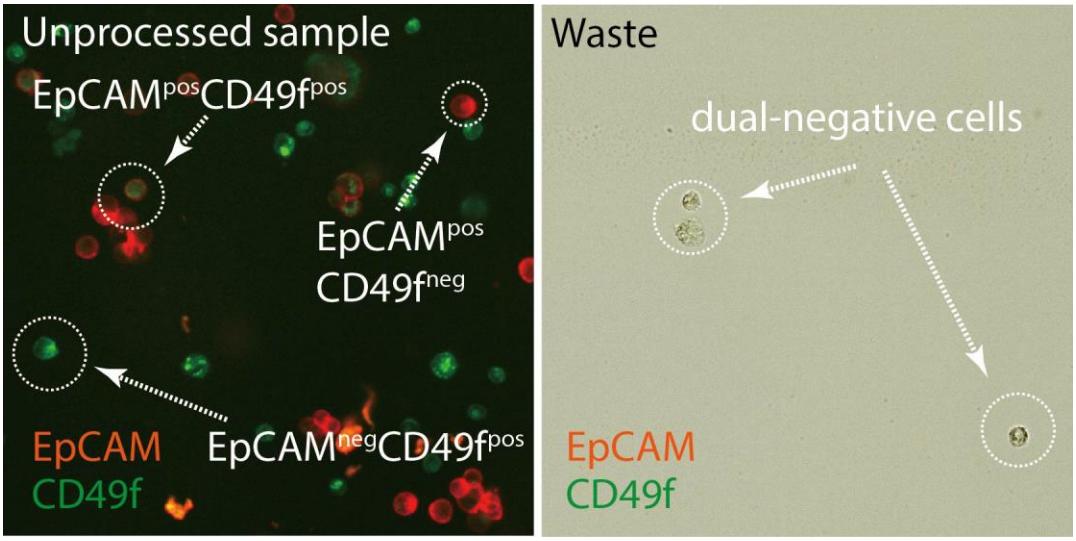

Figure 7.14 – The fluorescence image of the unprocessed sample and waste. (Left) The fluorescence image of the unprocessed sample stained with the same fluorophore-conjugated antibodies shows all combinatorial immunophenotypes ($EpCAM^{pos}CD49f^{pos}$, $EpCAM^{pos}CD49f^{neg}$, and $EpCAM^{low/neg}CD49f^{pos}$). (right) A fluorescence image of cells ($EpCAM^{neg}CD49f^{neg}$) found in the waste collected from our device. Post-labeling of cells against the two antibodies produced no fluorescence signal indicating the dual-negative immunophenotype of these cells.

7.4 Immunophenotyping of leukocytes

To demonstrate the relevance of our assay for point-of-care testing, we designed an assay to measure the composition of leukocytes in a blood sample. To distinguish different leukocyte subpopulations, we functionalized our device with four different antibodies (anti-CD66b, anti-CD38, anti-CD33, anti-CD45) against antigens differentially expressed among leukocytes. Importantly, the spatial arrangement of antibodies on the device (Figure 7.15) were specifically designed to distinguish different leukocyte subtypes with distinct immunophenotypes, namely granulocytes, lymphocytes, and monocytes: In one of the

microfluidic paths, antibodies were immobilized in a sequence, where the anti-CD66 was followed by the anti-CD38. Under this arrangement, cells captured in the anterior chamber (i.e., $CD66b^{pos}$ immunophenotype) were considered as granulocytes [181], while cells in the posterior chamber (i.e., $CD66b^{neg}CD38^{pos}$ immunophenotype) were considered as lymphocytes [182,183]. In the other microfluidic path, the anti-CD33 was followed by the anti-CD45. Because CD33 is a surface marker used for identifying monocytes, that is also expressed by granulocytes [184,185], we interpreted cells captured in the anterior chamber (i.e., $CD33^{pos}$ immunophenotype) as a mixed population of monocytes and granulocytes, while cells in the posterior chamber (i.e., $CD33^{neg}CD45^{pos}$ immunophenotype) were considered as granulocytes and lymphocytes. By processing electrical sensor data, we could determine the capture statistics for each immunophenotype (Table 7.4) and calculate the frequency of each leukocyte subpopulation (Table 7.5) in the blood sample.

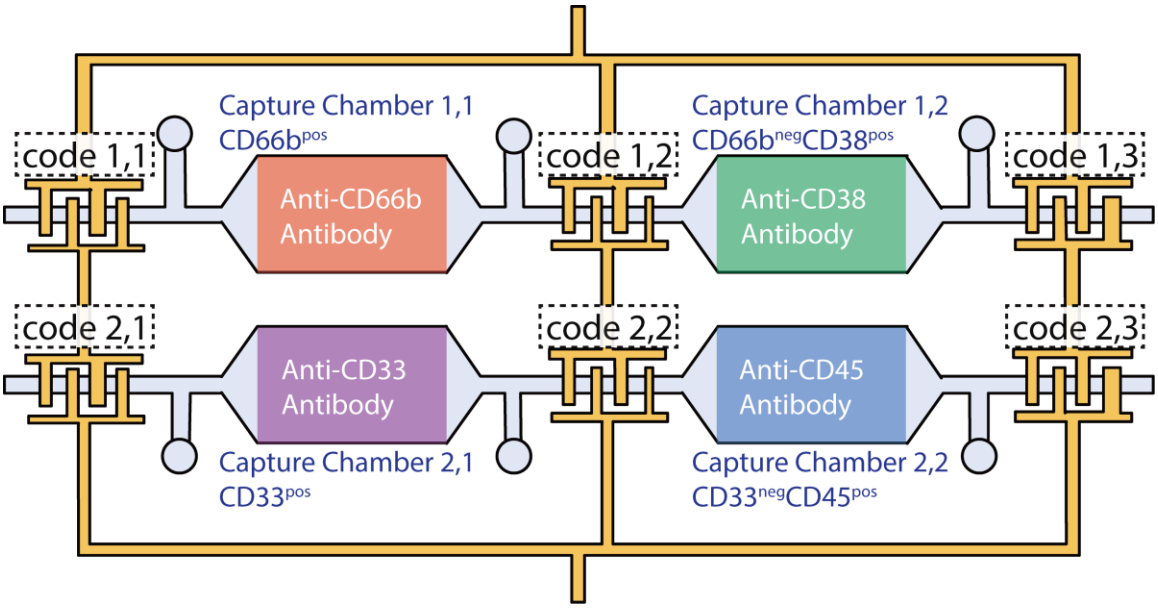

Figure 7.15 – A schematic showing the specific antibody arrangement in the microarray. Microfluidic cell capture chambers were functionalized with anti-CD66b, anti-CD38, anti-CD33, and anti-CD45 antibodies to fractionate leukocytes into granulocytes, lymphocytes, and monocytes.

Table 7.4 – The immunophenotype, calculation of the fractions, and the types of cells captured in each chamber and non-captured cells discharged into the waste

Chamber	Immunophenotype	Fraction	Cell type
Chamber 1,1	$CD66b^{pos}$	$p_{11}=(c_{11}-c_{12})/c_{11}$	Granulocytes
Chamber 1,2	$CD66b^{neg}CD38^{pos}$	$p_{12}=(c_{12}-c_{13})/c_{11}$	Lymphocytes
Outlet 1	$CD66b^{neg}CD38^{neg}$	$p_{1end}=c_{13}/c_{11}$	
Chamber 2,1	$CD33^{pos}$	$p_{21}=(c_{21}-c_{22})/c_{21}$	Monocytes + Granulocytes
Chamber 2,2	$CD33^{neg}CD45^{pos}$	$p_{22}=(c_{22}-c_{23})/c_{21}$	Lymphocytes + Granulocytes
Outlet 2	$CD33^{neg}CD45^{neg}$	$p_{2end}=c_{23}/c_{21}$	Other leukocytes

Table 7.5 – The parametric calculation of the fraction of each leukocyte subtype in the leukocyte suspension

Leukocyte Subtype	Fraction
Granulocytes	p_{11}
Lymphocytes	p_{12}
Monocytes	$1-p_{11}-p_{12}-p_{2end}$

We applied our technology on blood samples collected from consenting donors according to the Georgia Tech Institutional Review Board (IRB) protocol and validated our results by fluorescently labeling and imaging of leukocytes captured on our device. Following the lysis of erythrocytes, >4000 leukocytes were processed using our assay in 10-15 minutes at a flow rate of 80 μm s^{-1}. Following the completion of the assay, cells were immunolabeled on the chip with a cocktail of Alexa Fluor 594 anti-CD66b, Alexa Fluor 488 anti-CD38, Alexa Fluor 647 anti-CD33, and Brilliant Violet 421 anti-CD45 antibodies and characterized with a fluorescence microscope. Fluorescence measurements confirmed that virtually all captured leukocytes expressed the surface antigen targeted by the corresponding capture chamber (Figure 7.16).

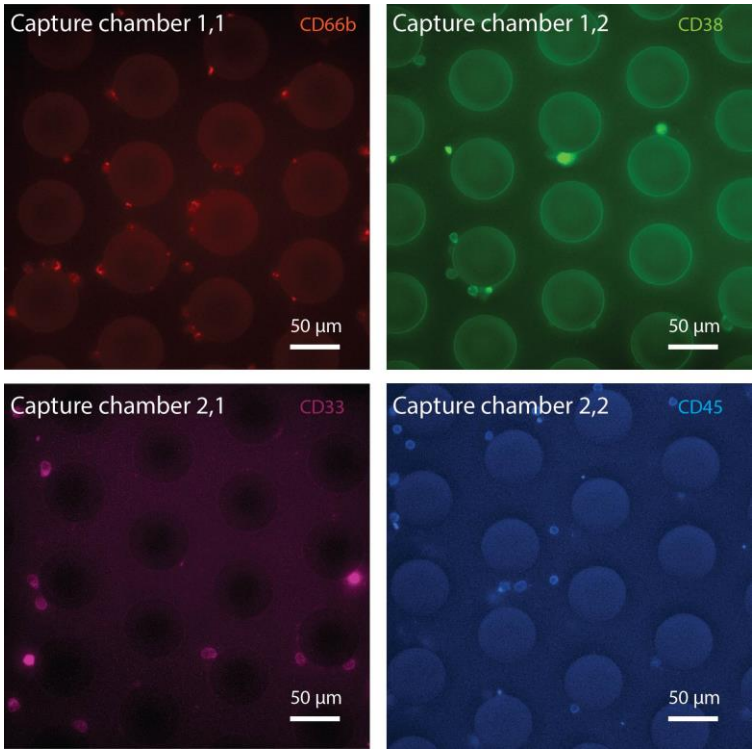

Figure 7.16 – The single-channel fluorescent images showing surface marker expressions on the captured cells in different microfluidic chambers. The images show all captured cells expressing the antigen targeted by the corresponding capture chamber.

By imaging all leukocytes on the chip in different fluorescence channels (Figure 7.17), we measured the frequency of expression for all four antigens in each capture chamber (Figure 7.18). This complete picture of cell composition demonstrated that (1) our microfluidic device was very efficient in capturing target cells, (2) cell population captured in different chambers showed drastic differences in their expression profile, further confirming successful sample fractionation into distinct subpopulations.

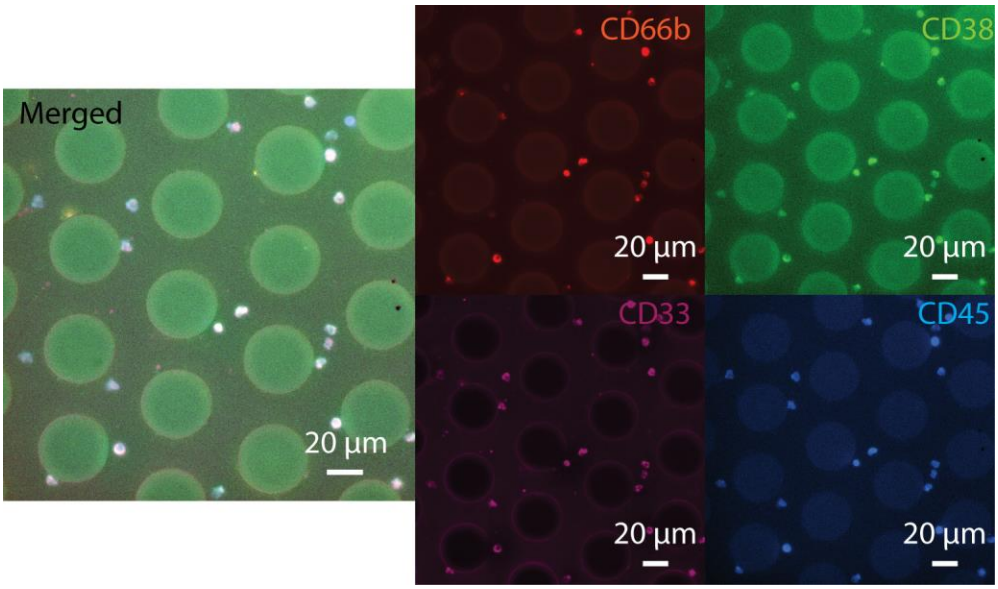

Figure 7.17 – Immunofluorescence characterization of cell populations captured in microfluidic chambers. These representative fluorescence images show a group of leukocytes captured in the microfluidic chamber functionalized with anti-CD33 antibody. The captured cells were post-labeled with a cocktail of Alexa Fluor 594 anti-CD66b, Alexa Fluor 488 anti-CD38, Alexa Fluor 647 anti-CD33, and Brilliant Violet 421 anti-CD45 antibodies. Similar images were also taken in other capture chambers by scanning fluorescence microscopy. Finally, by counting the cells positive in each fluorescence channel, the frequency of different immunophenotypes was calculated for each capture chamber.

To assess the performance of our technique for blood analysis, we benchmarked our results against measurements from established hematology techniques. Matching blood samples were processed with a commercial benchtop hematology analyzer (CELL-DYN Ruby, Abbott) to obtain a complete blood count and also with a flow cytometer (BD LSRFortessa). For the flow cytometry, the leukocyte suspension was fluorescently labeled against the same set of antigens employed in our assay, and the results were gated based on preconfigured values for leukocyte classification to calculate the frequency of each subpopulation (Figures 7.19, 7.20).

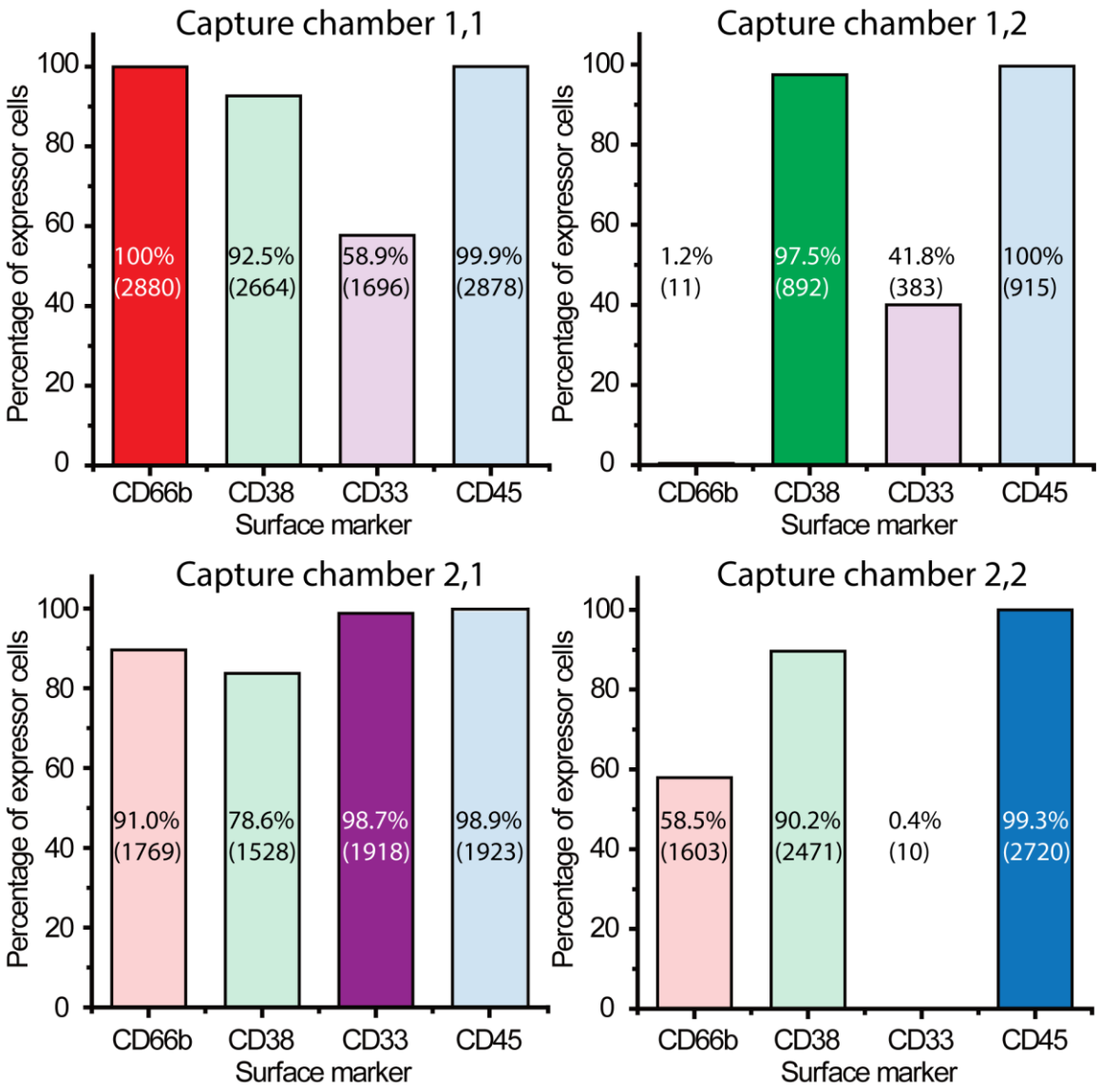

Figure 7.18 – Immuno-expression of cells captured in each microfluidic chamber. All of the captured cells were labeled with fluorophore-conjugated antibodies against all four antigens, and the frequency of each immunophenotype was calculated for each cell capture chamber. Each bar in the plots shows the measured frequency and the actual cell count for the immunophenotype in the corresponding capture chamber.

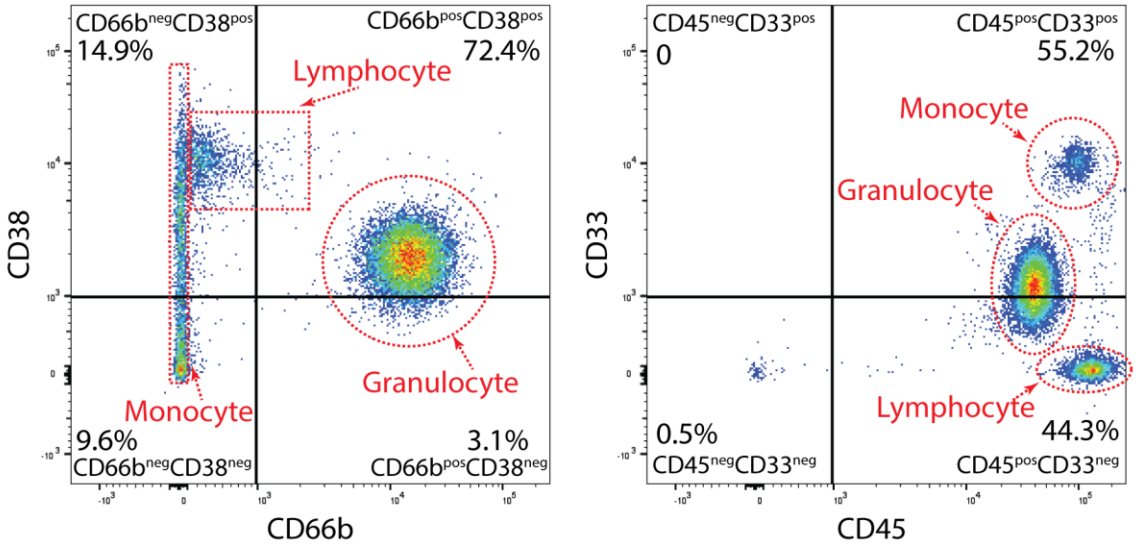

Figure 7.19 – Classification of leukocyte subpopulations with flow cytometry. The density scatter plots show frequencies of the subpopulations for each immunophenotype. The gates in the plots were set based on the prior tests with fluorophore-labeled calibration beads. The measurements were grouped as granulocyte, lymphocyte, or monocyte based on the cell hierarchy population analysis from the FSC-SSC plot (Figure 6.20) for better illustration.

Considering the differences between the complete blood count and flow cytometry results, our results are in agreement with both techniques (Figure 7.21); the percentage of $CD66b^{pos}$ cells (granulocytes) measured by our device, hematology analyzer, and flow cytometer were 66.0%, 64.5%, and 75.5%, respectively; the percentage of $CD66b^{neg}CD38^{pos}$ cells (monocytes) was measured as 21.8% with the antibody microarray, 28.6% with the hematology analyzer, and 14.9% with the flow cytometer; the frequency of the $CD33^{pos}$ cells was determined by our device to be 43.0% versus 55.2% from the flow cytometer. Our repeated measurements on blood samples collected from different donors showed that our device could accurately identify leukocyte subpopulations with an average of <6% difference from complete blood count and flow cytometry results (Figure 7.22).

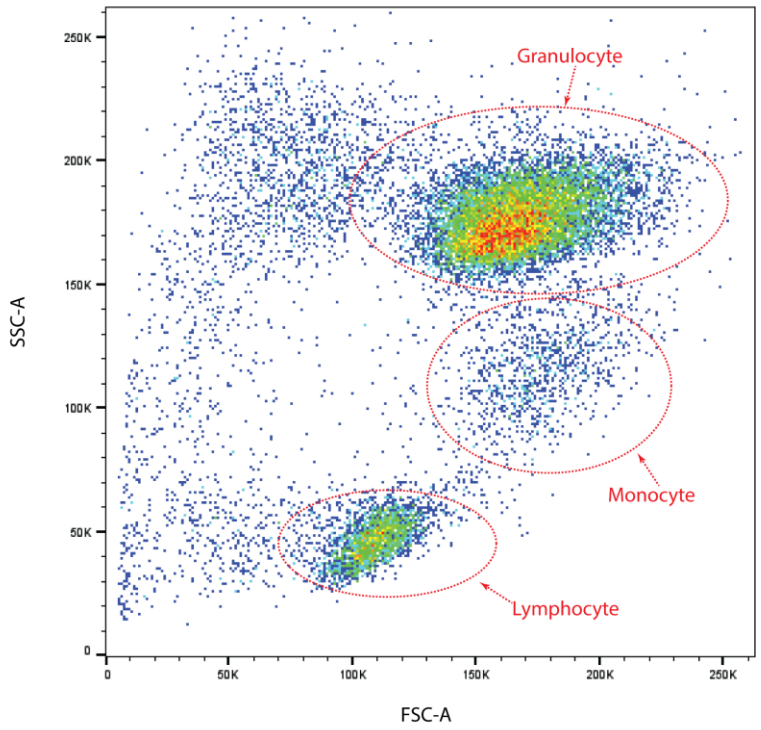

Figure 7.20 – The FSC-SSC scatter plot obtained from the flow cytometry analysis of the leukocytes used in our study. Gates we used for designating leukocyte subpopulations are shown on the plot.

Observed differences between these measurements should be expected due to several factors: (1) transduction modalities of the three methods are fundamentally different, leading to entirely different discrimination criteria to classify different subpopulations, (2) artifacts are unavoidably introduced during different sample preparation steps required for different techniques, e.g., erythrocyte residues in the lysed samples or cell loss during centrifugation processes.

The electronic antibody microarray, introduced in this work, is a viable immunophenotyping assay with several advantages over existing methods for the analysis of cell populations. First, our technique is label-free. In a typical flow cytometry assay, the samples have to be pre-labeled with fluorophore-conjugated antibodies to transduce

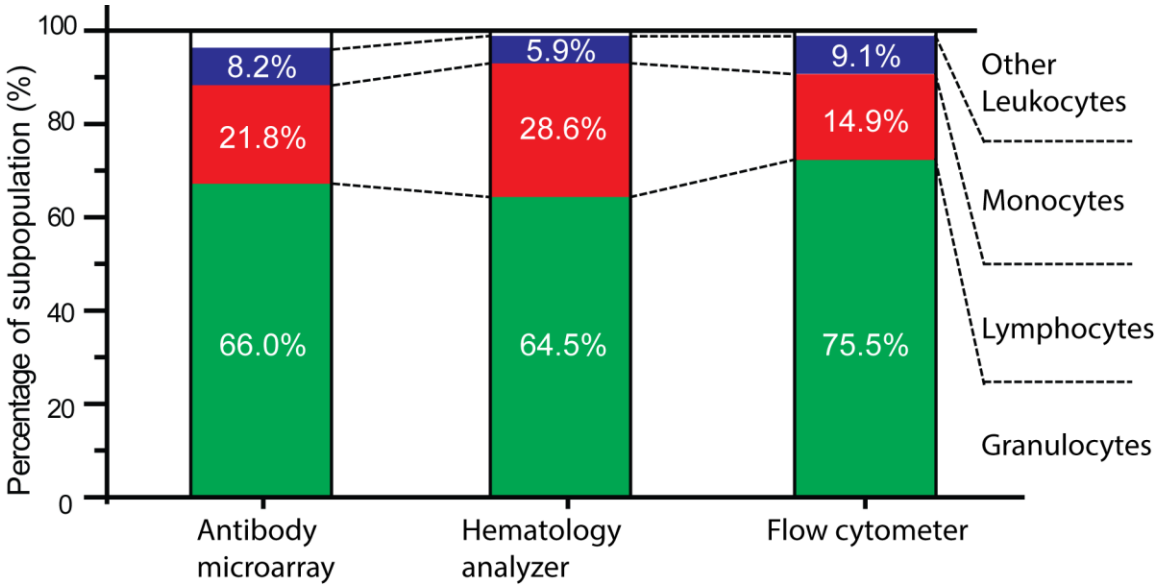

Figure 7.21 – The frequency of leukocyte subpopulations measured by our device, a commercial hematology analyzer, and a commercial flow cytometer in matched samples.

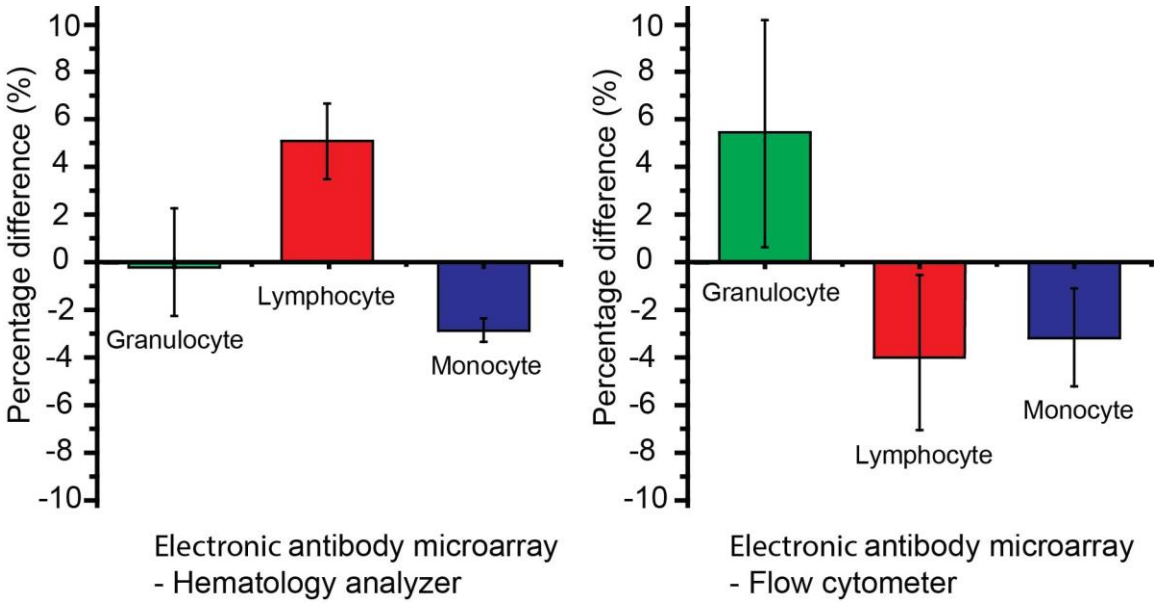

Figure 7.22 – The average difference in the measurement of leukocyte subpopulations using our device versus the hematology analyzer (left), and the flow cytometer (right). Error bars represent standard deviation

chemical information into optical signals [20,186], while unlabeled cells can directly be introduced into our assay for analysis. The label-free operation not only makes our

approach well suited for settings where sample preparation is not feasible but also reduces the total assay time, thereby increasing its practical utility. Second, our assay directly reports immunophenotyping results as electrical data. Compared to optical systems, which require both optical and electrical components, our platform can be coupled with an electronic circuit that can both drive and read the on-chip sensors, reducing both the system complexity and size. Compared to conventional electrical cytometry that measures the physical properties of cells (e.g., size [187] and electrical parameters [188]), our technique probes well-established and more specific biochemical markers on the cell membrane, which cannot be probed through electrical means otherwise. On-chip multiplexing of electrical data enables an efficient acquisition, storage, transmission, and analysis of the assay results. In fact, computational analysis of the assay results could be performed in real-time (~1000 cells s^{-1}) using deep learning algorithms [189]. Overall, our platform operates as simple as a Coulter counter supported with more advanced software to interpret its results. Third, our assay is both flexible and scalable to screen for a specific and larger number of antigen combinations, respectively. Flow cytometers are limited in the number of antigens that can be probed simultaneously due to spectral crosstalk in the detectors [20,186]. In contrast, our platform can add more capture chambers and sensors without affecting the performance of existing sensors [153]. Compared to conventional antibody microarrays [190,191], on the other hand, our assay can identify subpopulations expressing different antigen combinations by sequentially subjecting the cells to different antibodies. Taken together, label-free immunophenotyping of cell populations against multiple targets on an electronic disposable chip presents an opportunity in global health and telemedicine applications for cell-based diagnostics and health monitoring.

7.5 Conclusions

We introduced a microfluidic antibody microarray that can electrically report the frequency of target cell subpopulations in a sample. In our device, functionalized microfluidic chambers cascaded to produce different antibody combinations fractionate samples into its components, and an integrated sensor network transduces cell capture statistics into electrical data for label-free immunophenotyping. Remarkably, the application of our technique for the analysis of leukocyte subpopulations in blood samples produced comparable results with significantly more expensive and sophisticated commercial systems, both validating the assay accuracy and demonstrating its potential utility. All in all, we believe the ability to electrically screen cell immunophenotypes on a disposable chip that can be scaled and tuned for specific cell subsets could be transformative in cell-based diagnostics at the point-of-care and resource-limited scenarios.

CHAPTER 8. CONCLUSIONS AND FUTURE WORK

Immunophenotyping is an important process widely applied in fundamental research and clinical diagnosis. We develop a code-division multiplexed sensor network, called microfluidic CODES which combines Coulter principle with telecommunications theory to spatially track the cells from multiple nodes over a microfluidic device simultaneously from one single electrical readout. We integrate the technology with a microfluidic cell capture chamber array, each modified with antibodies against target antigens to identify cell subpopulations based on their CD markers in a quantitative manner. Our system provides an integrated platform for all-electronic label-free combinatorial immunophenotyping of cell populations, which can be widely applied to the resource-limited point-of-care applications.

8.1 Innovations

In this thesis, we introduce a unique bio-sensor technology, called microfluidic CODES, that can spatially track particles across a microfluidic device. Combining the techniques from traditionally distinct disciplines of telecommunications and microfluidics, the microfluidic CODES is capable of reporting microfluidic manipulation of cells within the device from a single electrical output. Our sensor technology relies on multiplexing an array of micromachined Coulter counters each designed to produce a distinct digital code when a particle is detected. These digital codes are developed using the same principles of CDMA telecommunication networks and can be uniquely recovered through simple mathematical calculations. As microfluidic CODES offers a simple, all-electronic interface for tracking particles on microfluidic devices, it is particularly well suited to create

integrated, low-cost lab-on-a-chip devices for cell- or particle-based assays that are needed for point-of-care tests in resource-limited settings.

To aid the design and analysis of our sensor network, we develop an equivalent circuit model for a network of code-multiplexed Coulter sensors and accurately predict the sensor output based on the microfluidic device geometry and sample properties. In our model, we combine the Foster-Schwan model and conformal mapping to model the cell-electrode interaction in a non-uniform electric field. Our model is then dynamically reconfigured to simulate cell flow over the micromachined surface electrodes. Finally, we solve for the steady-state current flow in these reconfigured versions of our model to construct time waveforms that represent the cell-induced pulse. The model we build will enable the design of code-division multiplexed Coulter sensors optimized to produce desired waveform patterns to ensure reliable and efficient decoding.

We combine our sensor technology with a microfluidic antibody array to convert the chemical information into electrical information. For this purpose, we create a microfluidic device that consists of microfluidic cell capture chambers pre-functionalized with antibodies against target antigens and code-multiplexed Coulter counters placed at strategic nodes across the device to quantify the fraction of cell population captured in functionalized chambers. At both inlet and outlet of each capture chamber, we place sensors with distinct codes, making it possible to count the number of cells from one electrical readout. By reading the cell count from the inlet and outlet counters for each capture chamber, the information about the prevalence of the antigen-positive subpopulation can be obtained. Therefore, our technology will be able to electronically

quantify the frequency of different antibodies in a cell population without any pre-labeling and by processing a signal obtained from a single electrical readout.

To manufacture the device, we also develop new fabrication techniques. For example, to functionalize our device, we develop a new technique to selectively modify individual capture chambers with various antibodies. Through the combinatorial arrangement of antibody sequences along microfluidic paths, our device achieves all-electronic combinatorial immunotyping of cell populations against multiple antigen targets.

8.2 Limitations and future work

In the work, we introduced a microfluidic antibody microarray with a direct electrical readout, based on the Microfluidic CODES sensor technology. Our technology provides an integrated platform for label-free combinatorial immunophenotyping of cell populations; we believe the ability to electrically screen cell immunophenotypes on a disposable chip that can be scaled and tuned for specific cell subsets could be transformative in cell-based diagnostics at the point-of-care and resource-limited scenarios.

From the experiment results, we found that even though the immunophenotyping information of cell populations from the antibody microarray is very close to the result obtained from flow cytometry, the numbers are not exactly the same, this error comes from the inevitable incomplete bindings and non-specific bindings, so the capture efficiency and false negative rate are not the ideal numbers. The error will be exaggerated when the population of the target cells is small, which is a limitation of our technique and needs to be solved in the future.

In flow cytometry, the fluorescent intensity of the cell represents the expression level of the surface antigen on the cell, however, in our current microfluidic antibody microarray, the immunocapture process provides a binary outcome for the surface antigen expression of each cell, which does not have the expression level information. In Section 7.2.2, we have discussed the relation between the flow speed and the number of antibody-antigen pairs needed in the capture process, which indicates that the cells being captured at different flow speeds may have different levels of surface antigen expression. It provides the possibility to apply our technique for surface antigen expression level profiling: by optimizing the dimension of each chamber, we can control the cells flowing at multiple speeds at different locations of the microfluidic device, so that the cells captured express different levels of surface antigens across an antibody microarray. For the next step, the research will continue with exploring the details of the relation between the surface antigen expression level and the flow speed, and adjusting the geometry of the antibody microarray, to make it more adjustable for various clinical immunophenotyping assays.

Also, Microfluidic CODES offers a simple, all-electronic interface to spatially track particles on microfluidic devices, which will potentially be useful in creating integrated low-cost lab-on-a-chip assays. The future work will also involve the combination of the Microfluidic CODES technology with microfluidic sample manipulation to implement all-electronic and fully integrated lab-on-a-chip assays for a variety of applications.

APPENDIX A. CHEMICALS AND MATERIALS LIST

Ammonium chloride (NH_4Cl), potassium bicarbonate ($KHCO_3$), ethylenediaminetetraacetic acid (EDTA) tetrasodium salt, glutaraldehyde, and trichloro(octyl)silane were purchased from Sigma-Aldrich (St. Louis, MO), pure ethanol were purchased from Decon Labs, Inc. (Kings of Prussia, PA), APTES was purchased from Gelest, Inc. (Morrisville, PA), BSA was purchased from Thermo Scientific (Rockford, IL), 1× PBS was purchased from Mediatech (Manassas, VA), all chemicals are analytical grade. All water used for the experiment was deionized (DI) water.

Alexa Fluor 594 anti-CD66b antibody (G10F5 clone), Alexa Fluor 488 anti-CD38 antibody (HIT2 clone), Brilliant Violet 421 anti-CD33 antibody (WM53 clone), Alexa Fluor 647 anti-CD45 antibody (2D1 clone), FITC anti-CD45 antibody (2D1 clone), anti-CD45 antibody (2D1 clone), anti-CD115 antibody (9-4D2-1E4 clone), Alexa Fluor 488 anti-CD115 antibody (9-4D2-1E4 clone), anti-EpCAM antibody (9C4 clone), anti-CD49f antibody (GoH3 clone), Alexa Fluor 594 anti-EpCAM antibody (9C4 clone), Alexa Fluor 488 anti-CD49f antibody (GoH3 clone), anti-CD66b antibody (G10F5 clone), anti-CD38 antibody (HIT2 clone), anti-CD33 antibody (WM53 clone), Alexa Fluor 647 anti-CD33 antibody (WM53 clone), Brilliant Violet 421 anti-CD45 antibody (2D1 clone), phycoerythrin (PE) anti-CD66b antibody (G10F5 clone), Allophycocyanin (APC) anti-CD38 antibody (HIT2 clone), PE anti-CD45 antibody (2D1 clone), and APC anti-CD33 (WM53 clone) antibody were all purchased from Biolegend (San Diego, CA).

4 in. silicon wafers were purchased from UniversityWafer, Inc. (South Boston, MA), SU-8 2000 series photoresist was purchased from MicroChem (Westborough, MA),

NR9-1500PY negative photoresist was purchased from Futurrex, Inc. (Franklin, NJ), PDMS elastomer Sylgard 184 was purchased from Dow Corning (Auburn, MI).

HeyA8 ovarian cancer cell line was obtained from Dr. John F. McDonald of Georgia Institute of Technology, MCF7 (ATCC® HTB-22™), SK-BR-3 (ATCC® HTB-30™), and MDA-MB-231 (ATCC® HTB-26™) breast cancer cell lines were obtained from American Type Culture Collection (ATCC) (Manassas, VA), Roswell Park Memorial Institute (RPMI) 1640 and Dulbecco's Modified Eagle's Medium (DMEM) medium were purchased from Mediatech (Manassas, VA), fetal bovine serum (FBS) was purchased from Seradigm (Radnor, PA), 0.25% trypsin-EDTA was purchased from Life Technologies (Carlsbad, CA).

The blood samples were obtained via venipuncture from healthy donors' bodies using an informed consent process according to the Georgia Tech IRB protocol approved by Georgia Tech IRB.

APPENDIX B. BIOLOGICAL SAMPLE PREPARATION

A.1 Human cancer cell line culture

Four different human cancer cell lines, HeyA8 (ovarian), MCF7 (breast), SK-BR-3 (breast), and MDA-MB-231 (breast), have been used in the work. We cultured the cancer cell line samples in RPMI 1640 (for HeyA8) or DMEM (for MCF7, SK-BR-3, and MDA-MB-231) media supplemented with 10% FBS and maintained under 5% CO2 atmosphere at 37 ℃ in an incubator. Once 80% confluence reached, cells were detached in a 0.25% trypsin solution, pelleted in a centrifuge, resuspended in 1× PBS, and mixed by gentle pipetting to mechanically dissociate potential cell aggregates. Cell concentration for each cell type was measured with a microscope

B.2 Human blood sample processing

1 mL blood samples were collected from healthy donors according to an IRB-approved protocol. To ensure against coagulation, all blood samples were collected in BD EDTA tubes, stored on a rocker at room temperature, and were processed within 6 hours of the blood withdrawal. Prior to processing on our assay, we lysed erythrocytes, which greatly outnumber leukocytes. For our assay, erythrocytes would not only hinder contact between the leukocytes and the functionalized device surface [192], but also increase the background noise in electrical signals and decrease the SNR in electrical measurements. To lyse erythrocytes, we treated the blood sample with ammonium-chloride-potassium (ACK) buffer for ~15 minutes and subsequently centrifuged at 350 xg for 5 minutes. The supernatant was removed, and the cell pellet was rinsed twice with PBS to remove

erythrocyte residues. The cell pellet was then suspended in PBS with gentle pipetting, filtered using 35 µm nylon mesh incorporated Cell Strainer Snap Cap (Falcon, Corning) to create the leukocyte suspension for our assay.

REFERENCES

[1] H. Zola, “Medical applications of leukocyte surface molecules - the CD molecules,” *Mol. Med.*, vol. 12, pp. 312-316, 2006.

[2] E. Dabelsteen, U. Mandel, H. C. Clausen, “Cell surface carbohydrates are markers of differentiation in human oral epithelium, ” *Crit. Rev. Oral Biol. Med.*, vol. 2, pp. 493-507, 1991.

[3] L. Belov, O. de la Vega, C. G. dos Remedios, S. P. Mulligan, R. I. Christopherson, “Immunophenotyping of leukemias using a cluster of differentiation antibody microarray,” *Cancer Res.*, vol. 61, pp. 4483-4489, 2001.

[4] Human Cell Differentiation Molecules (HCDM), http://www.hcdm.org/, March 2020.

[5] S. R. Bennett, F. R. Carbone, F. Karamalis, R. A. Flavell, J. F. A. P. Miller, W. R. Heath, “Help for cytotoxic-T-cell responses is mediated by CD40 signaling,” *Nature*, vol. 393, pp. 478-480, 1998.

[6] N. Baumgrath, In: Methods in Cell Biology Vol. 75 (Eds: Z. Darzynkiewicz, M. Roederer, H. Tanke). Elsevier, New York, NY, USA 2004.

[7] J. S. Han, P. P. Nair, “Flow cytometric identification of cell surface markers on cultured human colonic cell lines using monoclonal antibodies,” *Cancer*, vol. 76, pp. 195-200, 1995.

[8] A. Adan, G. Alizada, Y. Kiraz, Y. Baran, A. Nalbant, “Flow cytometry: basic principles and applications,” *Crit. Rev. Biotechnol.*, vol. 37, pp. 163-176, 2017.

[9] E. Coustan-Smith, J. Sancho, F. G. Behm, M. L. Hancock, B. I. Eazzouk, R. C. Ribeiro, G. K. Rivera, J. E. Rubnitz, J. T. Sandlund, C. H. Pui, D. Campana, “Prognostic importance of measuring early clearance of leukemic cells by flow cytometry in childhood acute lymphoblastic leukemia,” *Blood*, vol. 100, pp. 52-58, 2002.

[10] C. Riccardi, I. Nicoletti, “Analysis of apoptosis by propidium iodide staining and flow cytometry,” *Nat. Protoc.*, vol. 1, 1458, 2006.

[11] M. A. Van Dilla, R. G. Langlois, D. Pinkel, D. Yajko, W. K. Hadley, "Bacterial characterization by flow cytometry," *Science*, vol. 220, pp. 620-622, 1983.

[12] T. Inoue, A. Swain, Y. Nakanishi, D. Sugiyama, "Multicolor analysis of cell surface marker of human leukemia cell lines using flow cytometry," *Anticancer Res.*, vol. 34, pp. 4539-4550, 2014.

[13] O. Civelekoglu, N. Wang, M. Boya, T. Ozkaya-Ahmadov, R. Liu, A. F. Sarioglu, "Electronic profiling of membrane antigen expression via immunomagnetic cell manipulation," *Lab Chip*, vol. 19, pp. 2444-2455, 2019.

[14] S. C. De Rosa, L. A. Herzenberg, L. A. Herzenberg, M. Roederer, "11-color, 13-parameter flow cytometry: identification of human naive T cells by phenotype, function, and T-cell receptor diversity," *Nat. Med.*, vol. 7, pp. 245-248, 2001.

[15] M. Al-Hajj, M. S. Wicha, A. Benito-Hernandez, S. J. Morrison, M. F. Clarke, "Prospective identification of tumorigenic breast cancer cells," *Proc. Natl. Acad. Sci. U. S. A.*, vol. 100, pp. 3983-3988, 2003.

[16] S. J. Ochatt, "Flow cytometry in plant breeding," *Cytometry A*, vol. 73, pp. 581-598, 2008.

[17] C. P. D. Brussaard, D. Marie, G. Bratbak, "Flow cytometric detection of viruses," *J. Virol. Methods*, vol. 85, pp. 175-182, 2000.

[18] J. Agagliate, R. Röttgers, M. S. Twardowski, D. McKee, "Evaluation of a flow cytometry method to determine size and real refractive index distributions in natural , marine particle populations," *Appl. Opt.*, vol. 57, pp. 1705-1716, 2018.

[19] Flow cytometry Core Facility, the University of California, Irvine, http://www.immunology.uci.edu/flow-core, March 2020.

[20] Y. Saeys, S. Van Gassen, B. N. Lambreche, "Computational flow cytometry: helping to make sense of high-dimensional immunology data," *Nat. Rev. Immunol.*, vol. 16, pp. 449-462, 2016.

[21] W. Li, Y. Gao, D. Pappas, "A complementary method to CD4 counting: measurement of CD4+/CD8+ T lymphocyte ratio in a tandem affinity microfluidic system," *Biomed. Microdevices*, vol. 17, 113, 2015.

[22] Y. Zhang, Y. Zhou, W. Li, V. Lyons, A. Johnson, A. Venable, J. Griswold, D. Pappas, "Multiparameter Affinity Microchip for Early Sepsis Diagnosis Based on CD64 and CD69 Expression and Cell Capture," *Anal. Chem.*, vol. 90, pp. 7204-7211, 2018.

[23] M. A. Qasaimeh, Y. C. Wu, S. Bose, A. Menachery, S. Talluri, G. Gonzalez, M. Fulciniti, J. M. Karp, R. H. Prabhalla, R. Karnik, "Isolation of Circulating Plasma Cells in Multiple Myeloma Using CD138 Antibody-Based Capture in a Microfluidic Device," *Sci. Rep.*, vol. 7, 45681, 2017.

[24] Y. Liu, T. Germain, D. Pappas, "Microfluidic antibody arrays for simultaneous cell separation and stimulus," *Anal. Bioanal. Chem.*, vol. 406, pp. 7867-7873, 2014.

[25] N. T. Huang, W. Chen, B. R. Oh, T. T. Cornell, T. P. Shanley, J. Fu, K. Kurabayashi, "An integrated microfluidic platform for in situ cellular cytokine secretion immunophenotyping," *Lab Chip*, vol. 12, pp. 4093-4101, 2012.

[26] C. H. Chu, R. Liu, T. Ozkaya-Ahmadov, M. Boya, B. E. Swain, J. M. Owens, E. Burentugs, M. A. Bilen, J. F. McDonald, A. F. Sarioglu, "Hybrid negative enrichment of circulating tumor cells from whole blood in a 3D-printed monolithic device," *Lab Chip*, vol. 19, pp. 3427-3437, 2019.

[27] D. A. L. Vickers, E. J. Chory, S. K. Murthy, "Separation of two phenotypically similar cell types via a single common marker in microfluidic channels," *Lab Chip*, vol. 12, pp. 3399-3407, 2012.

[28] A. N. Khvastunova, S. A. Kuznetsova, L. S. Al-Radi, A. V. Vylegzhanina, A. O. Zakirova, O. S. Fedyanina, A. V. Filatov, I. A. Vorobjev, F. Ataullakhanov, "Anti-CD antibody microarray for human leukocyte morphology examination allows analyzing rare cell populations and suggesting preliminary diagnosis in leukemia," *Sci. Rep.*, vol. 5, 12573, 2015.

[29] F. Brinkmann, M. Hirtz, A. Haller, T. M. Gorges, M. J. Vellekoop, S. Riethdorf, V. Müller, K. Pantel, H. Fuchs, "A versatile microarray platform for capturing rare cells," *Sci. Rep.*, vol. 5, 15342, 2015.

[30] M. A. Qasaimeh, Y. C. Wu, S. Bose, A. Menachery, S. Talluri, G. Gonzalez, M. Fulciniti, J. M. Karp, R. H. Prabhala, R. Karnik, "Isolation of circulating plasma cells in multiples myeloma using CD138 antibody-based capture in a microfluidic device," *Sci. Rep.*, vol. 7, 45681, 2017.

[31] D. R. Gossett, W. M. Weaver, A. J. Mach, S. C. Hur, H. T. K. Tse, W. Lee, H. Amini, D. Di Carlo, "Label-free cell separation and sorting in microfluidic systems," *Anal. Bioanal. Chem.*, vol. 397, pp. 3249-3267, 2010.

[32] M. Karle, S. K. Vashist, R. Zengerle, F. von Stetten, "Microfluidic solutions enabling continuous processing and monitoring of biological samples: A review," *Anal. Chim. Acta*, vol. 929, pp. 1-22, 2016.

[33] J. Chen, J. Li, Y. Sun, "Microfluidic approaches for cancer cell detection, characterization, and separation," *Lab Chip*, vol. 12, pp. 1753-1767, 2012.

[34] C. W. Shields IV, C. D. Reyes, G. P. López, "Microfluidic cell sorting: a review of the advances in the separation of cells from debulking to rare cell isolation," *Lab Chip*, vol. 15, pp. 1230-1249, 2015.

[35] A. F. Sarioglu, N. Aceto, N. Kojic, M. C. Donaldson, M. Zeinali, B. Hamza, A. Engstrom, H. Zhu, T. K. Sundaresan, D. T. Miyamoto, X. Luo, A. Bardia, B. S. Wittner, S. Ramaswamy, T. Shioda, D. T. Ting, S. L. Stott, R. Kapur, S. Maheswaran, D. A. Haber, M. Toner, "A microfluidic device for label-free, physical capture of circulating tumor cell clusters," *Nat. Methods*, vol. 12, pp. 685-691, 2015.

[36] M. Hosokawa, T. Hayata, Y. Fukuda, A. Arakaki, T. Yoshino, T. Tanaka, T. Matsunaga, "Size-selective microcavity array for rapid and efficient detection of circulating tumor cells," *Anal. Chem.*, vol. 82, pp. 6629-6635, 2010.

[37] C. H. Hsu, D. Di Carlo, C. Chen, D. Irimia, M. Toner, "Microvortex for focusing, guiding and sorting of particles," *Lab Chip*, vol. 8, pp. 2128-2134, 2008.

[38] N. Haandbæk, O. With, S. C. Bürgel, F. Heer, A. Hierlemann, "Resonance-enhanced microfluidic impedance cytometer for detection of single bacteria," *Lab Chip*, vol. 14, pp. 3313-3324, 2014.

[39] J. S. Mellors, K. Jorabchi, L. M. Smith, J. M. Ramsey, "Integrated microfluidic device for automated single cell analysis using electrophoretic separation and electrospray ionization mass spectrometry," *Anal. Chem.*, vol. 82, pp. 967-973, 2010.

[40] A. Adamo, A. Sharei, L. Adamo, B. Lee, S. Mao, K. F. Jensen, "Microfluidics-based assessment of cell deformability," *Anal. Chem.*, vol. 84, pp. 6438-6443, 2012.

[41] S. Byun, S. Son, D. Amodei, N. Cermak, J. Shaw, J. H. Kang, V. C. Hecht, M. M. Winslow, T. Jacks, P. Mallick, S. R. Manalis, "Characterizing deformability and surface friction of cancer cells," *Proc. Natl. Acad. Sci. U. S. A.*, vol. 110, pp. 7580-7585, 2013.

[42] Z. Du, N. Colls, K. H. Cheng, M. W. Vaughn, L. Gollahon, "Platinum nanoparticles-doped sol-gel/carbon nanotubes composite electrochemical sensors and biosensors," *Biosens. Bioelectron.*, vol. 21, pp. 1991-1995, 2006.

[43] S. Nagrath, L. V. Sequist, S. Maheswaran, D. W. Bell, D. Irimia, L. Ulkus, M. R. Smith, E. L. Kwak, S. Digumarthy, A. Muzikansky, P. Ryan, U. J. Balis, R. G. Tompkins, D. A. Haber, M. Toner, "Isolation of rare circulating tumour cells in cancer patients by microchip technology," *Nature*, vol. 450, pp. 1235-1239, 2007.

[44] Q. Xiang, X. Xuan, B. Xu, D. Li, "Multi-functional particle detection with embedded optical fibers in a poly(dimethylsiloxane) chip," *Instrum. Sci. Technol.*, vol. 33, pp. 597-607, 2005.

[45] P. Kiesel, M. Bassler, M. Beck, N. Johnson, "Spatially modulated fluorescence emission from moving particles" *Appl. Phys. Lett.*, vol. 94, 041107, 2009.

[46] Z. Wang, S. Y. Chin, C. D. Chin, J. Sarik, M. Harper, J. Justman, S. K. Sia, "Microfluidic CD4+ T-cell counting device using chemiluminescence-based detection," *Anal. Chem.*, vol. 82, pp. 36-40, 2010.

[47] S. M. Imaad, N. Lord, G. Kulsharova, G. L. Liu, "Microparticle and cell counting with digital microfluidic compact disc using standard CD drive," *Lab Chip*, vol. 11, pp. 1448-1456, 2011.

[48] T. Kartanas, V. Ostanin, P. K. Challa, R. Daly, J. Charmet, T. P. J. Knowles, "Enhanced quality factor label-free biosensing with micro-cantilevers integrated into microfluidic systems," *Anal. Chem.*, vol. 89, pp. 11929-11936, 2017.

[49] A. K. Vutha, B. Davaji, C. H. Lee, G. M. Walker, "A microfluidic device for thermal particle detection," *Microfluid. Nanofluid.*, vol. 17, pp. 871-878, 2014.

[50] C. Hu, S. Kalsi, I. Zeimpekis, K. Sun, P. Ashburn, C. Turner, J. M. Sutton, H. Morgan, "Ultra-fast electronic detection of antimicrobial resistance genes using isothermal amplification and thin film transistor sensors," *Biosens. Bioelectron.*, vol. 96, pp. 281-287, 2017.

[51] L. T. Sexton, L. P. Horne, S. A. Sherrill, G. W. Bishop, L. A. Baker, C. R. Martin, "Resistive-pulse studies of proteins and protein/antibody complexes using a conical nanotube sensor," *J. Am. Chem. Soc.*, vol. 129, pp. 13144-13152, 2007.

[52] S. Murali, A. V. Jagtiani, X. Xia, J. Carletta, J. Zhe, "A microfluidic Coulter counting device for metal wear detection in lubrication oil," *Rev. Sci. Instrum.*, vol. 80, 016105, 2009.

[53] R. Lin, J. L. Prieto, J. S. Fisher, A. P. Lee, "High efficiency cell encapsulation utilizing novel on-demand droplet generation scheme and impedance-based detection," *Proceedings of uTAS (The 14th International Conference on Miniaturized Systems for Chemistry and Life Science)*, Groningen, the Netherlands, October 3-7, 2010.

[54] M. A. M. Gijs, F. Lacharme, U. Lehmann, "Microfluidic applications of magnetic particles for biological analysis and catalysis," *Chem. Rev.*, vol. 110, pp. 1518-1563, 2010.

[55] Z. Altintas, M. Akgun, G. Kokturk, Y. Uludag, "A fully automated microfluidic-based electrochemical sensor for real-time bacteria detection," *Biosens. Bioelectron.*, vol.100, pp. 541-548, 2018.

[56] Z. Yang, Y. Zhang, T. Itoh, R. Maeda, "A novel MEMS compatible lab-on-a-tube technology," *Lab Chip*, vol. 14, pp. 4604-4608, 2014.

[57] W. H. Coulter, "High speed automatic blood cell counter and cell size analyzer," *Proc. Natl. Electron. Conf.*, vol. 12, pp. 1034-1042, 1956.

[58] R. W. DeBlois, C. P. Bean, "Counting and Sizing of Submicron Particles by the Resistive Pulse Technique," *Rev. Sci. Instrum.*, vol. 41, pp. 909-916, 1970.

[59] D. Polling, S. C. Deane, M. R. Burcher, C. Glasse, C. H. Reccius, "Coded electrodes for low signalnoise ratio single cell detection in flow-through impedance spectroscopy," *Proceedings of uTAS (The 14th International Conference on Miniaturized Systems for Chemistry and Life Science)*, Groningen, the Netherlands, October 3-7, 2010.

[60] S. Emaminejad, S. Talebi, R. W. Davis, M. Javanmard, "Multielectrode sensing for extraction of signal from noise in impedance cytometry," *IEEE Sensors J.*, vol. 15, pp. 2715-2716, 2015.

[61] K. R. Balakrishnan, G. Anwar, M. R. Chapman, T. Nguyen, A. Kesavaraju, L. L. Sohn, "Node-pore sensing: a robust, high-dynamic range method for detecting biological species," *Lab Chip*, vol. 13, pp. 1302-1307, 2013.

[62] P. Xie, X. Cao, Z. Lin, N. Talukder, S. Emaminejad, M. Javanmard, "Processing gain and noise in multi-electrode impedance cytometers: Comprehensive electrical design methodology and characterization," *Sens. Actuators B Chem.*, vol. 241, pp. 672-680, 2017.

[63] M. R. Kellman, F. R. Rivest, A. Pechacek, L. L. Sohn, M. Lustig, "Node-pore coded coincidence correction: Coulter counters, code design, and sparse deconvolution," *IEEE Sensors J.*, vol. 18, pp. 3068-3079, 2018.

[64] S. Gawad, L. Schild, P. Renaud, "Micromachined impedance spectroscopy flow cytometer for cell analysis and particle sizing," *Lab Chip*, vol. 1, pp. 76-82, 2001.

[65] D. Holmes, D. Pettigrew, C. H. Reccius, J. D. Gwyer, C. van Berkel, J. Holloway, D. E. Davies, H. Morgan, "Leukocyte analysis and differentiation using high speed microfluidic single cell impedance cytometry," *Lab Chip*, vol. 9, pp. 2881-2889, 2009.

[66] N. N. Watkins, S. Sridhar, X. Cheng, G. D. Chen, M. Toner, W. Rodriguez, R. Bashir, "A microfabricated electrical differential counter for the selective enumeration of CD4+ T lymphocytes," *Lab Chip*, vol. 11, pp. 1437-1447, 2011.

[67] O. A. Saleh, L. L. Sohn, "Direct detection of antibody-antigen binding using an on-chip artificial pore," *Proc. Natl. Acad. Sci. U. S. A.*, vol. 100, pp. 820-824, 2003.

[68] R. Rodrigiez-Trujillo, M. A. Ajine, A. Ozran, M. D. Mar, F. Larsen, C. H. Clausen, W. E. Svendsen, "Label-free protein detection using a microfluidic Coulter-counter device," *Sens. Actuators B Chem.*, vol. 190, pp. 922-927, 2014.

[69] J. Mok, M. N. Mindrinos, R. W. Davis, M. Javanmard, "Digital microfluidic assay for protein detection," *Proc. Natl. Acad. Sci. U. S. A.*, vol. 111, pp. 2110-2115, 2014.

[70] O. A. Saleh, L. L. Sohn, "An artificial nanopore for molecular sensing," *Nano Lett.*, vol. 3, pp. 37-38, 2003.

[71] R. W. DeBlois, R. K. A. Wesley, “Sizes and concentrations of several type C oncornaviruses and bacteriophage T2 by the resistive-pulse technique,” *J. Virol.*, vol. 23, pp. 227-233, 1977.

[72] O. A. Saleh, L. L. Sohn, “Quantitative sensing of nanoscale colloids using a microchip Coulter counter,” *Rev. Sci. Instrum.*, vol. 72, pp. 4449-4451, 2001.

[73] N. N. Watkins, U. Hassan, G. Damhorst, H. Ni, A. Vaid, W. Rodriguez, R. Bashir, “Microfluidic CD4+ and CD8+ T lymphocyte counters for point-of-care HIV diagnostics using whole blood,” *Sci. Trans. Med.*, vol. 5, 214ra170, 2013.

[74] U. Hassan, R. Zhu, R. Bashir, “Multivariate computational analysis of biosensor's data for improved CD64 quantification for sepsis diagnosis,” *Lab Chip*, vol. 18, pp. 1231-1240, 2018.

[75] E. Valera, J. Berger, U. Hassan, T. Ghonge, J. Liu, M. Rappleye, J. Winter, D. Abboud, Z. Haidry, R. Healey, N. T. Hung, N. Leung, N. Mansury, A. Hasnain, C. Lannon, Z. Price, K. White, R. Bashir, “A microfluidic biochip platform for electrical quantification of proteins,” *Lab Chip*, vol. 18, pp. 1461-1470, 2018.

[76] U. Hassan, T. Ghonge, B. Reddy Jr., M. Patel, M. Rappleye, I. Taneja, A. Tanna, R. Healey, N. Manusry, Z. Price, T. Jensen, J. Berger, A. Hasnain, E. Flaugher, S. Liu, B. Davis, J. Kumar, L. White, R. Bashir, “A point-of-care microfluidic biochip for quantification of CD64 expression from whole blood for sepsis stratification,” *Nat. Comm.*, vol. 8, 15949, 2017.

[77] J. Zhe, A. Jagtiani, P. Dutta, J. Hu, J. Carletta, “A micromachined high throughput Coulter counter for bioparticle detection and counting,” *J. Micromech. Microeng.*, vol. 17, pp. 304-313, 2007.

[78] Y. Song, J. Yangi, X. Pan, D. Li, “High-throughput and sensitive particle counting by a novel microfluidic differential resistive pulse sensor with multidetecting channels and a common reference channel,” *Electrophoresis*, vol. 36, pp. 495-501, 2015.

[79] Y. Chen, S. J. Kim, J. Guo, Y. Kang, J. P. Kausalya, “Portable Coulter counter with vertical through-holes for high-throughput applications,” *Sens. Actuators B Chem.*, vol. 213, pp. 375-381, 2015.

[80] A. V. Jagtiani, J. Carletta, J. Zhe, "A microfluidic multichannel resistive pulse sensor using frequency division multiplexing for high throughput counting of micro particles," *J. Micromech. Microeng.*, vol. 21, 065004, 2011.

[81] J. Skommer, J. Akagi, K. Takeda, Y. Fujimura, K. Khoshmanesh, D. Wlodkowic, "Multiparameter lab-on-a-chip flow cytometry of the cell cycle," *Biosens. Bioelectron.*, vol. 42, pp. 586-591, 2013.

[82] H. Y. Huang, H. T. Fu, H. Y. Tsing, H. J. Huang, C. J. Li, D. J. Yao, "Motile human sperm sorting by an integrated microfluidic system," *J. Nanomed. Nanotechnol.*, vol. 5, 199, 2014.

[83] S. Y. Yang, K. Y. Lien, K. J. Huang, H. Y. Lei, G. B. Lee, "Micro flow cytometry utilizing a magnetic bead-based immunoassay for rapid virus detection," *Biosens. Bioelectron.*, vol. 24, pp. 855-862, 2008.

[84] J. P. Golden, J. Verbarg, P. B. Howell Jr., L. C. Shriver-Lake, F. S. Ligler, "Automated rocessing integrated with a microflow cytometer for pathogen detection in clinical matrices," *Biosens. Bioelectron.*, vol. 40, pp. 10-16, 2013.

[85] D. Vercruysse, A. Dusa, R. Stahl, G. Vanmeerbeeck, K. de Wijs, C. Liu, D. Prodanov, P. Peumans, L. Lagae, "Three-part differential of unlabeled leukocytes with a compact lens-free imaging flow cytometer," *Lab Chip*, vol. 15, pp. 1123-1132, 2015.

[86] R. J. Yang, H. H. Hou, Y. N. Wang, C. H. Lin, L. M. Fu, "A hydrodynamic focusing microchannel based on micro-weir shear lift force," *Biomicrofluidics*, vol. 6, 034110, 2012.

[87] M. Frankowski, J. Theisen, A. Kummrow, P. Simon, H. Ragusch, N. Bock, M. Schmidt, J. Neukammer, "Microflow cytometers with integrated hydrodynamic focusing," *Sensors*, vol. 13, pp. 4674-4693, 2013.

[88] S. C. Lin, P. W. Yen, C. C. Peng, Y. C. Tung, "Single channel layer, single sheath-flow inlet microfluidic flow cytometer with three-dimensional hydrodynamic focusing," *Lab Chip*, vol. 12, pp. 3135-3141, 2012.

[89] A. A. Nawaz, X. Zhang, X. Mao, J. Rufo, S. C. S. Lin, F. Guo, Y. Zhao, M. Lapsley, P. Li, J. P. McCoy, S. J. Levine, T. J. Huang, "Sub-micrometer-precision, three-

dimensional (3D) hydrodynamic focusing via ‘microfluidic drifting’,” *Lab Chip,* vol. 14, pp. 415-423, 2014.

[90] M. A. Daniele, D. A. Boyd, D. R. Mott, F. S. Ligler, “3D hydrodynamic focusing microfluidics for emerging sensing technologies,” *Biosens. Bioelectron.*, vol. 67, pp. 25-34, 2015.

[91] J. M. Martel, M. Toner, “Inertial focusing in microfluidics,” *Annu. Rev. Biomed. Eng.*, vol. 16, pp. 371-396, 2014.

[93] A. J. Chung, D. R. Gossett, D. Di Carlo, “Three dimensional, sheathless, and high-throughput microparticle inertial focusing through geometry-induced secondary flows," *Small,* vol. 9, pp. 685-690, 2013.[103] W. Xun, J. Feng, H. Chang, “A microflow cytometer based on a disposable microfluidic chip with side scatter and fluorescence detection capability,” *IEEE Trans. Nanobioscience*, vol. 14, pp. 850-856, 2015.

[94] A. B. Shrirao, Z. Fritz, E. M. Novik, G. M. Yarmush, R. S. Schloss, J. D. Zahn, M. L. Yarmush, “Microfluidic flow cytometry: The role of microfabrication methodologies, performance and functional specification,” *Technology*, vol. 6, pp. 1-23, 2018.

[95] R. J. Yang, L. M. Fu, H. H. Hou, “Review and perspectives on microfluidic flow cytometers,” *Sens. Actuators B Chem.,* vol. 266, pp. 26-45, 2018.

[96] M. Shaker, L. Colella, F. Caselli, P. Bisegna, P. Renaud, “An impedance-based flow microcytometer for single cell morphology discrimination,” *Lab Chip,* vol. 14, pp. 2548-2555, 2014.

[97] D. Holmes, J. K. She, P. L. Roach, H. Morgan, “Bead-based immunoassays using a micro-chip flow cytometer,” *Lab Chip,* vol. 7, pp. 1048-1056, 2007.

[98] C. Grenvall, C. Antfolk, C. Z. Bisgaard, T. Laurell, “Two-dimensional acoustic particle focusing enables sheathless chip Coulter counter with planar electrode configuration,” *Lab Chip,* vol. 14, pp. 4629-4637, 2014.

[99] J. Chen, A. A. Nawaz, Y. Zhao, P. H. Huang, J. P. McCoy, S. J. Levine, L. Wang, T. J. Huang, “Standing surface acoustic wave (SSAW)-based microfluidic cytometer,” *Lab Chip*, vol. 14, pp. 916-923, 2014.

[100] P. Sajeesh, A. K. Sen, “Particle separation and sorting in microfluidic devices: a review,” *Microfluid. Nanofluid.,* vol. 17, pp. 1-52, 2014.

[101] Y. C. Tung, M. Zhang, C. T. Lin, K. Kurabayashi, S. J. Skerlos, “PDMS-based opto-fluidic micro flow cytometer with two-color, multi-angle fluorescence detection capability using PIN photodiodes,” *Sens. Actuators B Chem.,* vol. 98, pp. 356-367, 2004.

[102] W. Shi, L. Guo, H. Kasdan, Y. C. Tai, “Four-part leukocyte differential count based on sheathless microflow cytometer and fluorescent dye assay,” *Lab Chip,* vol. 13, pp. 1257-1265, 2013.

[103] W. Xun, J. Feng, H. Chang, “A microflow cytometer based on a disposable microfluidic chip with side scatter and fluorescence detection capability,” *IEEE Trans. Nanobioscience,* vol. 14, pp. 850-856, 2015.

[104] K. Goda, A. Ayazi, D. R. Gossett, J. Sadasivam, C. K. Lonappan, E. Sollier, A. M. Fard, S. C. Hur, J. Adam, C. Murray, C. Wang, N. Brackbill, D. Di Carlo, B. Jalali, “High-throughput single-microparticle imaging flow analyzer,” *Proc. Natl. Acad. Sci. U. S. A.,* vol. 109, pp. 11630-11635, 2012.

[105] T. Sawetzki, C. D. Eggleton, S. A. Desai, D. W. M. Marr, “Viscoelasticity as a biomarker for high-throughput flow cytometry,” *Biophys. J.,* vol. 105, pp. 2281-2288, 2013.

[106] M. A. Mansor, M. Takeuchi, M. Nakajima, Y. Hasegawa, M. R. Ahmad, “A novel integrated dual microneedle-microfluidic impedance flow cytometry for cells detection in suspensions,” *Int. J. Elect. Com. Eng.,* vol. 7, pp. 1513-1521, 2017.

[107] A. El Hasni, C. Schmitz, K. Bui-Göbbels, P. Bräunig, W. Jahnen-Dechent, U. Schnakenberg, “Electrical impedance spectroscopy of single cells in hydrodynamic traps,” *Sens. Actuators B Chem.,* vol. 248, pp. 419-429, 2017.

[108] K. Cheung, S. Gawad, P. Renaud, “Impedance spectroscopy flow cytometry: On chip label-free cell differentiation,” *Cytometry A,* vol. 65A, pp. 124-132, 2005.

[109] J. Chen, Y. Zheng, Q. Tan, E. Shojaei-Baghini, Y. L. Zhang, J. Li, P. Prasad, L. You, X. Y. Wu, Y. Sun, “Classification of cell types using a microfluidic device for mechanical and electrical measurement on single cells,” *Lab Chip,* vol. 11, pp. 3174-3181, 2011.

[110] Y. Song, M. Li, J. Yang, J. Wang, X. Pan, Y. Sun, D. Li, "Capacitive detection of living microalgae in a microfluidic chip," *Sens. Actuators B Chem.*, vol. 194, pp. 164-172, 2014.

[111] M. Helou, M. Reisbeck, S. F. Tedde, L. Richter, L. Bär, J. J. Bosch, R. H. Stauber, E. Quandt, O. Hayden, "Time-of-flight magnetic flow cytometry in whole blood with integrated sample preparation," *Lab Chip*, vol. 13, pp 1035-1038, 2013.

[112] K. S. Kim, J. K. Park, "Magnetic force-based multiplexed immunoassay using superparamagnetic nanoparticles in microfluidic channel," *Lab Chip*, vol. 5, pp. 657-664, 2005.

[113] Y. Komatsu, R. Nagaoka, K. Funamoto, T. Hayase, N. Masauzi, H. Kanai, Y. Saijo, "'Sonocytometry' - Novel diagnostic method of ultrasonic differentiation of cells in blood flow," in *2014 36th Annual International Conference of the IEEE Engineering in Medicine and Biology Society*, pp. 2761-2764, Chicago, IL, USA, Augest 26-30, 2014.

[114] Y. Gong, N. Fan, X. Yang, B. Peng, H. Jiang, "New advances in microfluidic flow cytometry," *Electrophoresis*, vol. 40, pp. 1212-1229, 2019.

[115] E. I. Galanzha, V. P. Zharov, "Circulating Tumor Cell Detection and Capture by Photoacoustic Flow Cytometry in Vivo and ex Vivo," *Cancers*, vol. 5, pp. 1691-1738, 2013.

[116] R. Liu, N. Wang, F. Kamili, A. F. Sarioglu, "Microfluidic CODES: a scalable multiplexed electronic sensor for orthogonal detection of particles in microfluidic channels," *Lab Chip*, vol. 16, pp. 1350-1357, 2016.

[117] D. Torrieri, Principle of Spread-Spectrum Communication Systems, Springer, New York, NY, 2015.

[118] R. Rao, S. Dianat, Basics of Code Division Multiple Access (CDMA), SPIE, 2005.

[119] J. G. Proakis, Digital Communications (2nd ed.), McGraw-Hill, New York, NY, 1989.

[120] E. H. Dinan, B. Jabbari, "Spreading codes for direct sequence CDMA and wideband CDMA cellular networks," *IEEE Commun. Mag.*, vol. 36, pp. 48-54, 1998.

[121] R. Gold, "Optimal binary sequences for spread spectrum multiplexing," *IEEE Trans. Inf. Theory*, vol. 13, pp. 619-621, 1967.

[122] R. Gold, "Maximal recursive sequences with 3-valued recursive cross-correlation functions," *IEEE Trans. Inf. Theory*, vol. 14, pp. 154-156, 1968.

[123] I. A. Glover and P. M. Grant, Digital Communications, Prentice Hall Europe, London, Great Britain, 1998.

[124] J. A. Salehi, "Code division multiple-access techniques in optical fiber networks. I. Fundamental principles," *IEEE Trans. Commun.*, vol. 37, pp. 824-833, 1989.

[125] D. Zaccarin, M. Kavehrad, "Performance evaluation of optical CDMA systems using non-coherent detection and bipolar codes," *J. Lightware Technol.*, vol. 12, pp. 96-105, 1994.

[126] S. Verdu, Multiuser Detection, Cambridge University Press, Cambridge, UK, 1998.

[127] R. Liu, W. Waheed, N. Wang, O. Civelekoglu, M. Boya, C. H. Chu, A. F. Sarioglu, "Design and modeling of electrode networks for code-division multiplexed resistive pulse sensing in microfluidic devices," *Lab Chip*, vol. 17, pp. 2650-2666, 2017.

[128] K. R. Foster, H. P. Schwan, "Dielectric properties of tissues and biological materials: a critical review," *Crit. Rev. Biomed. Eng.*, vol. 17, pp. 25-104, 1989.

[129] T. Sun, H. Morgan, "Single-cell microfluidic impedance cytometry: a review," *Microfluid. Nanofluid.*, vol. 8, pp. 423-443, 2010.

[130] W. Franks, I. Schenker, P. Schmutz, A. Hierlemann, "Impedance characterization and modeling of electrodes for biomedical applications," *IEEE Trans. Biomed. Eng.*, vol. 52, pp. 1295-1302, 2005.

[131] T. Sun, C. Bernabini, H. Morgan, "Single-colloidal particle impedance spectroscopy: Complete equivalent circuit analysis of polyelectrolyte microcapsules," *Langmuir,* vol. 26, pp. 3821-3828, 2009.

[132] M. Marcali, C. Elbuken, " Impedimetric detection and lumped element modelling of a hemagglutination assay in microdroplets," *Lab Chip,* vol. 16, 2494-2503, 2016.

[133] J. Hong, D. S. Yoon, S. K. Kim, T. S. Kim, S. Kim, E. Y. Pak and K. No, AC frequency characteristics of coplanar impedance sensors as design parameters," *Lab Chip,* vol. 5, pp. 270-279, 2005.

[134] G. Mernier, E. Duqi, P. Renaud, "Characterization of a novel impedance cytometer design and its integration with lateral focusing by dielectrophoresis," *Lab Chip,* vol. 12, pp. 4344-4349, 2012.

[135] J. C. Maxwell, A Treatise on Electricity and Magnetism, Dover Publications, New York, NY, 1954.

[136] Z. Stojek, Chapter I.1, 3-9, in Electroanalytical Methods, ed. F. Scholz, Springer-Verlag, Heidelberg, Germany, 2010.

[137] P. Jacobs, A. Varlan and W. Sansen, "Design optimisation of planar electrolytic conductivity sensors," *Med. Biol. Eng. Comput.*, vol. 33, pp. 802-810, 1995.

[138] W. Olthuis, W. Streekstra and P. Bergveld, "Theoretical and experimental determination of cell constants of planar-interdigitated electrolyte conductivity sensors," *Sens. Actuators B Chem.*, vol. 24, pp. 252-256, 1995.

[139] A. R. Varlan, P. Jacobs and W. Sansen, "New design technique for planar conductometric haematocrit sensors," *Sens. Actuators B Chem.*, vol. 34, pp. 258-264, 1996.

[140] P. Linderholm and P. Renaud, "Comment on "AC frequency characteristics of coplanar impedance sensors as design parameters" by Jongin Hong, Dae Sung Yoon, Sung Kwan Kim, Tae Song Kim, Sanghyo Kim, Eugene Y. Pak and Kwangsoo No, Lab Chip, 2005, 5, 270," *Lab Chip*, vol. 5, pp. 1416-1417, 2005.

[141] N. Demierre, T. Braschler, P. Linderholm, U. Seger, H. van Lintel and P. Renaud, "Characterization and optimization of liquid electrodes for lateral dielectrophoresis," *Lab Chip*, vol. 7, pp. 355-365, 2007.

[142] R. Schinzinger , P. A. A. Laura, Conformal mapping: methods and applications, Elsevier, Amsterdam, The Netherlands, 1991.

[143] H. Morgan, T. Sun, D. Holmes, S. Gawad, N. G. Green, "Single cell dielectric spectroscopy," *J. Phys. D: Appl. Phys.*, vol. 40, pp. 61-70, 2007.

[144] S. Gawad, K. Cheung, U. Seger, A. Bertsch, P. Renaud, "Dielectric spectroscopy in a micromachined flow cytometer: theoretical and practical considerations," *Lab Chip*, vol. 4, pp. 241-251, 2004.

[145] K. L. Chopra, L. C. Bobb, M. H. Francombe, "Electrical Resistivity of Thin Single‐Crystal Gold Films," *J. Appl. Phys.*, vol. 34, pp. 1699-1702, 1963.

[146] A. Olmo, A. Yúfera, "Computer simulation of microelectrode based bio-impedance measurements with COMSOL," *Proceedings of BIODEVICES (The 3rd International Conference on Biomedical Electronics and Devices)*, Valencia, Spain, January 20-23, 2010.

[147] A. Yúfera, A. Olmo, P. Daza, D. Cañete, in Advanced Biometric Technologies, ed. G. Chetty and J. Yang, InTech, Rijeka, Croatia, 2011, Chapter 17, 343-366.

[148] U. Hassan, N. N. Watkins, C. Edwards, R. Bashir, "Flow metering characterization within an electrical cell counting microfluidic device," *Lab Chip*, vol. 14, pp. 1469-1476, 2014.

[149] D. Spencer, F. Caselli, P. Bisegna, H. Morgan, "High accuracy particle analysis using sheathless microfluidic impedance cytometry," *Lab Chip*, vol. 16, pp. 2467-2473, 2016.

[150] A. De Ninno, V. Errico, F. R. Bertani, L. Businaro, P. Bisegna, F. Caselli, "Coplanar electrode microfluidic chip enabling accurate sheathless impedance cytometry," *Lab Chip*, vol. 17, pp. 1158-1166, 2017.

[151] N. Wang, R. Liu, A. F. Sarioglu, “Microfluidic Platform with Multiplexed Electronic Detection for Spatial Tracking of Particles,” *J. Visualized Exp.*, vol. 121, e55311, 2017.

[152] R. Liu, N. Wang, W. Waheed, A. F. Sarioglu, “A scalable electronic sensor for multiplexed detection of cells in different microfluidic channels,” in *Proceeding of Solid-State Sensors, Actuators and Microsystems Workshop*, pp. 376-379, Hilton Head Island, South Carolina, June 5-9, 2016.

[153] R. Liu, N. Wang, N. Asmare, A. F. Sarioglu, “Scaling code-multiplexed electrode networks for distributed Coulter detection in microfluidics,” *Biosens. Bioelectron.*, vol. 120, pp. 30-38, 2018.

[154] J. M. Holtzman, “A simple, accurate method to calculate spread-spectrum multiple-access error probabilities,” *IEEE Trans. Commun.*, vol. 40, pp. 461-464, 1992.

[155] T. S. Rappaport, Wireless Communications: Principles and Practice, second ed., Prentice Hall, New Jersey, 2002.

[156] J. M. Holtzman, “On using perturbation analysis to do sensitivity analysis: derivatives versus differences,” *IEEE Trans. Autom. Control*, vol. 37, pp. 243-247, 1992.

[157] J. C. Liberti, T. S. Rappaport, “Accurate techniques to evaluate CDMA bit error rates in multipath channels with imperfect power Control,” *IEEE Global Telecommunications Conference*, GLOBECOM ’95, pp. 33-37, Singapore, 1995.

[158] R. Liu, C. H. Chu, M. Boya, D. Lee, O. Civelekoglu, H. Chen, A. F. Sarioglu, “Analysis and characterization of soft-lithography-compatible parallel-electrode-sensors in microfluidic devices,” 2019 *20th International Conference on Solid-State Sensors, Actuators and Microsystems & Eurosensors XXXIII (TRANSDUCERS & EUROSENSORS XXXIII)*, Berlin, Germany, June 23-27, 2019, pp. 1744-1747.

[159] W. Zhang, Y. Hu, G. Choi, S. Liang, M. Liu, W. Guan, “Microfluidic multiple cross-correlated Coulter counter for improved particle size analysis,” *Sens. Actuators B Chem.*, vol. 296, 126615, 2019.

[160] V. Errico, A. De Ninno, F. R. Bertani, L. Businaro, P. Bisegna, F. Caselli, “Mitigating positional dependence in coplanar electrode Coulter-type microfluidic devices,” *Sens. Actuators B Chem.*, vol. 247, pp. 580-586, 2017.

[161] J. M. R. Rickel, A. J. Dixon, A. L. Klibanov, J. A. Hossack, “A flow focusing microfluidic device with an integrated Coulter particle counter for production, counting and size characterization of monodisperse microbubbles,” *Lab Chip*, vol. 18, pp. 2653-2664, 2018.

[162] S. Dekker, P. K. Isgor, T. Feijten, L. I. Segerink, M. Odijk, “From chip-in-a-lab to lab-on-a-chip: a portable Coulter counter using a modular platform,” *Microsyst. Nanoeng.*, vol. 4, 34, 2018.

[163] F. Liu, Y. Han, L. Du, P. Huang, J. Zhe, “Airborne mineral dust measurement using an integrated microfluidic device,” *Microfluid Nanofluidics*, vol. 20, 27, 2016.

[164] R. Liu, N. Wang, C. H. Chu, A. F. Sarioglu, “The effect of the electrode resistance on the performance of code-multiplexed resistive pulse sensing”, 2017 *19th International Conference on Solid-State Sensors, Actuators and Microsystem (TRANSDUCERS)*, pp. 2115-2118, Kaoshiung, June 18-22, 2017.

[165] R. Liu, C. Chu, M. Boya, O. Civelekoglu, H. Chen, A. F. Sarioglu, “Soft lithography compatible fabrication of parallel electrodes in microfluidic devices,” in *Proc. of uTAS (The 22nd International Conference on Miniaturized Systems for Chemistry and Life Sciences)*, pp. 825-827, Kaoshiung, November 11-15, 2018.

[166] N. Wang, R. Liu, C. H. Chu, A. F. Sarioglu, “A multiplexed resistive pulse sensor network for simultaneous detection of cells in a 10-channel microfluidic chip,” in *Proc. of uTAS (The 20th International Conference on Miniaturized Systems for Chemistry and Life Sciences)*, pp. 1388-1389, Dublin, Ireland, October 9-13, 2016.

[167] D. K. Wood, M. V. Requa, A. N. Cleland, “Microfabricated high-throughput electronic particle detector,” *Rev. Sci. Instrum.*, vol. 78, 104301, 2017.

[168] F. Caselli, P. Bisegna, F. Maceri, “EIT-inspired microfluidic cytometer for single-cell dielectric spectroscopy,” *J. Microelectromech. S.*, vol. 19, pp. 1029-1040, 2010.

[169] D. Spencer, H. Morgan, “Positional dependence of particles in microfludic impedance cytometry,” *Lab Chip*, vol. 11, pp. 1234-1239, 2011.

[170] T. L. Edwards, J. C. Harper, R. Polsky, D. M. Lopez, D. R. Wheeler, A. C. Allen, S. M. Brozik, “A parallel microfluidic channel fixture fabricated using laser ablated plastic laminates for electrochemical and chemiluminescent biodetection of DNA,” *Biomicrofluidics*, vol. 5, 044115, 2011

[171] L. I. Segerink, A. J. Sprenkels, J. G. Bomer, I. Vermes, A. van der Berg, "A new floating electrode structure for generating homogeneous electrical fields in microfluidic channels," *Lab Chip*, vol. 11, pp. 1995-2001, 2011.

[172] A. L. Kadilak, Y. Liu, S. Shrestha, J. R. Bernard, W. E. Mustain, L. M. Shor, "Selective deposition of chemically-bonded gold electrodes onto PDMS microchannel side walls," *J. Electroanal. Chem.*, vol. 727, pp. 141-147, 2014.

[173] R. Liu, C. H. Chu, T. Ozkaya-Ahmadov, O. Civilekoglu, D. Lee, AKM Arifuzzman, A. F. Sarioglu, "Combinatorial immunophenotyping of cell populations with an electronic antibody microarray," *Small*, vol. 15, 1904732, 2019.

[174] Z. Tong, G. Rajeev, K. Guo, A. Ivask, S. McCormick, E. Lombi, C. Priest, N. H. Voelcker, "Microfluidic cell microarray platform for high throughput analysis of particle-cell interactions," *Anal. Chem.*, vol. 90, pp. 4338-4347, 2018.

[175] H. T. Nguyen, L. N. Dupont, A. M. Jean, T. Géhin, Y. Chevolot, E. Laurenceau, M. A. M. Gijs, "Microfluidic extraction and microarray detection of biomarkers from cancer tissue slides," *J. Micromech. Microeng.*, vol. 28, 034004, 2018.

[176] W. Y. Huang, S. T. Chou, C. H. Chen, S. Y. Chou, J. H. Wu, Y. C. Chen, G. B. Lee, "An automatic integrated microfluidic system for allergy microarray chips," *Analyst*, vol. 143, pp. 2285-2292, 2018.

[177] C. Cozens-Roberts, D. A. Lauffenburger, J. A. Quinn, "Receptor-mediated cell attachment and detachment kinetics. I. Probabilistic model and analysis," *Biophys. J.*, vol. 58, pp. 841-856, 1990.

[178] Y. Zhang, V. Lyons, D. Pappas, "Fundamentals of affinity cell separations," *Electrophoresis*, vol. 39, pp. 732-741, 2018.

[179] M. A. Ingersoll, R. Spanbroek, C. Lottaz, E. L. Gautier, M. Frankenberger, R. Hoffmann, R. Lang, M. Haniffa, M. Collin, F. Tacke, A. J. R. Habenicht, L. Zieler-Heitbrock, G. J. Randolph, "Comparison of gene expression profiles between human and mouse monocyte subsets," *Blood*, vol. 115, pp. e10-e19, 2010.

[180] H. Schneck, B. Gierke, F. Uppenkamp, B. Behrens, D. Niederacher, N. H. Stoecklein, M. F. Templin, M. Pawlak, T. Fehm, H. Neubauer, "EpCAM-independent enrichment of circulating tumor cells in metastatic breast cancer," *PLoS ONE*, vol. 10, e0144535, 2015.

[181] J. Yoon, A. Terada, H. Kita, "CD66b Regulates Adhesion and Activation of Human Eosinophils," *J. Immunol.*, vol. 179, pp. 8454-8462, 2007.

[182] G. Del Poeta, L. Maurillo, A. Venditti, F. Buccisano, A. M. Epiceno, G. Capelli, A. Tamburini, G. Suppo, A. Battaglia, M. I. Del Principe, B. Del Moro, M. Masi, S. Amadori, "Clinical significance of CD38 expression in chronic lymphocytic leukemia," *Blood*, vol. 98, pp. 2633-2639, 2001.

[183] M. Schneider, V. Schumacher, T. Lischke, K. Lücke, C. Meyer-Schwesinger, J. Velden, F. Koch-Nolte, H.W. Mittrücker, "CD38 is expressed on inflammatory cells of the intestine and promotes intestinal inflammation," *PLoS ONE*, vol. 10, e0126007, 2015.

[184] T. Hernández-Caselles, M. Martínez-Esparza, A. B. Pérez-Oliva, A. M. Quintanilla-Cecconi, A. García-Alonso, D. M. R. Alvarez-López, P. García-Peñarrubia, "A study of CD33 (SIGLEC-3) antigen expression and function on activated human T and NK cells: two isoforms of CD33 are generated by alternative splicing," *J. Leukoc. Biol.*, vol. 79, pp. 46-58, 2006.

[185] F. Naeim, P. N. Rao, S. X. Song, W. W. Grody, Atlas of Hematopathology, Academic Press, Cambridge, MA, USA, 2013.

[186] S. P. Perfetto, P. K. Chattopadhyay, M. Roederer, "Seventeen-colour flow cytometry: unravelling the immune system," *Nat. Rev. Immunol.*, vol. 4, 648, 2004.

[187] I. J. Conlon, G. A. Dunn, A. W. Mudge, M. C. Raff, "Extracellular control of cell size," *Nat. Cell Biol.*, vol. 3, pp. 918-921, 2001.

[188] K. C. Cheung, M. Di Berardino, G. Schade-Kampmann, M. Hebeisen, A. Pierzchalski, J. Bocsi, A. Mittag, A. Tárnok, "Microfluidic impedance-based flow cytometry," *Cytometry A*, vol. 77A, pp. 648-666, 2010.

[189] N. Wang, R. Liu, N. Asmare, C. H. Chu, A. F. Sarioglu, "Processing code-multiplexed Coulter signals via deep convolutional neural networks," *Lab Chip*, vol. 19, pp. 3292-3304, 2019.

[190] Z. Chen, T. Dodig-Crnković, J. M. Schwenk, S. Tao, "Current applications of antibody microarrays," *Clin. Proteom.*, vol. 15, 7, 2018.

[191] B. B. Haab, “Methods and applications of antibody microarrays in cancer research,” *Proteomics*, vol. 3, pp. 2116-2122, 2003.

[192] L. Diéguez, M. A. Winter, K. J. Pocock, K. E. Bremmell, B. Thierry, “Efficient microfluidic negative enrichment of circulating tumor cells in blood using roughened PDMS,” *Analyst*, vol. 140, pp. 3565-3572, 2015.